GOVP1200506006

과제번호 M1-0203-00-0082

국가지정연구실사업

National Research Laboratory

시공간 고분해능 비선형 광학 측정 및 계측 기술 연구

Research on Temporal & Spatial High Resolution Nonlinear Optical Measurement Techniques

연 세 대 학 교

과 학 기 술 부

제 출 문

과학기술부 장관 귀하

본 보고서를 "시공간 고분해능 대면적 비선형 광학 측정 및 계측기술에 관한 연구"과제의 보고서로 제출합니다.

2004. 12.

주관연구기관명 : 연 세 대 학 교

주관연구책임자 : 박 승 한

연 구 원 : 임 상 엽

〃 : 최 문 구

〃 : 김 건 식

〃 : 이 현 호

〃 : 유 장 훈

〃 : 채 규 민

〃 : 오 승 일

〃 : 정 영 준

〃 : 양 재 석

〃 : 정 은 희

〃 : 김 대 근

〃 : 이 재 훈

〃 : 황 택 용

보 고 서 초 록

과제관리번호	M1-0203-00-0082	해당단계 연구기간	2002-06-25 ~ 2004-06-24	단계구분	1단계 / 총 2단계
연구사업명	중 사 업 명	국가지정연구실사업			
	세부사업명	국가지정연구실사업			
연구과제명	중 과 제 명				
	세부(단위)과제명	시공간 고분해능 대면적 비선형 광학 측정 및 계측기술			
연구책임자	박 승 한	해당단계 참여연구원수	총 : 12 명 내부 : 1 명 외부 : 11 명	해당단계 연구비	정부: 440,000 천원 기업: 천원 계: 440,000 천원
연구기관명 및 소속부서명	연세대학교 물리학과		참여기업명		-
국제공동연구	상대국명 : -		상대국연구기관명 :		
위 탁 연 구	연구기관명 :		연구책임자 :		

요약(연구결과를 중심으로 개조식 500자이내)

보고서 면수: 124면

1. 나노 탐침 Slide 제작
   - 나노 탐침 슬라이드를 표준적인 Si 공정을 이용하여 창의적으로 고안, 제작함
   - 100nm 정도의 나노 개구와, 시료를 올려놓을 수 있는 30nm 두께의 고강도 Si_3N_4 나노 슬라이드로 구성되어 있음
   - 기존 근접장 광학 현미경의 거리조절장치를 사용하지 않고도 근접장 광검출이 가능함

2. 단일 탐침 Slide/Tapered Optical Fiber Probe Interconnection
   - 광섬유 탐침과 나노 탐침 슬라이드를 근접장 영역에 접근시켜, 두 탐침을 200-300nm 영역내에서 interconnection에 성공함

3. 10ps/100nm 시공간 고분해능 비선형 광특성 측정 시스템 구성

4. 자체 집광 현상에 관한 FDTD 시뮬레이션 및 측정
   - FDTD 시뮬레이션 기법과 근접장 비선형 광측정을 통한 자체집광 현상을 연구함

5. 금속-반도체 Composite 나노 입자 제조
   - 금속-반도체 복합 나노구조를 제안하고 CNRS 연구소와 공동으로 제조에 성공함

6. 근접장 위상천이 간섭계 개발
   - 근접장 현미경의 탐침을 점광원으로 응용하여 위상천이 간섭계와 결합함으로써 공간 고분해능 위상정보를 근접장 영역에서 측정함
   - 광섬유 탐침에서 반사된 빛과 시료의 표면에서 반사된 빛이 간섭을 일으키게 함으로써 고분해능의 위상정보를 근접장 영역에서 측정함
   - 외부적인 형상에서는 볼 수 없는 복잡한 내부 구조를 광학적 위상 측정을 통해 측정함

색 인 어 (각 5개 이상)	한 글	비선형 광학 측정, 레이저, 레이저 분광, 레이저 계측, 비선형 나노분광
	영 어	nonlinear optics, laser, laser spectroscopy, laser metrology, nanophotonics

요 약 문

Ⅰ. 제 목

시공간 고분해능 대면적 비선형 광학 측정 및 계측기술에 관한 연구

Ⅱ. 연구개발의 목표

시공간 고분해능 비선형 광학 계측 기술 개발

- 초고속 및 초미세 영역에서 계측할 수 있는 고분해능 기술 개발
- 공간해상도 100nm, 시간분해능 10ps 비선형 광학 기술에 관한 특허 및 원천기술의 확보

Ⅲ. 연구개발의 내용 및 범위

10 ps/100 nm 시공간 고분해능 비선형 광특성 측정기술 개발

- 신기능성 단일 탐침 Slide 및 Array (5×5) Slide 설계/제작 (≤100nm)
- 100nm 탐침 Array Slide 특성 분석
  (SEM & NSOM)
- 단일 탐침 Slide / Tapered Optical Fiber Probe Interconnection
- 시간분해 고분해능 비선형 광특성 측정 시스템 구성 (10ps, 100nm)
- 나노 Composite 비선형 광특성 측정/분석

Ⅳ. 연구개발결과

1. 나노 탐침 Slide 제작

- 빛의 파장보다 훨씬 작은 크기(100nm)의 나노 개구와, 시료를 올려놓을

수 있는 30nm 두께의 고강도 Si_3N_4 나노 슬라이드로 구성된 나노 탐침 슬라이드를 표준적인 Si 공정을 이용하여 창의적으로 고안, 제작함.

- 기존 근접장 광학 현미경의 거리조절장치를 사용하지 않고도 근접장 광검출이 가능함

2. 10ps/100nm 시공간 고분해능 비선형 광특성 측정 시스템
   - 10ps 시간 분해능 단일 광자 계수 장치를 100nm 공간 분해능 근접장 광학 현미경에 결합함.

3. 단일 탐침 Slide/Tapered Optical Fiber Probe Interconnection
   - 광섬유 탐침과 나노 탐침 슬라이드를 근접장 영역에 접근시켜, 두 탐침을 2차원 평면상의 200-300nm 영역 안에서 interconnection함.

4. 자체 집광 현상에 관한 FDTD 시뮬레이션 및 측정
   - FDTD 시뮬레이션 기법과 근접장 비선형 광측정을 통하여 자체집광 현상을 연구하고, 광세기에 따른 AsS 박막의 근접장 광분포를 측정함

5. 금속-반도체 Composite 나노 입자 제조
   - 금속-반도체 복합 나노구조를 제안하고, 프랑스 ICMCB CNRS연구소와 공동 연구를 통해 성공적으로 제조함.

6. 근접장 위상천이 간섭계 개발
   - 근접장 현미경의 광섬유 탐침에서 반사된 빛과 시료의 표면에서 반사된 빛이 간섭을 일으키게 함으로써 고분해능의 위상정보를 근접장 영역에서 측정하여 외부에서는 볼 수 없는 내부구조를 측정할 수 있었음.

V. 향후 연구개발 계획

1. 1단계 연구 개발을 통해 얻은 시공간 고분해능 비선형 광특성 측정 기술의 체계화 및 최적화

2. 공간 해상도 30nm, 시간 분해능 100fs, 대면적 1mm×1mm의 비선형 광특성 측정 기술 확립

3. 고분해능 광위상 정보 측정 기술과 근접장 파면 측정 기술을 비선형 광측정 분야로 확장

S U M M A R Y

Ⅰ. Title

Research on the Optical Measurement and Instrumentation of Temporal and Spatial High Resolution Nonlinear Near-field Scanning Optical Microscopy of Large Areas

Ⅱ. Objectives

Development of Temporal and Spatial High Resolution Nonlinear Near-field Scanning Optical Microscope

- Development of nonlinear measurement techniques in 10ps/100nm regime.
- Obtaining proprietary technology associated in nonlinear optics with spacial resolution of 100nm, and temporal resolution of 10ps

Ⅲ. Contents and Scope

10ps/100nm temporal and spatial high resolution nonlinear optical characteristic measurement technology development

- Novel design and development of single probe slide and Array (5×5) Slide (≤100nm)
- Analysis of 100nm probe array slide characteristics (SEM & NSOM)
- Single probe slide / tapered optical fiber probe interconnection
- Construction of temporal and spatial high resolution nonlinear optical characteristic measurement system (10ps, 100nm)
- Measurement and analysis of nonlinear optical characteristics of nano-composite structures

Ⅳ. Results

1. Fabrication of Nano Probe Slide

- Novel development and fabrication of a Nano-probe Slide consisting of a aperture of dimensions much smaller than the wavelength (100nm) and a sample slide of thickness 30nm Si_3N_4 using standard Si manufacturing procedures
- Optical detection made possible without using previously developed distance regulation methods for near-field scanning optical microscopy

2. 10ps/100nm Temporal and Spatial High Resolution Nonlinear Optical Characteristic Measurement System

- Combination of 10ps temporal resolution single photon counting equipment onto 100nm spatial resolution near-field optical microscope

3. Single Probe Slide/Tapered Optical Fiber Probe Interconnection

- Interconnection in a 200~300nm 2 dimensional region of a tapered optical fiber probe and a nano probe slide in the near-field

4. FDTD Simulations and Experimental Measurements of Self-focusing Effects

- Development of FDTD simulation techniques to study self-focusing effects and multiple filamentation in AsS thinfilms depending on sample thickness and beam intensity

5. Metal-Semiconductor Composite Nano-particle Fabrication

- Successful fabrication of metal-semiconductor composite nano-structures through collaboration with CNRS laboratory in France

6. Development of Near-field Scanning Optical Interferometer

- Measurement of high resolution optical phase information using the interference of light reflected from the fiber facet of a near-field optical microscope and that reflected from the sample surface. Images containing complex internal information can be obtained through this method which cannot be seen in the topographic image.

V. Future Research Plans

1. Systemization and optimization of the temporal and spatial high resolution nonlinear optical measurement system developed in the 1st stage of research development

2. Development of nonlinear optical measurement techniques of 30nm spatial resolution , 100fs temporal resolution, and 1mm×1mm large area

3. Expansion of high resolution optical phase information measurement techniques and near-field wavefront measurement techniques into fields of nonlinear optical measurement

C O N T E N T S

목 차

제 1 장 연구개발과제의 개요

제 1 절 연구 개발의 필요성

21세기에 전개되고 있는 과학기술의 급격한 진보와 정보 혁명의 흐름 속에서 우리나라가 진정한 선진국으로 진입하기 위해서는 시대적 흐름에 부응하는 기반지식과 원천기술을 반드시 확보하여야 한다. 특히, 미래사회가 요구하고 있는 초경량화, 초고감도화, 초소형화 및 초저전력화 기술 분야에서 과학 기술적인 우위를 선점할 수 있어야 하며, 이를 달성하기 위해서는 고부가가치의 초정밀 측정 및 계측 기술 분야에서 독창적인 연구·기술 능력을 시급히 확보하여야 한다. "비선형 광학 측정 및 계측 기술"은 이러한 초정밀 측정 및 계측 기술의 하나로서, 물리학, 화학, 생물학 등의 기초 연구 분야는 물론 초고속 정보통신, 고밀도 나노소재 개발, 동위원소 분리, 환경오염 원격 감시, 임상의학 진단 및 치료 등과 같이 21세기 국가 경쟁력의 핵심 산업 분야로 알려져 있는 정보/통신(IT), 나노(NT), 환경(ET), 생명(BT), 우주(ST) 산업 분야에 직접적으로 응용할 수 있는 초정밀 측정 및 계측 관련 "핵심 원천요소 기반기술"이다.

이와 같은 비선형 광학 측정 및 계측 기술은, 두 개 이상의 파장의 레이저를 조사시켜서 새로운 파장의 빛을 발생시키는 비선형 혼합파 발생기술, 강한 세기의 레이저 빛에 따른 흡수 변화를 측정하는 들뜸 비선형기술, 시간에 따른 비선형성의 변화를 측정하는 시간분해 비선형 기술, 그리고 자체 집광/퍼짐 기술, 다광자 발생기술, 유도 라만 산란 기술 등으로 구성되어 있다[Mukamel(1995), Newell(1992), Boyd(1992), Shen(1991), Zernike(1973), Bloembergen(1965)]. 현재 비선형 광학 측정 및 계측 기술은 대기오염 감시 및 자동차 내연기관 연소효율 측정기술 등에 적용되어 그 진가를 인정받고 있으며, 정보통신 분야에 있어서도 솔리톤 전송 및 초고속 광스위치 등으로 응용되고 있다. 또한 생체 조직의 광학적 비선형 특성을 이용하여 3차원 laser tomography, 비침습 진단기기 등과 같은 장비들로도 적극 개발되고 있는 등 다양한 산업 분야에서 다양한 종류의 정밀 측정 및 계측에 활용되고 있다.

하지만 21세기에 들어와 과학기술이 마이크로 기술에서 나노기술의 새 분야로 영역이 확대되면서 레이저를 이용한 이러한 비선형광학 측정 및 계측 기술은 나노기술의 영역에서 관찰하고 측정할 수 있는 "고분해능 비선형 광학 측정 기술"로 변모해야 할 필요성이 대두되게 되었다. 따라서 회절한계를 넘어서는 초미세 시스템에서 일어나는 현상을 관측, 분석 혹은 제어하기 위한 "고분해능 비선형 측정 및 계측 기술"은 21세기 새로운 기술 패러다임에 적합한 핵심 원천기술로서 그 중요성을 크게 인정받고 있다.

표 1-1. 비선형 분광기술 및 활용분야

분 류	기 술 의 개 요	세 부 구 성 기 술	활 용 분 야
다광파 혼합기술	물질에 입사된 여러 광파들의 상호 작용에 의하여 발생되는 광파의 세기 및 스펙트럼을 분석하는 기술	·이광파 혼합 기술 ·4광파 혼합기술	·연소성분 분석 및 진단 ·대기오염 감시기술 ·광섬유 증폭/센서/통신 ·고분해 식각기술
다광자 분광기술	물질에 강한 여기광이 입사되어 광자 2개이상을 동시에 흡수하여 발생되는 흡수 변화 및 형광을 분석 하는 기술	·이광자 흡수 분광기술 ·다광자 유도 형광 기술	·동위원소 분리기술 ·고해상도 이광자 영상기술 ·Optical Limiter
조화파 발생기술	입사된 여기광들의 진동수의 정수배 또는 차이에 해당하는 새로운 진동수의 광파 발생 기술	·Sum frequency 발생기술 ·고차 조화파 발생기술 ·광파라메트릭 발생기술	·중적외선 광원 ·통신용 주파수 변환기 ·파장 가변 레이저 ·DVD
포화 분광기술	좁은 파장폭을 갖는 강한 빛을 물질에 조사 시켜 특정한 에너지 상태를 포화시켜서 나타나는 물리적 현상을 관찰 하는 기술	·자체 포화 분광기술 ·띄움-들띄움 분광 기술 ·Multilevel Saturation spectroscopy	·반도체 레이저 개발 ·광메모리 ·광전 변조기/결합기 ·고분자 소자 개발 ·극미량 분석기술
시간분해 분광기술	광검출기의 한정된 반응 시간을 초단 펄스와 광지연기법을 이용하여 극복하고 시간에 따른 역동적으로 변화하는 비선형 광현상을 관찰 하는 기술	·시간분해 차등 투과 분광기술 ·시간상관 단일광자 계수 분광기술 ·광투과 변조 기술	·광 스위칭 ·생체 진단기술 ·혈중성분 분석진단 ·형광체 개발 ·차세대 양자신소재 개발

1. 기술적 필요성

일반적으로 백열등과 같이 약한 빛을 물질에 조사하면 빛은 반사, 투과, 혹은 흡수되는데, 이 때 입사한 빛이 물질에 의하여 반사, 투과, 흡수되는 비율은 입사된 빛의 광량에 관계없이 일정하다. 그러나 강한 레이저광이 물질에 조사되면 그 물질계를 구성하고 있는 원자(혹은 분자)와 레이저광 사이에 강한 상호작용이 일어나 반사율, 투과율, 흡수율 및 굴절률 등이 레이저광의 세기와 조사시간에 따라 변화하거나, 조사된 레이저의 파장과는 전혀 다른 파장의 빛이 발생되는 등의 특이한 특징을 갖는 비선형 현상이 일어나게 되는데, 이러한 비선형 특성을 과학적인 측면에서 체계적으로 연구·분석하고 그 원인을 규명하며, 이를 공학적인 측면에서 응용하여 초정밀 광학 측정 및 계측 시스템을 구축할 수 있도록 하는 것이 "비선형 광학 측정 및 계측 기술"이다.

현재 초고속 광스위치에 적용되고 있는 기술은 전기장의 세기에 따른 물질의 흡수변화와 그에 따른 굴절율 변화인 비선형 광학 특성을 이용한 것이며, 대기오염 물질 분석에 이용되는 안티-스톡 라만 분광(CARS) 기술은 공기 중에 두 가지의 다른 주파수를 가진 강한 빛을 동시에 조사시켰을 때 입사된 두 빛의 주파수 차이에 분자의 고유 진동수 차이가 더해지거나 차감 된 주파수의 빛을 발생시키는 것이다. 또한 초고속 정보전송기술로 떠오르고 있는 soliton 전송법 역시 비선형 현상으로 빛의 세기에 따른 물질의 굴절율 변화를 이용한 것이다. 또 방사성 동위 원소 분리에 응용되는 다광자 이온화(multi-photon ionization) 기술은 물질의 다차 비선형 현상을 이용하는 기술이다.

이와 같은 비선형 광학 측정 및 계측 기술은 현재 EDFA, 반도체 레이저, 광변조기, 오염도 측정기술 관련 산업 등에 적극적으로 활용되고 있을 뿐만 아니라, 향후 정보/통신, 의료, 환경, 자원 산업 등 차세대 핵심 산업구조 전반에 커다란 영향을 미칠 기반기술로서 확고히 자리잡고 있다. 또한 환경오염 물질이나 생체 시료의 극미량 성분분석 기술에도 탁월한 성능을 보이고 있어 최근 들어 이와 관련한 고부가 가치의 상품이 계속 창출되고 있고, 이를 지원하는 시스템 장비 생산 업체도 급격히 늘고 있다.

따라서 향후 비선형 광학 측정 및 계측 기술의 수요는 차세대 NT, IT, BT, ET, ST 산업 분야 전반에 걸쳐 시공간 고분해능 비선형 광학 측정 및 계측 기술을 중심으로 앞으로도 크게 증가할 것으로 예상되며 이에 따른 새로운 산업기반도 형성될 것으로 예상

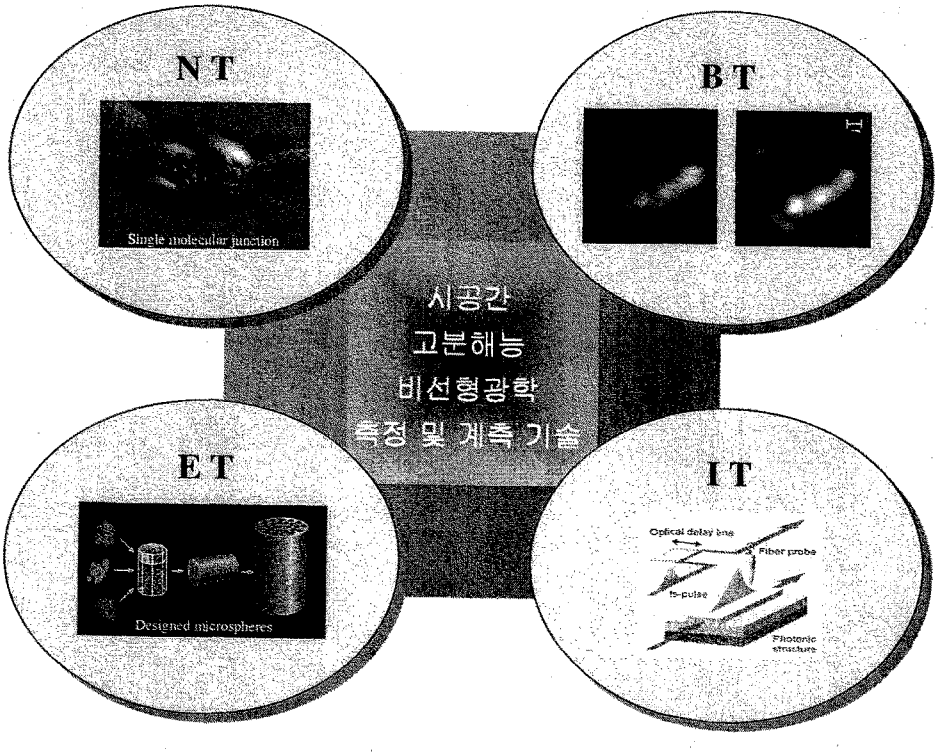

그림 1. 시공간 고분해능 비선형 광학 측정 및 계측 기술 활용 분야

되므로, 고분해능 비선형 광학 측정 및 계측 기술은 핵심 기반기술로서 우리 나라의 국가 경쟁력 확보라는 차원에서 매우 중요한 기술이다. 특히, 이 분야의 국가 경쟁력 확보는 특허 및 원천 기술을 어떻게 확보하는 가의 측면이 매우 중요하므로, 특허 및 원천기술을 선점하기 위한 비선형 광학 측정 및 계측 기기의 시공간 초고분해능화 기술, 초고감도화 기술, 초소형화 및 초경량화 기술 등의 개발이 시급히 필요하다.

특히 기존의 비선형 광학 측정 및 계측 기술은 회절한계 때문에 공간 분해능의 한계가 있었고 SEM, TEM, STM, AFM 등은 분해능은 좋으나 생물 분자와 같은 시스템을 관측하는 데는 한계가 있었으므로, 고분해능 비선형 광학 측정 및 계측 기술은 그림 1에서 볼 수 있듯이 우리나라 미래의 국부를 창출할 수 있는 차세대 신규 산업에로의 응용 가능성이 지대하여 최근 주목을 받고 있는 정보기술, 나노기술 및 신소재 기술 산업분야와 생명과학을 포함한 바이오기술 산업분야 등에서 핵심 기술로서의 영향력을 넓혀 가리라 예상된다.

2. 경제·산업적 필요성

21세기는 정보와 생명 산업의 시대이며 나노-바이오 테크놀로지 분야의 발전이 산업발전의 원동력이 될 것으로 예상된다. 특히 정보 산업의 근간인 나노기술과 생명산업의 근간인 바이오기술, 그리고 이를 결합한 나노바이오 기술 분야의 약진이 예측되고 있다. 이러한 나노바이오 분야에서의 획기적인 발전을 가져오기 위해서는 스위칭 기능을 갖는 단분자 시스템의 개발과 이들 분자 시스템의 2차원 혹은 3차원 공간적 배열을 할 수 있어야 하며, 다양한 크기의 단백질, 효소, 항체, DNA 등의 생체 나노분자를 제어할 수 있거나 생체 현상을 모방한 새로운 개념의 나노 신소재 및 단분자 첨단 소재·소자의 특성을 측정하고 제어할 수 있어야 한다.

따라서 본 연구를 통하여 추구하고 있는 시공간 고분해능 비선형 광학 측정 및 계측 기술은 21세기 국가 기술 경쟁력 확보를 위한 효자산업 창출을 위하여 반드시 선행되어야 할 필연적인 연구이며 차세대 나노바이오 산업의 핵심 기반 기술이 될 수 있으리라 기대된다. 또한, 개발될 고부가가치의 첨단 고분해능 비선형 측정 및 계측 기술은 차세대 고밀도 광기록 매체인 HD-DVD에 사용되는 핵심 광학부품의 초정밀 성능 평가 혹

은 반도체 레이저 및 반도체 소자의 평가에도 응용될 수 있기 때문에 반도체 관련 분야의 기술 자립에도 크게 기여할 수 있으리라 기대된다.

3. 사회·문화적 필요성

지난 수 십 년간 전자를 이용한 실리콘 전자 소자의 고속화, 고집적화, 대용량화를 시키려는 부단한 노력을 기울여 온 결과 현재와 같은 눈부신 정보혁명의 시대를 이룩하게 되었다. 그러나 이러한 실리콘 전자소자들은 운반자 이동속도의 감소, 전자기적인 간섭 및 병렬처리의 어려움 등 여러 가지 근본적인 한계에 직면하고 있다. 기존의 실리콘 소자가 갖고 있는 이러한 문제점을 극복 혹은 보완하기 위하여 많은 연구가 진행되어 왔는데 광전소자도 해결 방안의 하나로 연구 개발되어 왔다. 고분해능 비선형 측정 및 계측 기술은 이와 같은 광전소자 개발 및 광전소자의 고밀도 집적화 기술 개발에 핵심적인 역할을 함으로써 정보기술에 기초한 삶의 편의성 향상에 기여할 수 있을 것이며, 초고속 질병 진단 및 치료, 신약의 초고속 약효 검색, 고감도 환경분석 등을 통하여 건강한 삶의 실현에 기여하는 등 사회·문화 전반에 걸쳐 큰 영향을 미칠 것으로 예상된다. 따라서 사회 문화적 측면에서 고분해능 비선형 측정 및 계측기술은 NT, IT, BT 등의 기술 진보에 핵심적인 기여를 할 수 있으므로 작게는 현 생활에 이롭게 이용되는 과학문화의 혜택을 풍요롭게 할 것이고, 크게는 아직 알려지지 않은 새로운 원리를 발견하고 이해하며 이를 구체화하는데 기여할 수 있을 것이다.

제 2 절 연구개발의 내용 및 범위

현재 널리 사용되고 있는 고분해능 전자현미경인 TEM 및 SEM, 그리고 STM, AFM 등은 미세구조물의 구조 형태에 관한 정보를 제공하고 있으나, 아직도 생물 분자와 같은 복잡하고 다양한 시스템을 관측/분석/제어하는 데는 한계가 있다. 또한, 빛의 파장을 줄여서 회절한계 내에서 분해능을 높이는 방법은 여러 가지 기술적인 문제점들 때문에 한계에 부딪히고 있어, 비접촉, 비파괴 검사가 가능하고 신뢰성 높은 "고분해능 비선

형 측정 및 계측기술"은 앞으로 미래의 산업 분야에 큰 파급효과를 미칠 것으로 예상된다. 이와 같은 "고분해능 비선형 광학 측정 및 계측 기술"을 구현하기 위해서는 다양한 요소 기술을 필요로 하나, 본 연구실에서는 아래와 같은 세 가지 핵심 기술 개발을 중점적으로 연구하고 있다.

1. 공간 고분해능 단일 탐침 Slide의 설계 및 제작

현재 고분해능 광학 측정 장치에 사용되고 있는 Tapered Optical Fiber Probe(TOFP)는 Throughput이 작고, 수명이 짧고, 내구성이 낮으며, 다루기가 용이하지 않고, 두 개 혹은 그 이상의 Fiber Probe를 가까이 배치하기 어려운 단점이 있다. 본 연구실에서는 이와 같은 문제점을 해결하기 위하여 Si 의 Anisotropic 특성을 이용한 탐침 개발에 초점을 맞추어 연구를 수행하여 왔다, 특히, 탐침 아랫 면에 경도가 강하고 레이저광 투과성이 우수한 Si_3N_4 박막을 nm의 두께로 증착한 고분해능 탐침 Slide를 제작함으로써 초미세 생체 분자 등의 비선형 측정과 계측을 용이하게 할 수 있는 독창적인 기술을 창출하여 새로운 개념의 고분해능 탐침 개발하고자 한다(Si_3N_4 박막 탐침 Slide: 특허출원번호(10-2002-19474)).

2. 탐침 Array Slide 응용 고분해능 대면적 비선형 광특성 측정 및 계측기술 개발

NSOM을 비롯한 고분해능 광학 측정 장치는 정밀도는 높으나 100μm×100μm 정도의 면적에 제한되는 영역만을 관측하는 한계가 있으며 스캐닝 속도가 낮은 단점이 있었다. 본 연구실에서는 이 문제점을 극복하기 위하여 고분해능 탐침을 Array로 제작하고 스캐닝을 하는 동안 각 탐침을 동시에 관측할 수 있는 시스템을 구축함으로써 1mm×1mm 정도의 대면적을 고분해능으로 짧은 시간에 관측할 수 있는 비선형 광학 측정 및 계측을 구현하고자 한다.

3. 100fs/30nm 시공간 고분해능 비선형 광학 측정 및 계측 기술 개발

기존의 Time-Correlated Single Photon Counting System 혹은 Femto

Second Pump-Probe 분광기법 등을 공간 고분해능 비선형 광학 측정 및 계측 기술에 접목할 수 있다면, 회절한계를 넘어서는 초미세 시스템에서 일어나는 초고속 현상을 관측, 분석 혹은 제어할 수 있다. 따라서 본 연구실에서는 그 동안 수행하여 온 다양한 비선형 분광기법 및 비선형 광기술 응용 연구의 기반과 이미 확보하고 있는 다양한 종류의 레이저를 비롯한 주변 연구장비들을 최대한 활용하여, 100fs/30nm의 시공간 분해능으로 초미세 구조 혹은 나노바이오 시스템에서 일어나는 초고속 현상를 관측하거나 비선형 스펙트럼 측정/분석 혹은 비선형 이미징을 획득할 수 있는 원천 기술의 확보를 시도하고자 한다(그림 2 참조).

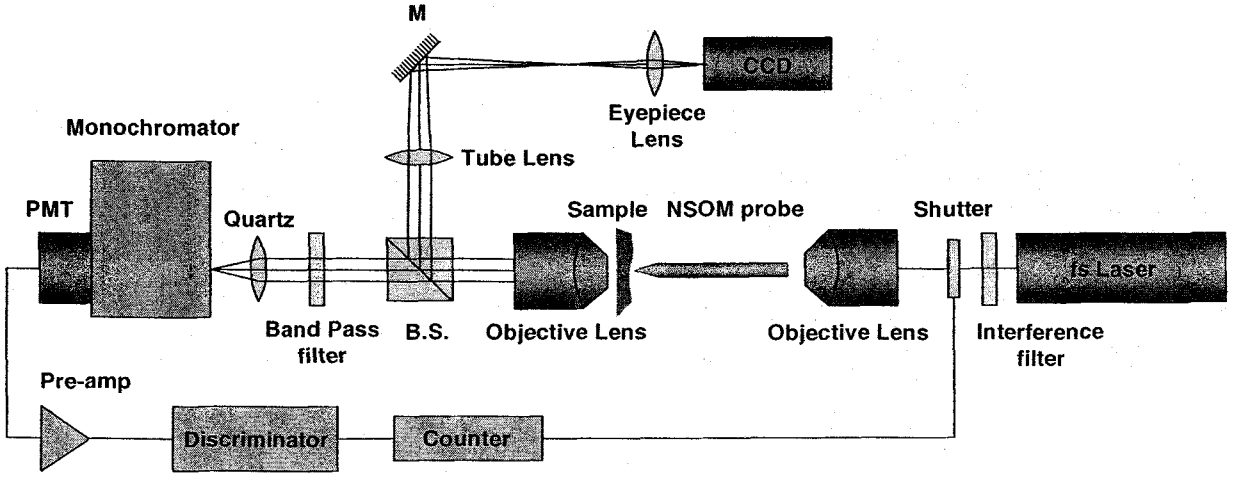

그림 2. 시공간 고분해능 비선형 측정 및 계측 장치도

제 2 장 국내외 기술개발 현황

제 1 절 국외 기술개발 현황

미국, 일본, 유럽 등 선진국에서는 준평형상태 비선형 분광 기술 및 초고속 비선형 광특성 측정 기술이 확립되어 있으며, 이는 극초단 펄스 레이저 기술의 비약적인 발전에 힘입은 바가 크다. 예를 들면 미국에는 Stanford 대학의 SPRC, UCSB의 Quantum Institute, Lucent Technology, 유럽에는 독일 Max Planck Institute의 Quantum Optics 그룹, 일본의 RIKEN 내의 Frontier Research Program 등에서 시간분해 비선형 광학 측정 및 계측이 이루어 지고 있다. 최근 들어 이들 연구기관은 물론 시공간 고분해능 비선형 광학 측정 및 계측 연구를 수행하고 있는 연구소 혹은 대학이 급속히 증가하고 있다. 특히, 활발히 연구가 진행되고 있는 미국의 연구기관으로는 Strategic Research Orientation NanoLink Program을 운영하고 있는 버클리 대학, Center for Ultrafast Optical Science가 소재하고 있는 미시간 대학을 들 수 있으며, 일본도 Near-field Nano-optics Project 및 ERATO Localized Photon Project를 진행하고 있다. 최근에 문헌상에 발표된 자료를 중심으로 시공간 두 영역에서 동시에 고분해능의 비선형 광학 특성 측정기술을 보유한 그룹을 살펴보면 표 1-2와 같다.

표 1-2. 시공간 고분해능 비선형 광학 연구그룹

국가	연구그룹	비선형 가법	시간분해능	공간해상도	출처
미국	Harvard U. (Xie 그룹)	Two Photon Absorption	-	20nm (metal tip)	PRL82,4014(1999)
	SUNY (Shen 그룹)	Two Photon Fluorescence Imaging	-	200nm	APL76,1(2000)
독일	Max-Born-Institute (Lienau 그룹)	fs Pump-Probe	200fs	100nm	PRB61,R10583(2000)
스위스	FIT (Keller 그룹)	fs Pump-Probe	250fs	150nm	RSI70,2758(1999), PRB65,45322(2002)
일본	Tokyo U. (Tani 그룹)	Two Color fs Pump-Probe	250fs	200nm	APL 77, 1283 (2000)

제 2 절 국내 기술개발 현황

국내 비선형 광특성 측정기술은 서울대, 서강대, 이화여대, 부산대, 인하대, KAIST 등에서 활발히 진행되고 있으며, 국가 출연 연구기관인 한국원자력연구원과 한국표준과학연구원, ETRI, 및 KIST등에서도 기기 개발 및 응용연구가 활발히 진행되고 있다. 대학과 연구소의 연구그룹은 현재 국내외 학술지에 꾸준히 연구결과를 발표하고 있으며, 각 그룹은 필요에 따라 비선형 광학 측정 및 계측 기술 중의 일부를 구축하여 연구를 수행하고 있다. 하지만 아직은 시공간 고분해 비선형 광학 측정 및 계측을 시도하고 있는 곳은 매우 적은 상태이며, 이를 이용하는 응용 분야의 연구는 거의 없는 실정이다. 또한 국내의 비선형 광학 측정 및 계측 관련 산업은 아직 선진국에 비하여 기술적인 면에서 수준이 낮은 편이므로, 향후 경쟁력 확보를 위한 특허 및 원천기술을 획득하기 위해서는 비선형 광학 측정 및 계측 기기의 초고분해능화 기술, 초고감도화 기술, 소형화 및 경량화 기술 등을 중점적으로 개발하는 방향의 연구를 반드시 수행하여야 할 것이다.

제 3 장 연구개발 수행 내용 및 결과

제 1 절 신기능성 Si_3N_4 탑재 탐침 Slide의 설계 및 제작

1. 신기능성 Si_3N_4 탑재 탐침 Slide의 설계 및 제작 배경

기존의 고분해능 비선형 기술의 핵심은 렌즈를 이용하여 관측하고자 하는 시료의 국소 영역에 레이저광을 입사시키고 국소 영역에서의 변화를 관측하는 것이었다. 이와 같은 현미경 기술은 대물렌즈를 시료 표면에서 파장보다 매우 먼 거리에 두고 관측하므로 회절현상으로 인한 분해능 한계를 피할 수가 없다. 본 연구실에서는 이러한 회절한계를 넘어서는 고분해능 비선형 광특성 측정기술을 확보하기 위하여 근래에 급속도로 발전하고 있는 근접장 기술에 관한 연구를 수행하여 왔다. 근접장 기술은 파장보다 매우 작은 개구를 지닌 탐침을 시료 표면에서부터 파장보다 매우 작은 근접거리에 위치시켜 시료 표면을 주사하면서 회절되기 이전의 빛을 검출함으로써 회절한계를 극복하는 기법이다[Pohl(1984), Betzig(1991)].

이러한 근접장 기술을 적용할 때 가장 중요한 구성요소 가운데 하나가 탐침이다. 근접장 광학 현미경에서 사용되는 탐침은 매우 다양해서 광섬유 탐침, AFM 캔티레버, 'aperture less' 금속 탐침, SIL (Solid Immersion Lens) 등이 있지만 주로 사용되는 탐침은 광섬유를 잡아당기거나 식각하여 뾰족하게 만든 후 개구 부분만을 제외하고 금속 코팅을 함으로써 제작하는 tapered optical fiber probe이다. 일반적으로 끝단에 형성되는 개구는 수십 내지 수백 nm 직경을 지닌다. 본 연구실에서도 실제로 이러한 광섬유 탐침을 이용하여 반도체 양자우물 구조 및 양자점 구조에 대한 연구를 수행한 바 있다.

그러나 광섬유 탐침은 throughput이 작고, 수명이 짧으며, 내구성이 떨어지는 단점이 있다. 특히 기존 근접장 광학 현미경에서 광섬유 탐침을 비롯한 여러 탐침으로 근접장 광영상을 얻을 때, 시료에 수-수십 nm까지 탐침을 근접시킨 후 시료-탐침 간 거리를 일정하게 유지하는 거리유지 장치를 사용하고 있는데 이는 근접장 광학 현미경 기술을 적용하는 광 소자 개발 연구에 가장 커다란 걸림돌로 작용하고 있다.

이러한 단점을 보완하고 새로운 개념의 고분해능 비선형 광학 측정 및 계측 연구

를 수행하기 위하여 신기능성 탐침 Slide를 제안하고, 탐침 Slide의 최적 제작을 위한 공정과정을 연구하였다. 신기능성 탐침 Slide는 파장보다 작은 개구와 그 개구를 덮고 있는 광학적으로 투명한 나노미터 두께의 Si_3N_4 박막으로 이루어져 있다. 개구는 앞에서 언급한 바와 같이 근접장 탐침의 요건인 광 국소화를 위한 부분이고, 개구를 덮고 있는 Si_3N_4 박막은 나노 구조 물질이나 생체시료 등을 직접적으로 올려놓을 수 있도록 되어 있다. 본 연구실에서 제안한 이러한 나노 Slide의 장점은 시료를 단순히 나노 Slide 위에 올려놓기만 해도 자동적으로 개구와 시료 사이의 거리가 파장보다 매우 짧은 근접거리가 되므로 별도의 근접장 거리 유지 장치 없이 근접장 탐침의 역할을 가능하게 하며 향후 이를 이용한 광소자 개발에 유용하게 적용될 수 있으리라 기대된다.

2. 신기능성 Si_3N_4 탑재 탐침 Slide의 제작 방법

신기능성 Si_3N_4 탑재 탐침 Slide를 제작하기 위해서 기존 광 리소그래피와 Si 계열 공정기술을 적용하였다. Si 을 비등방 식각하면 Si 이 지니고 있는 비등방 식각 특성에 따라 Si {111}면이 식각 저지면으로 작용하기 때문에 Si {100} 면으로 식각 깊이가 깊어짐에 따라 너비가 줄어들어 역 피라미드 모양의 홈이 생긴다[Seidel(1990)]. 적당한 마스크 크기를 선택하면 끝단에서의 개구 크기를 파장 이하로 조절할 수 있다[Lee(1999)]. 한편 수십 나노미터 두께의 Si_3N_4 막으로 개구를 덮으면 그 막은 나노 구조 물질을 올려놓을 수 있는 나노 Slide 역할을 하게 된다.

제안된 나노 탐침 Slide의 제작 공정 중 광 리소그래피 및 식각 에러를 줄이기 위해서 SOI (Silicon On Insulator) 기판의 15μm 두께 Si (100) 층을 사용하였다. Si 층의 양면에는 LPCVD로 Si_3N_4 막을 증착하였는데 아래면의 Si_3N_4 막은 리소그래피용 마스크로서, 윗면의 30nm 두께 Si_3N_4 막은 마지막까지 남아서 나노 Slide 역할을 하게 하였다. 나노 Slide로서 Si_3N_4 막을 사용한 이유는 가시광에서 자외선 영역까지 광학적으로 투명해서 광학 실험에 지장이 없을 뿐만 아니라 매우 강도가 높아서 내구성이 좋기 때문이다. 더군다나 Si_3N_4 막은 Si 공정 과정 중에 증착할 수 있기 때문에 공정 진행이 중단되지 않는 이점도 있다.

탐침 개구를 위한 패턴을 광 리소그래피로 만든 후 마스크 막으로 작용하는

Si_3N_4 막에 Reactive Ion Etching(RIE)으로 식각과정을 거쳤다. 그 후 Si을 10 wt. %, 65 ℃ KOH 수용액에 담가 비등방 식각을 수행하였다. α-step 스타일러스로 측정한 식각 속도는 시간당 40㎛ 정도이었다. 본 연구진이 개발한 나노 탐침 Slide의 제작 공정은 그림 3와 같다.

3. 제작된 신기능성 Si_3N_4 탑재 탐침 Slide의 특성 조사

개발한 공정과정을 통하여 제작된 나노 탐침 Slide는 광학현미경과 주사 전자현미경, 그리고 근접장 광학 현미경을 이용하여 특성을 연구하였다. 연구 결과 광 리소그래피를 이용한 표준화 된 Si 공정 작업을 통해 나노 구조 물질을 올려놓을 수 있는 나노 탐침 Slide 및 나노 탐침 Array Slide의 제작이 가능함을 확인할 수 있었다. 그림 4(a)와 (b)는 제작된 50nm x 50nm 단일 나노 탐침 Slide와 5 x 5 Array 나노 탐침 Slide의 주사 전자현미경 영상이다. 전자현미경 영상을 통해 배열 내의 개구 크기를 측정한 결과 같은 패턴으로부터 형성된 개구가 거의 같은 크기를 가짐을 확인하였다. 특히 개구 크기는 한 방향에 대해서 단조 증가하거나 단조 감소하는 경향을 보였다. 이는 개구 크기 에러의 주 원인이 Si 층의 두께 변화임을 암시한다. 즉 탐침 배열이 형성되는 수백 ㎛ 이내에서는 Si 층의 두께가 서서히 변화하기 때문에 그 두께 변화가 개구 크기로 이어진 것으로 추정된다. 순조로운 공정 과정을 거쳐 제작된 탐침의 경우 10개의 개구 크기가 100 nm 이내로 제어됨을 알 수 있었다. 이와 같은 공정을 통하여 파장 이하의 개구 크기를 갖는 단일 탐침 및 Array 구조를 성공적으로 형성하였다.

제 2 절 10ps/100nm 시공간 고분해능 비선형 광특성 측정 시스템

그 동안 수행하여 온 다양한 비선형 분광기법 및 비선형 광기술 응용 연구의 기반을 바탕으로 초미세 구조 혹은 나노 바이오 시스템에서 일어나는 초고속 현상을 관측하거나 비선형 스펙트럼 측정/분석 혹은 비선형 이미징을 획득할 수 있는 10ps/100nm 급 시공간 고분해능 비선형 광특성 측정 시스템을 개발하였다.

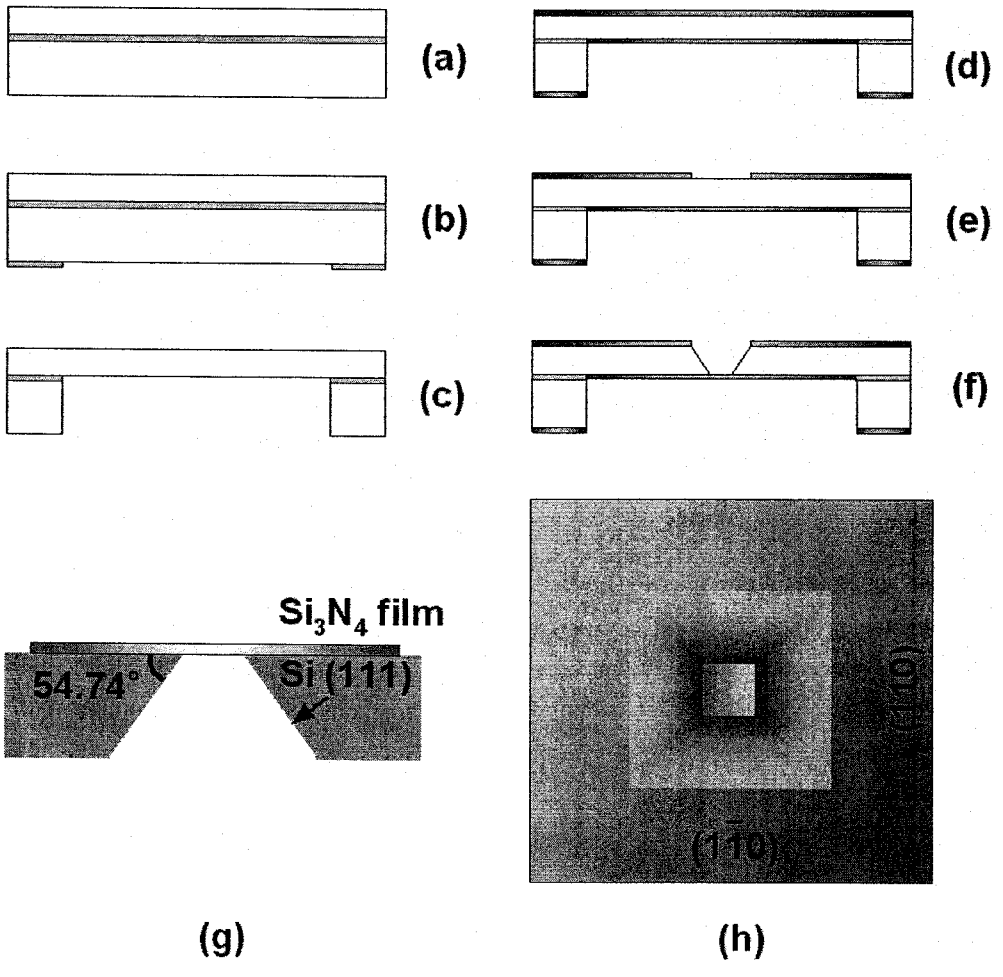

그림 3. 나노 탐침 Slide 제작 공정

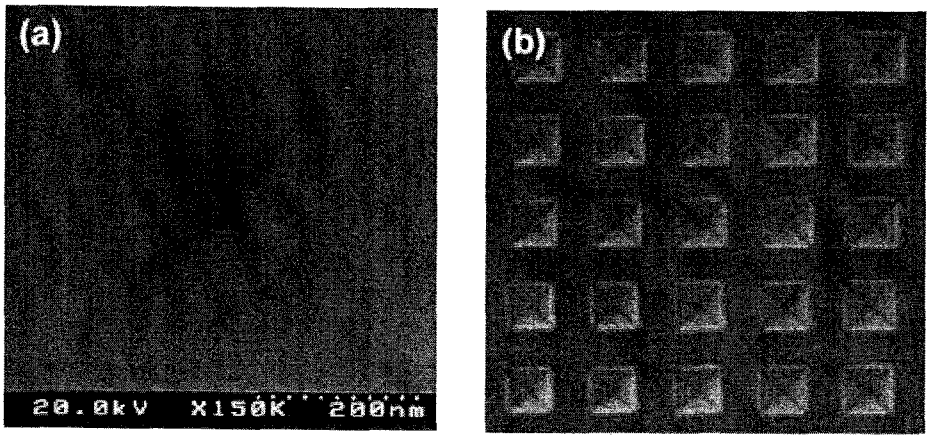

그림 4. 단일 나노 탐침 및 5x5 Array 나노 탐침

1. 공간 고분해능 비선형 광 측정 장치의 개선

근접장 광학 현미경의 핵심 기술의 한가지는 탐침을 시료로부터 수십 nm 이내로 근접시켜 제어하는 기술이다. 일반적으로 tuning fork를 거리조절 센서로서 사용하는 방법이 가장 보편화되어 있는데, 이는 다른 부대 장치가 필요 없고 사용이 간편하기 때문이다[Karrai(1995)]. 주로 공명 주파수가 32,768 Hz인 tuning fork의 한쪽 면에 광섬유 탐침을 접착한 뒤 전압을 인가하여 자체 여기시키거나 혹은 PZT 위에 다시 접착한 후 외부에서 PZT를 진동시켜 여기시킨다. tuning fork로부터 발생하는 전기 신호는 진폭에 비례하기 때문에 그 신호를 모니터링하고 있으면 광섬유 탐침이 근접장 영역에 들어갈 때 shear force로 인해 진폭이 감소하므로 시료-탐침 간 거리 유지가 가능해진다. 그런데 일반적인 tuning fork 이용 거리조절 센서는 근접장 탐침이 시료와 완전히 닿은 상태일 때 신호 크기가 0이 아니다.

본 연구실에서는 tuning fork 센서의 주파수 반응 곡선이 근접장 영역으로 들어가는 경우 고주파수 영역으로 수 Hz 정도 천이한다는 사실에 주목하였다[Ruiter(1997)]. 이 경우 tuning fork 센서의 공명 특성이 비대칭적이고 신호가 0이 되는 영역을 저주파수 영역에 생성시킬 수 있다면 배경 잡음 역시 감소시킬 수 있을 것이기 때문이다.

다양한 실험을 거친 결과 모서리를 깎아낸 비대칭 형태의 PZT를 여기 진동자로 사용할 경우 tuning fork 센서가 비대칭적인 공명 특성을 지님을 확인하였다. 특별히 tuning fork 센서의 Q-factor를 2500 이상으로 증가시켰으며, 무엇보다도 배경 잡음을 거의 0이 되도록 줄였다. 그림 5에 보이는 바와 같이 Blue ray disc의 표면 형상을 측정한 결과 개선된 거리조절 방법은 vertical stability가 2nm 이내로 탁월한 성능을 보였다.

2. 시간 고분해능 측정 장치와 공간 고분해능 측정 장치의 결합

제2차년도의 목표인 100 nm 공간분해능, 10 ps 시간 분해능을 갖는 시공간 고분해능 비선형 광특성 측정 시스템을 구성하기 위하여 Time-Correlated Single Photon Counting (TCSPC) 시스템을 공간 고분해능 비선형 광학 측정 및 계측 기술에 접목하였다. TCSPC 시스템은 시료에서 나오는 형광의 세기가 매우 약해서 단일 광자의 방출 확률분포 상태에 이르렀을 때, 반복 측정에 의해 축적되는 시간상의 히스토그램이 형광세

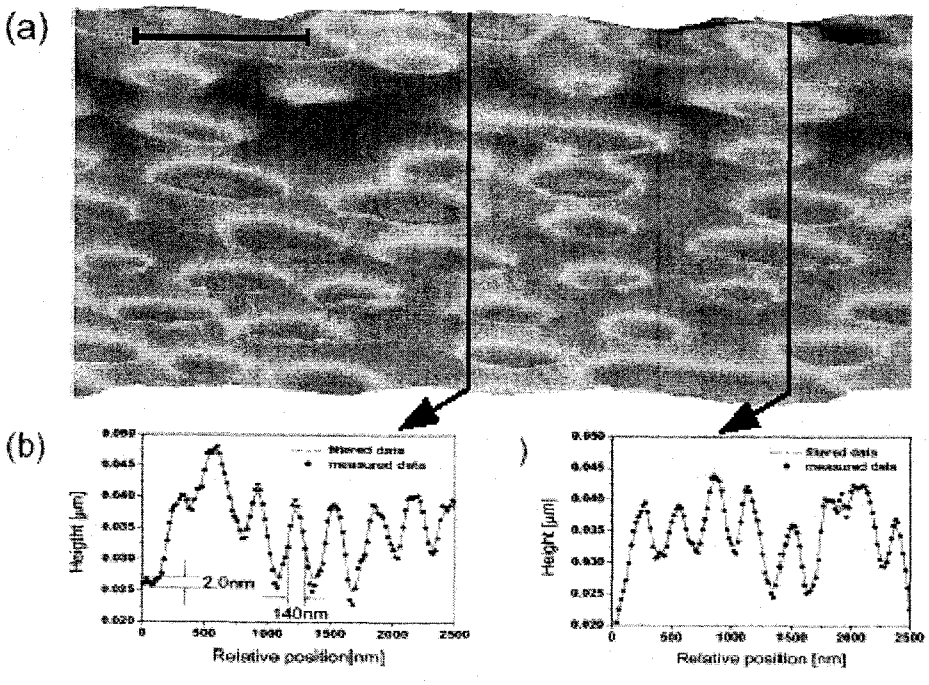

그림 5. 근접장 광학현미경으로 측정한 Blue ray disc의 표면 형상

기의 시간적 분포와 같다는 원리에 기반을 두고 있다. 이때 여기광원은 반복율이 높은 주기적인 펄스를 사용하며, 각각의 펄스를 시간상의 기준점으로 둘 때 한 주기 내에서 단일 광자가 검출기에 도달한 시점을 기록함으로써 형광의 소멸곡선을 재구성하게 된다 [O'Connor(1984)].

여기광에 의해 시료에서 방출된 형광은 분광기를 거쳐 MCP-PMT로 검출된다. MCP-PMT에서 전기적인 신호로 변환된 신호는 Pre-Amp를 거쳐 증폭된 후, CFD (Constant Fraction Discriminator)에 입력된다. 신호를 잡음에서 분리해내는 discriminator의 일종인 CFD는, 특히 펄스 진폭이 일정치 않은 경우에도 신호를 정확히 추출해 낼 수 있는 것으로 알려져 있다. 이렇게 CFD로부터 얻은 신호는 시작 신호로서 레이저 다이오드 드라이버에서 나오는 Sync 신호와 함께 TDC (Time to Digital Converter)로 입력된다. TDC는 TAC (Time to Amplitude Converter)와 ADC (Analog to Digital Converter)가 결합된 시스템과 같은 역할을 수행한다.

이와 같은 TCSPC 법을 이용한 시간 고분해능 비선형 광특성 측정 기술은 잘 확립되어 있으며, 국내 몇몇 연구진에서도 극초단 펄스 레이저를 광원으로 하여 초고속 동력학에 관한 연구를 활발히 진행하고 있으나, 시간적으로 분해능이 우수하면서 동시에 공간해상도를 높인 비선형 광특성 측정 기술을 보유한 그룹은 거의 없는 실정이다.

본 연구실에서는 10ps 영역의 시간 분해능을 지니는 TCSPC 시스템을 구성하고, 이를 공간 고분해능의 근접장 광학 현미경과 결합하여 그림 6과 같은 10ps/100nm 시공간 분해능의 비선형 광특성 측정 장치를 구성하였다.

여기광원으로는 PicoQuant 사의 picosecond 다이오드 레이저(LDH-P-C-400)를 사용하였다. 이 레이저 다이오드는 발진 파장이 402 nm로서 가시광 영역에서 형광을 내는 시료를 여기하는 데에 적합하다. 반복율은 최대 40 MHz까지 낼 수 있어서 TCSPC 실험에 알맞으며, 평균 power는 1 mW 정도이다. 펄스폭은 제작사에서 직접 측정한 바에 의하면 검출장치의 IRF (Instrument Response Function) 값인 30 ps 이 convolution 된 상태에서 60 ps 정도임을 알 수 있었다. 그러므로 실제 펄스폭은 이보다 짧은 40 ps 정도로 추정된다.

여기광원은 tapered optical fiber probe 에 결합하여 조사하게 하였으며 방출된 빛 혹은 형광은 현미경 대물렌즈로 수광하여 32cm 분광기를 거쳐 MCP-PMT로 검출하

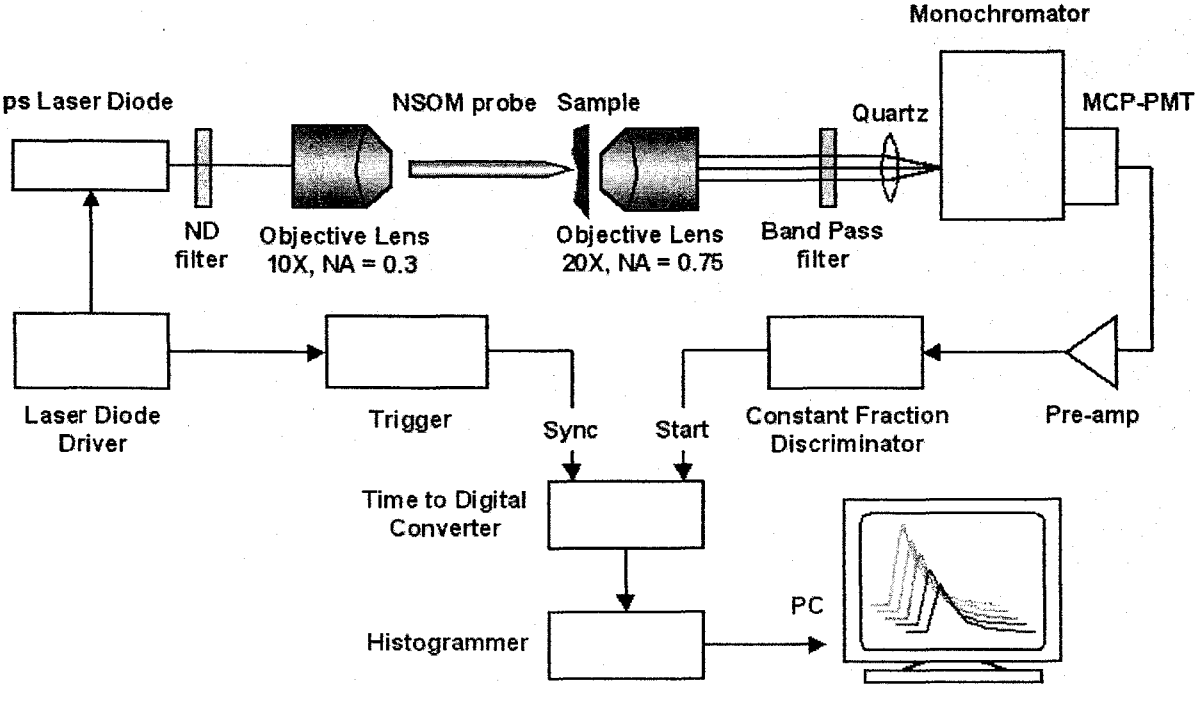

그림 6. 10ps/100nm 시공간 시공간 고분해능 비선형 광특성 측정 시스템

였다. MCP-PMT는 Hamamatsu 사의 R3809U-51 모델을 사용하였는데, 측정된 IRF값은 41.8 ps 이다. MCP-PMT는 -30℃로 냉각시켜 dark count를 최소화하였으며, -3000V라는 고압에서 작동하므로 냉각수에 의한 습기로 인해 누전되는 것을 방지하기 위하여 냉각기 내를 질소 가스로 충전하였다. MCP-PMT에서 전기적인 신호로 변환된 신호는 PicoQuant 사의 inverting pre-amp (PAM 102-T)를 거쳐 증폭된 후, TCSPC board (PicoQuant, TimeHarp 200)의 start 입력단자로 입력하였다. start 신호는 곧바로 CFD에 입력되어, 레이저 다이오드 드라이버에서 나오는 Sync 신호와 함께 TDC 로 입력된다.

시공간 고분해능 측정 장치의 작동원리는 다음과 같다. 근접장 탐침을 한 지점에 위치시킨 후 그 지점에서 TCSPC 측정을 수행한다. 측정이 완료되면 scanner로 시료를 움직여 그 다음 위치에서 동일한 TCSPC 측정을 반복한다. 이와 같은 과정을 측정하고자 하는 전 영역에서 반복하여 얻은 데이터는 공간상의 2차원 정보와 시간에 따른 변화를 동시에 보여준다. 본 연구실에서는 TCSPC 분광장치와 공간 고분해능의 근접장 광학 현미경을 구성하고 결합하여 10ps/100nm 시공간 분해능의 비선형 광특성 측정 장치를 성공적으로 구성하였다.

제 3 절 단일 탐침 / Tapered Optical Fiber Probe Interconnection

본 연구실에서 개발한 나노 탐침 슬라이드의 장점 가운데 한 가지는 탐침-탐침 interconnection [Yatsui(1997)]이 매우 단순한 방식으로 가능하다는 점이다. 그 이유는 기존 광섬유 탐침의 경우 매우 뾰족한 첨두형이므로 두 탐침을 수 nm 영역 내에서 연결시키기 위해서는 대단한 노력이 필요하며 더 나아가 응용 가능성이 거의 없다. 그러나 나노 탐침 슬라이드의 경우에는 평면형 탐침이므로 기존 광섬유 탐침이 쉽게 근접장 영역에 접근할 수 있고, 탐침 위에 고강도 Si_3N_4 나노 Slide가 장착되어 있어서 아무런 어려움 없이 두 탐침의 interconnection을 이룰 수 있었다.

그림 7은 interconnection을 위한 장치도이다. 나노 탐침 슬라이드를 제어하기 위하여 3축 나노 변위기를 장착하였고 100nm 직경의 광섬유 탐침을 tuning fork에 부착

하여 거리 유지를 하였다. 광섬유 탐침에 488nm Ar 레이저 빔을 입사시켜, 나노 탐침 슬라이드를 통과해 나오는 빛을 수광하여 CPM(Channeled Photomultiplier tube, Perkin Elmer Inc.)으로 얻었다. 광섬유 탐침이 나노 탐침 슬라이드와 interconnection 된 실제 영상과 결과 값을 그림 8에 보였다. SEM 측정 결과 130×170nm 크기의 기하적인 개구를 지니는 나노 탐침 슬라이드의 근접장 영역에서 2차원 주사를 수행함으로써 광 영상을 얻었다 (그림 8(b)). 그림에 표시된 지시선에 해당하는 세기 곡선은 각각 그림 8(c), (d)이며 260nm와 340nm의 반치폭을 보였다. 이 결과는 2차원 평면상 200-300nm 영역 안에서 interconnection이 이루어짐을 의미한다. 탐침-탐침 interconnection 기술은 향후 단일 양자점 광특성 분석, 의료/생명공학 분야의 연구, 나노 광학 소자 개발 등으로의 응용이 기대된다.

제 4 절 Nonlinear Kerr Film의 비선형 특성 연구 및 분석

본 연구실에서는 Si_3N_4 탑재 탐침 Slide를 이용한 공간 고분해능 비선형 측정기술 개발과 아울러서 기존의 광섬유 탐침을 이용한 근접장 광학 현미경을 개선하여 Nonlinear Kerr Film의 비선형성을 측정하였다. 특히 자체집광 현상의 측정 및 분석을 파장 이하의 공간분해능으로 측정하기 위하여 근접장 광학 현미경을 이용하였다. 자체집광(self-focusing) 현상은 대표적인 광학적 비선형 현상 중 하나로서, 이를 이용하여 물질의 비선형성을 측정하는 연구가 많이 이루어져 왔으며, 근래에는 회절한계 이하의 크기를 갖는 spot을 형성시키기 위한 도구로서 고려되고 있다.

1. Nonlinear Kerr Film의 비선형성에 관한 이론적 고찰

본 연구실에서는 As_2S_3 박막의 자체 집광 현상을 관측, 분석하기 위하여 근접장 비선형 광 측정 연구와 Finite-Difference Time-Domain (FDTD) 시뮬레이션 기법을 이용한 이론 연구를 병행하였다. 이제까지 자체 집광 현상의 분석 및 예측에는 non-paraxial Beam Propagation Method (BPM) 방법이 많이 이용되어 왔다

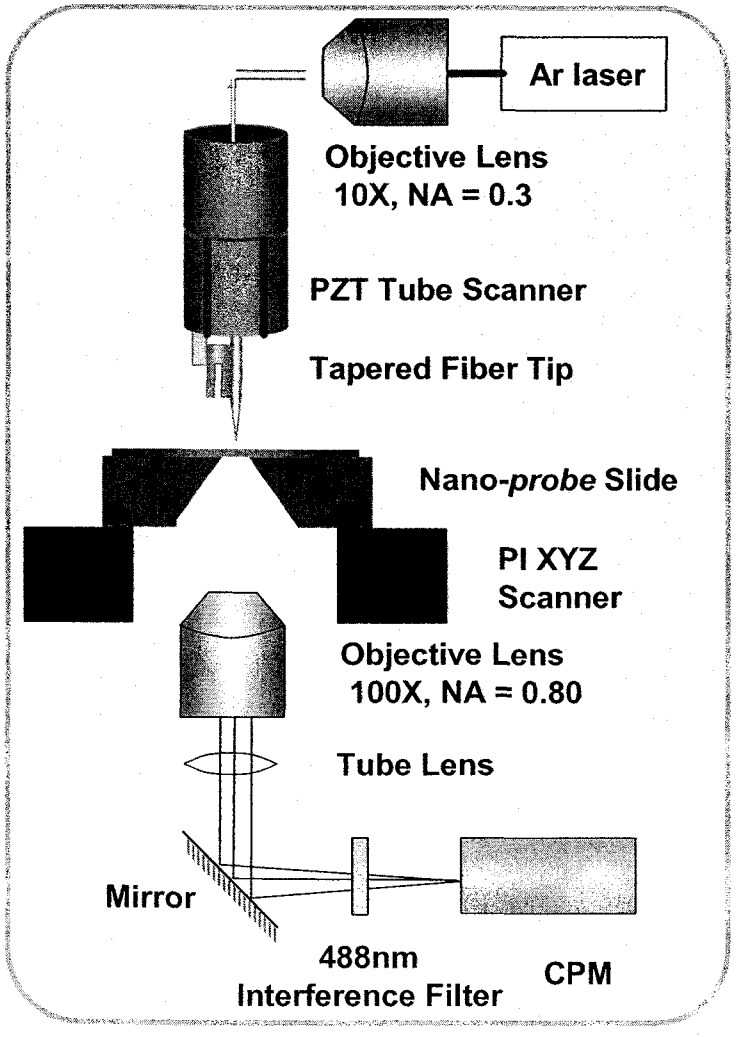

그림 7. 탐침-탐침 Interconnection 장치도

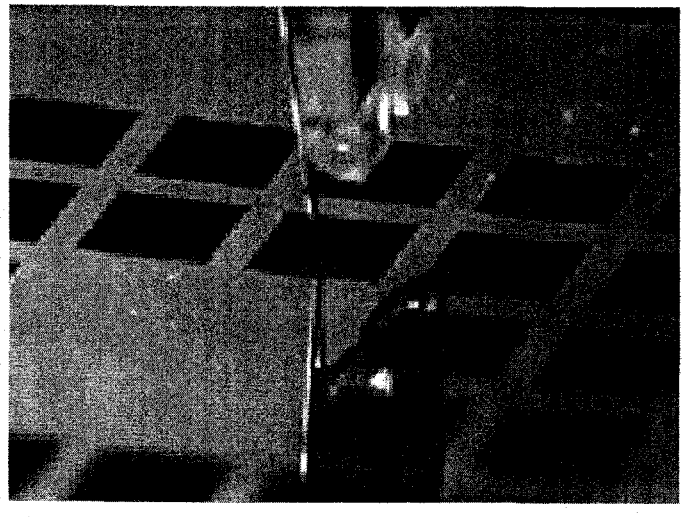

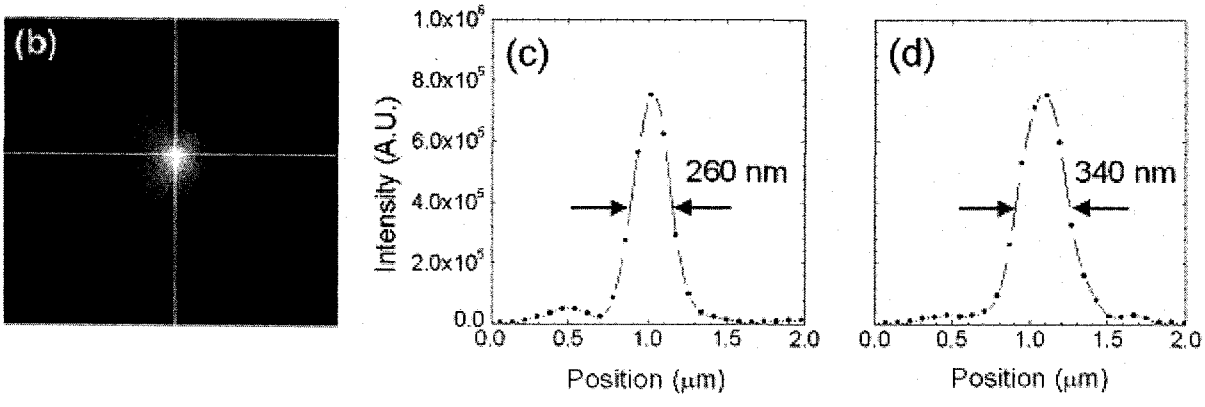

그림 8. 나노 탐침 Slide와 광섬유 탐침 interconnection

[Feit(1988)]. 그러나 박막에서는 다중 반사가 자체 집광에 많은 영향을 주므로 BPM 방법으로는 효과적인 결과를 얻기가 어렵다. 박막에서 자체집광 현상에 영향을 줄 수 있는 요소인 박막의 두께, 파장, 빔 세기 분포 등은 자체집광에 의한 최소 spot 크기와 형태에 직접적인 영향을 줄 수 있다.

본 연구에서는 박막의 두께, 파장, 입사빔 세기 분포 및 편광 방향 등을 고려하여 체계적으로 자체 집광 현상을 연구하여, 입사빔의 편광 방향과 박막에서의 Nonlinear Fabry-Perot Etalon 효과에 의해 박막 근처의 근접장 영역에서 비대칭적인 광분포가 발생할 수 있음을 발견하였다(그림 9). Bulk 상태의 비선형 물질에서는 자체 집광에 의한 비대칭 광분포가 발생한다는 이론적인 예측이 있었고[Fibich(2000)], 최근 들어 실험적으로 관측된 바도 있다[Song(2000)]. 하지만 비선형 박막에서도 이러한 현상이 일어남을 예측할 수 있었고, 더 나아가서 최소 spot이 발생하는 위치가 박막으로부터 일정 거리만큼 벗어난 곳에 맺히는 사실을 알아내었다. 또한 FDTD 시뮬레이션을 통해 근접장에서 일어나는 세기 분포들이 비선형 박막의 경우 fs 영역의 매우 짧은 시간 내에서 변화하다가 수렴함을 알 수 있었다.

2. 근접장 광학 현미경을 이용한 As_2S_3 박막의 자체 집광 현상 관측

한편 이론적인 시뮬레이션과 함께 근접장 광학 현미경을 이용하여 As_2S_3 박막으로부터 일어나는 자체 집광 현상을 관측하였다. As_2S_3 박막은 비선형 굴절율이 충분히 커서 수 mW의 CW 레이저로도 비선형성을 일으킬 수 있었다. 100nm 직경의 광섬유 탐침을 수광부로 사용하여 2차원 평면상을 주사하였으며, FDTD 시뮬레이션 결과로부터 예측한 바를 검증하기 위하여 박막 표면으로부터 z 축상으로 거리를 변화시켜가며 영상을 얻었다(그림 10). 측정 결과 이론적으로 예측한 자체 집광에 의한 multiple filamentation 현상을 As_2S_3 박막으로부터 명백히 관측할 수 있음을 알 수 있었다.

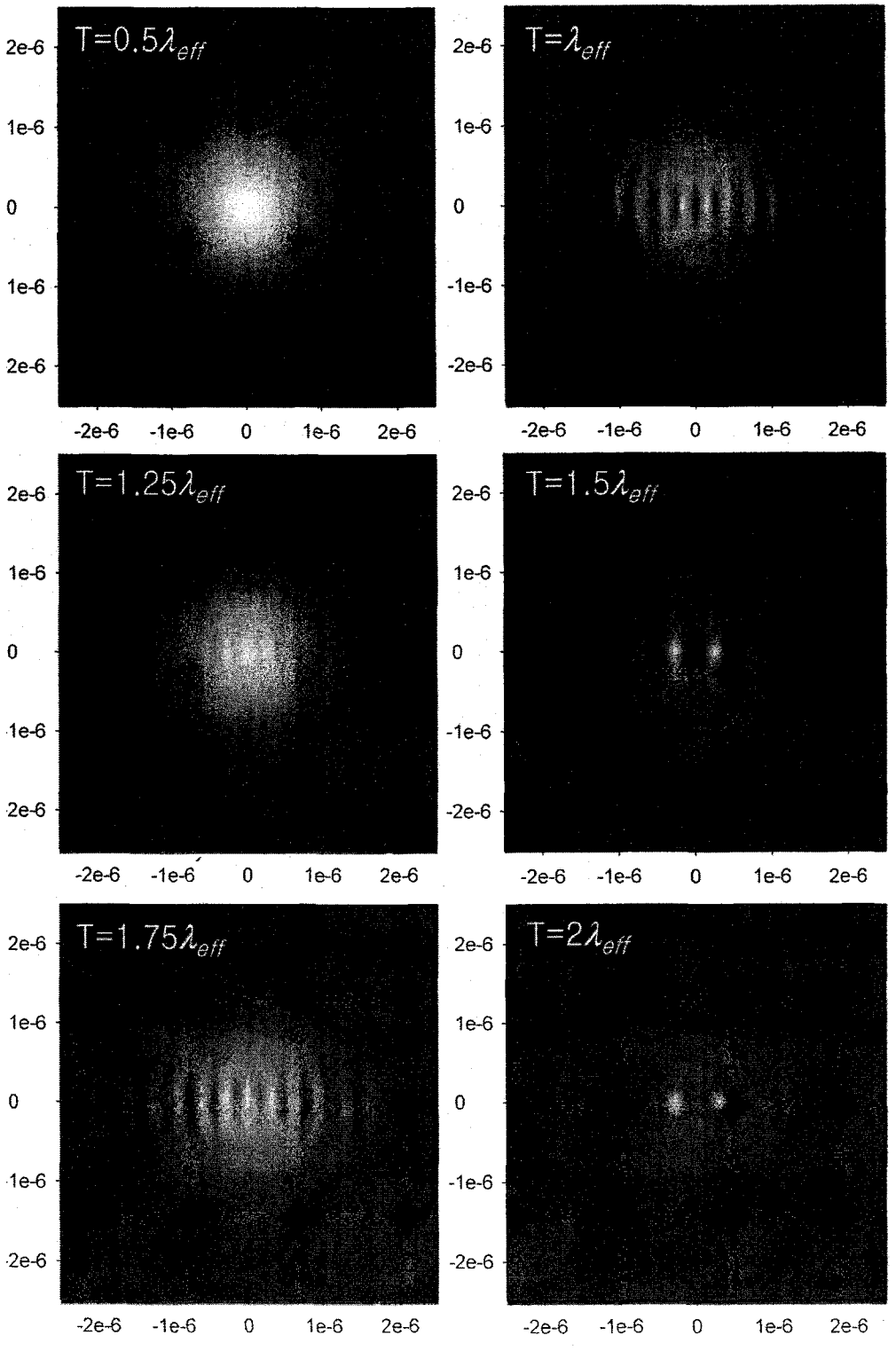

그림 9. Nonlinear Kerr Film에 대한 FDTD Simulation 결과

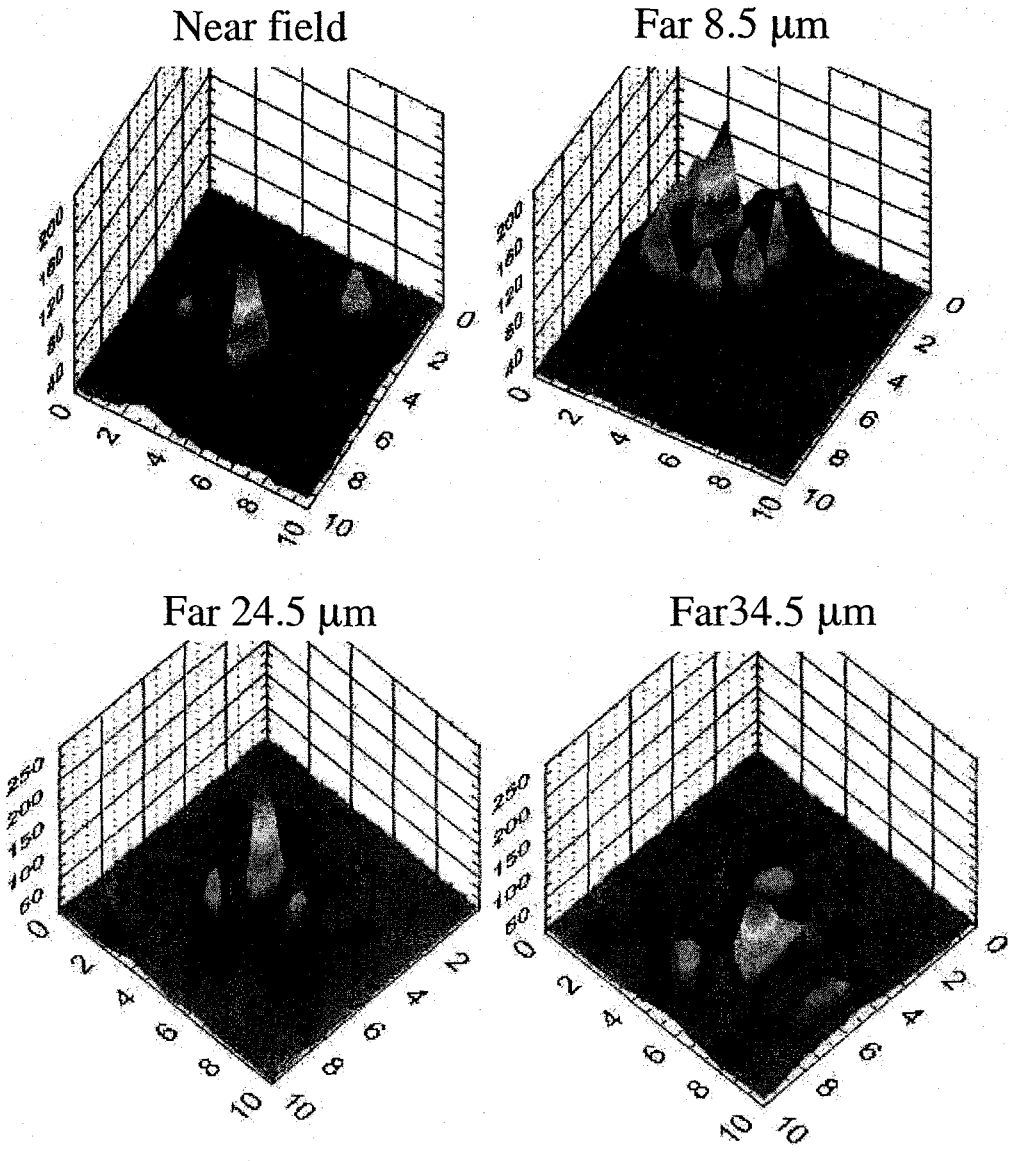

그림 10. 거리에 따른 As_2S_3 박막의 Multiple-Filamentation 관측 결과

제 5 절 금속-반도체 복합 나노 입자 제조 및 특성 분석

반도체 양자점과 같은 나노 입자는 특별한 광학적, 전기적, 화학적 성질을 띠고 있기 때문에 관심을 끄는 물질계이다. 반도체 양자점 제조법은 매우 다양하지만 최근에 개발된 화학적 반응에 의해 제조하는 콜로이드 상태 양자점은 유리 매질 내의 양자점보다도 안정적이고, 양자점이 액체 내에 부유하는 상태이기 때문에 다양한 응용 가능성이 있어서 많은 연구진에서 연구하고 있다[Alivisatos(1998)]. 특별히 상온에서 감마선 조사에 의한 콜로이드 양자점 생성법이 새롭게 선보여 매우 활발히 연구되고 있는데, 이러한 양자점은 반응 과정 중에 시료의 크기를 모니터링할 수 있다는 장점이 있다[Mostafavi(2000)].

일반적으로 콜로이드 양자점은 그 외부에 capping ligand를 더하여 제조하는데, 이러한 외부층은 양자점끼리 뭉치는 현상을 방지하고 액체에 잘 결합되어 부유하게 하며, 나아가서는 광학적으로 양자 효율을 높이는 역할까지 한다. 이와 같은 코어-쉘 구조의 나노 입자는 한 물질로만 이루어진 나노 입자에 비해 특이한 물리적 특성을 지니기 때문에 새로운 연구 주제로 떠오르고 있다[Halas(2002)]. 본 연구진은 이와 같은 코어-쉘 구조를 반도체-금속 복합 나노 입자로 제조하는 것을 제안하였다. 표면에 금속을 입힌 반도체 나노 입자의 광학적 성질은, 표면 플라즈몬과의 상호작용 혹은 field enhancement 현상으로 인해 기존 나노 입자와는 완전히 다른 성질을 갖고 있으리라 기대된다.

1. CdS/Ag 복합 나노 입자의 제조

본 연구진은 프랑스 ICMCB-CNRS연구소와 공동 연구를 통해 CdS 양자점 및 CdS/Ag 복합 나노구조를 성공적으로 제조하였다. 모든 과정은 산화를 막기 위해 질소 가스 분위기에서 진행하였다. 우선 10^{-3} M의 Cd^{2+} 용액을 얻기 위해 $CdSO_4$를 고순도 증류수에 녹였다. 동시에 2-mercaptoethanol ($HOCH_2CH_2SH$)을 Na_3PO_4 buffer solution 에 섞어 10^{-1} M의 2-mercaptoethanol 용액을 얻었다. 세 번째 단계로 두 용액을 pH 7.5에서 각각 1:100, 1:200, 1:300의 비율로 혼합하였다. 그 뒤 2500 Ci의 ^{137}Cs

감마선을 0.3 kGy, 0.6 kGy, 0.9 kGy 조사량으로 용액에 조사하였다. 이때 수소화 전자 e^-_{aq} 가 환원제로 작용하여 CdS 양자점을 생성시킨다. 마지막으로 금속 코팅된 양자점을 제조하기 위해 Ag_2SO_4를 녹여 만든 은 용액을 첨가하여 Ag로 CdS 양자점 표면을 두르게 하였다.

제조된 CdS/Ag 복합 나노 입자의 구조를 관측하기 위해 고배율 TEM 사진으로 관측하였다(그림 11). 그림에서 보는 바와 같이 1 영역과 2 영역이 다른 물질임을 분간할 수 있다. TEM 사진으로부터 얻은 격자 상수를 JCPDF file에 있는 CdS 및 Ag 의 값과 비교한 결과 1 영역은 CdS 양자점이며 2 영역은 Ag 임이 밝혀졌다. 즉 CdS 양자점 위에 Ag 나노 결정이 성공적으로 생장되어 CdS/Ag 복합 나노구조의 제조에 성공하였다.

2. CdS/Ag 복합 나노 입자의 광학적 특성

흡수 스펙트럼을 측정한 결과 Ag 입자가 CdS 양자점 위에 증착된 복합 나노 구조의 경우 3.0 eV와 4.25 eV 사이에 두 개의 흡수 봉우리가 생김을 확인하였다(그림 12). 가우시안 맞춤에 의해서 3.36 eV 에 생긴 것으로 확인된 봉우리는 CdS 양자점의 흡수 스펙트럼에서는 관측되지 않았으므로 Ag 에 기인한다. 이는 CdS 양자점 위에 증착된 Ag 나노 입자의 표면 플라즈몬 흡수 공명이 분명하다. 이뿐 아니라 CdS 양자점에 의한 exciton 봉우리가 강한 Local Field에 의한 비선형성으로 인하여 적색 편이함을 관측할 수 있었다. 이와 같은 실험결과를 해석하기 위해 effective-mass Hamiltonian 방법을 사용하여 양자점에 외부 전기장이 걸려 있을 때 흡수 봉우리의 변이를 계산해 보았다. 그 결과 스펙트럼 상에서 나타난 0.09eV 의 적색 변이는 약 1×10^6 V/cm의 국소 전기장이 양자점에 인가되어 생긴 것으로 추정된다. 새롭게 제조된 금속-반도체 composite 나노 입자는 반도체와 금속의 상호작용을 나노미터 수준에서 관측할 수 있다는 점에서 fs dynamics 연구 분야의 발전을 촉진할 것으로 기대된다.

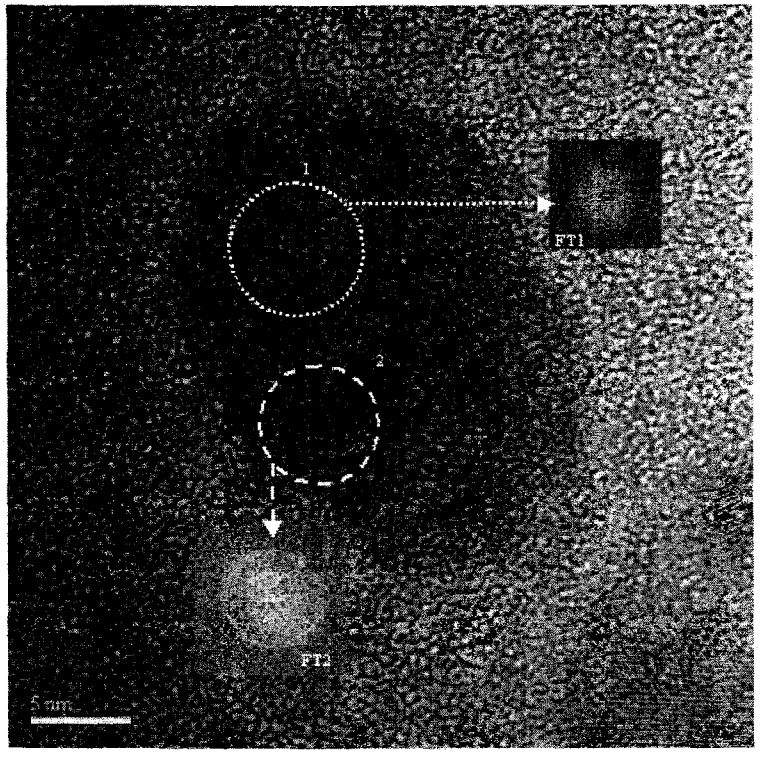

그림 11. CdS/Ag 복합 나노구조의 고배율 TEM 사진

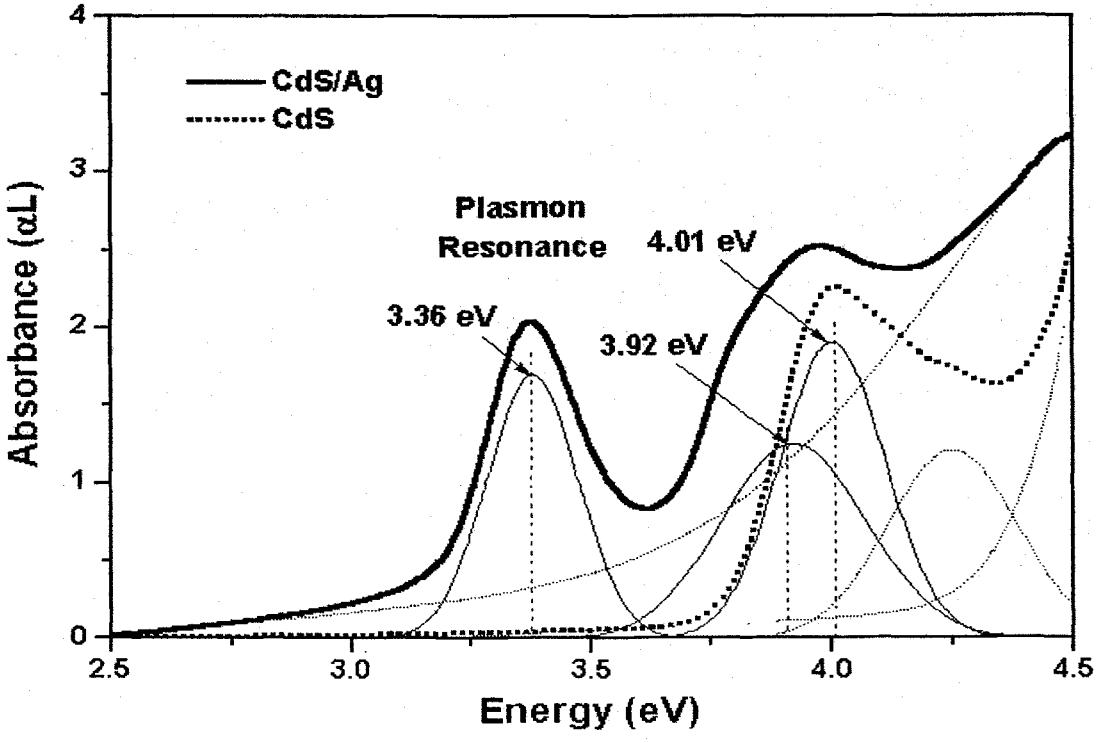

그림 12. CdS 양자점 및 CdS/Ag 복합 나노구조의 흡수 스펙트럼

제 6 절 근접장 위상천이 간섭계 개발

근접장에서의 광학적인 위상정보에 관한 근본적인 연구는 매우 관심있는 주제임에도 불구하고 이제까지 거의 다루어지지 않은 분야인데, 이는 적절한 연구 방법이 없었기 때문이라고 사료된다. 본 연구진은 근접장 현미경의 탐침을 점광원으로 응용하여 위상천이 간섭계와 결합함으로써 공간 고분해능 위상정보를 근접장 영역에서 얻을 수 있었다. 근접장 주사 위상천이 간섭계의 원리는 광섬유 탐침에서 반사된 빛과 시료의 표면에서 반사된 빛이 간섭을 일으키게 함으로써 고분해능의 위상정보를 근접장 영역에서 얻어내는 것이다. 제안한 근접장 주사 광간섭계는 그림 13과 같이 구성하였다.

근접광을 관측하기 위해서는 사용하는 광의 파장보다 작은 직경의 광섬유 탐침을 이용하고 시료와 탐침 간 거리를 파장보다 짧게 유지시키는shear-force 검출에 의한 시료-탐침 간 거리 유지가 필수적이다. Shear-force 검출은 수정 진동자(tuning fork)의 공명특성을 이용하는 방법이 널리 사용되고 있다. 광섬유 탐침의 끝단은 $50nm$ 정도의 열린 개구와 그 주위에 $200nm$ 정도의 두께로 금속 코팅된 구조를 가지고 있어서, 끝단으로부터 반사된 광이 새로운 점 광원을 만들기 위한 적합한 모양을 가지고 있다. 탐침은 위치의 이동도 자유롭고, 탐침에서 반사된 광과 시료 표면에서 반사된 광을 서로 간섭시킨 상태에서, 탐침의 끝단을 $\lambda/8$씩 이동 시키면서 $\lambda/4$씩 위상천이 된 4장의 간섭무늬를 측정하고, 측정한 간섭무늬에 위상천이 알고리즘을 적용함으로써 초점에서의 파면수차를 구할 수 있도록 하였다.

그림 14는 개발한 고분해능 근접장 주사 광간섭계를 이용하여 폴리머 박막에서 얻은 근접장 영상과 표면 형상이다. $3\times3\mu m$ 주사 영역 안에서 폴리머 박막에 외부 압력을 가해 생긴 내부 균열을 측정하였는데 외부적인 형상에서는 볼 수 없는 복잡한 내부 구조를 광학적 위상 측정을 통해 밝혀낼 수 있다. 이때 광학적 위상 측정을 통해 얻은 정보는 100nm 보다 훨씬 좋은 광학적 해상도를 가지고 있었으며 이는 표면 형상의 경우보다 월등히 뛰어났다. 이와 관련된 2건의 특허를 출원하였고, 본 연구결과는 Nature지에 투고할 예정이다.

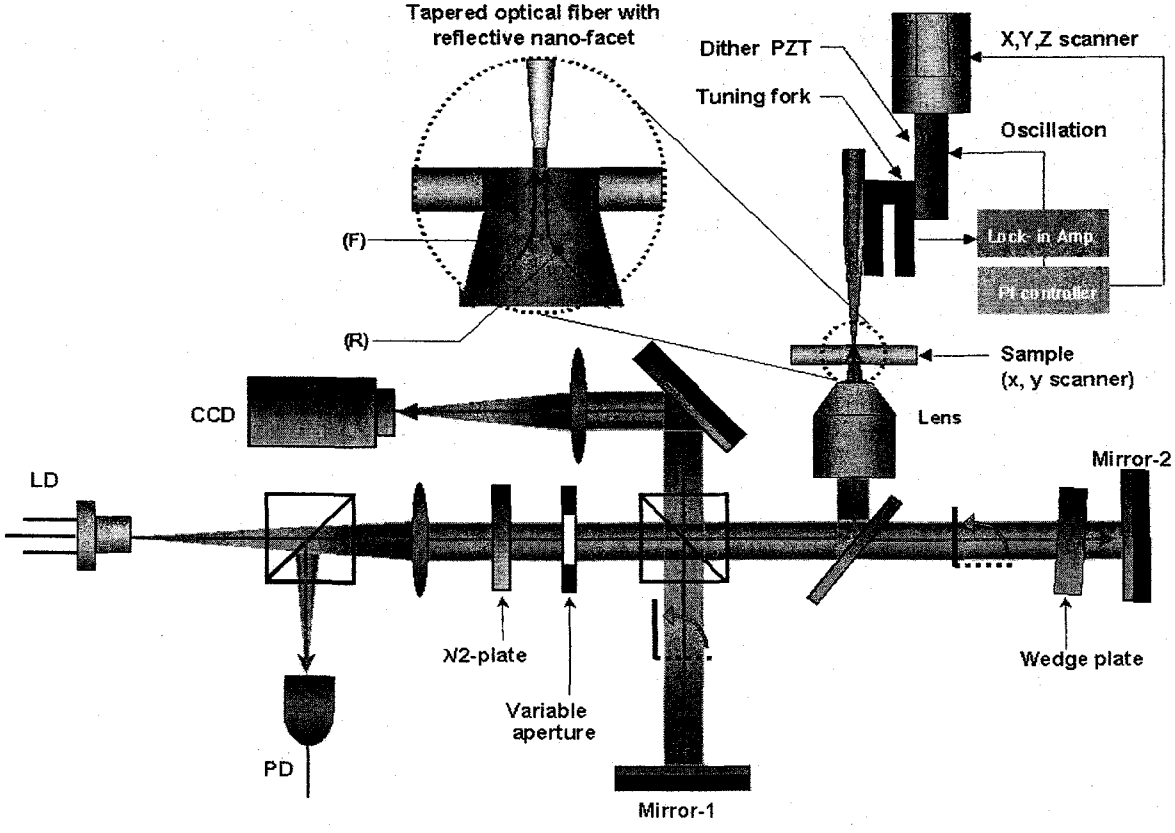

그림 13. 고분해능 비선형 시료측정 및 근접장 파면 측정 장치도

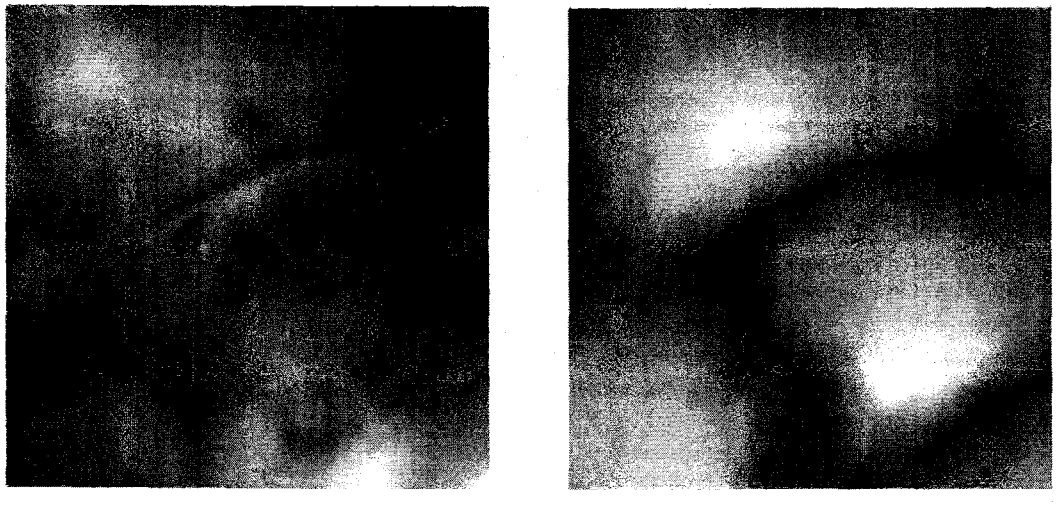

그림 14. 근접장 위상 광영상(왼쪽) 및 형상 (오른쪽). 전체 영역은 3×3μm임

제 4 장 연구목표 달성도 및 관련분야에의 기여도

제 1 절 연구목표 달성도

연도	세부연구목표	달성내용	달성도
1차년도	신기능성 단일 나노 탐침 Slide 제작	신기능성 나노 탐침 Slide를 제안하고, 표준적인 Si 반도체 공정을 이용한 100nm급의 나노 탐침 Slide를 성공적으로 제작하였음.	100%
	고분해능 비선형 광특성 측정 시스템 개발	신기능성 나노 탐침 Slide를 nm 급 제어 변위기 위에 장착하여 100nm급 고분해능 공간 해상도의 광특성 측정 시스템을 개발하였음. 또한, ICCD를 분광기에 동시 장착하여 비선형 광특성 검출의 Dynamic Range를 증대시켰음.	100%
	SCI 논문 2, 국내논문 3편, 특허 1건	SCI 논문투고 3편, 국내논문 2편, 해설 논문 1편을 게재하고, 2건의 특허를 출원하였음.	100%
2차년도	신기능성 탐침 Array Slide 제작 기술	대량 생산이 가능한 표준적인 반도체 공정의 장점을 이용하여 100nm급 5×5 나노 탐침 Array Slide를 성공적으로 제작하였음.	100%
	고분해능 탐침 Array Slide 응용 시간분해 비선형 광특성 측정기술 개발	100nm급 근접장 나노 탐침 Array Slide를 사용하여 고분해능 공간 해상도의 광특성 측정 시스템을 개발하였으며, 광섬유 탐침과의 interconnection에 성공하고, 시간상관 단일광자 계수 장치를 결합함으로써 10 ps 시간분해능의 비선형 광특성 측정 시스템을 개발하였음. 또한, 근접장 위상 측정 기술과 3차원 FDTD 분석 기술을 확보하였음.	150%
	나노구조 비선형 형광/흡수 측정/분석	반도체-금속 복합 나노 구조의 비선형 흡수 스펙트럼을 측정/분석하였음.	80%
	SCI 논문 2, 국내논문 3편, 특허 1건	SCI 논문투고 11편, 국내논문 2편, 해설 논문 1편을 게재하고, 2건의 특허를 출원하였음.	100%
종합	100nm 공간분해능, 10ps 시간분해능 비선형 광특성 측정 기술 확립	100nm급 근접장 나노 탐침 Slide를 제작하고 이를 이용하여 100nm급 고분해능 공간 해상도의 광특성 측정 시스템을 개발하였으며, 이 시스템에 ICCD와 시간상관 단일광자 계수 장치를 결합함으로써 10ps의 시간분해능을 갖는 비선형 광특성 측정 시스템을 개발하였음. 또한, 근접장 위상 측정 기술과 3차원 FDTD 분석 기술을 확보하였음.	100%
	SCI 논문 4, 국내논문 6편, 특허 2건	SCI 논문투고 14편, 국내논문 4편, 해설 논문 2편을 게재하고, 4건의 특허를 출원하였음.	100%

제 2 절 관련 분야 기여도

1. 비선형 광학 기술 관련 홈페이지 운영

"http://phya.yonsei.ac.kr/~optics" 운영하고 있음.

2. 산·학·연 협력거점 활동

▸ 삼성전자 (Samsung Electronics AMLCD Division)
- 내용: 투명 전도막의 전기적/광학적 특성 협력 연구
- 성과: J. Korean Phys. Soc. 44, 956 (2004) / 한국광학회지. 1, 455 (2002) / Appl. Phys. A 79, 109 (2004) 공동발표

▸ 삼성종합기술원 (Samsung Advanced Institute of Technology)
- 내용: 적외선 흡수 분광을 이용한 혈청검사 협력 연구
- 성과: J. Opt. Soc. Kor. 7, 240 (2003) 공동발표

▸ 한국 원자력 연구소 양자광학기술개발부
- 내용: 자유전자 레이저를 응용한 금속의 광학상수 측정 협력 연구
- 성과: 한국광학회 (전남대학교, 2004. 2. 12 - 13) 공동발표

3. 기술지도

▸ 초정밀 광파면 측정 기술지도
- 일시: 2003. 2. 20
- 업체: 삼성전자 메카트로닉스 센터, 방문자: 김부태 부장 / 서제완 과장

▸ 고분해능 고감도 NSOM 측정 기술지도
- 일시: 2003. 12. 18
- 업체: 삼성전자 디지털 미디어 연구소, 방문자: 윤두섭 수석 / 노명도 수석

▸ 정밀 광학기기 측정 기술지도

- 일시: 2004. 3. 11
- 업체: 삼성전기
- 방문자: 장학현 부장 / 박천호 차장

▸ 근접장 주사 광현미경의 원리 소개

- 일시: 2004. 4. 22
- 업체: SKC
- 방문자: 오세진 부장 / 신민경 대리 / 김경록 대리

4. 국내외 연구기관과의 상호기술교류 협정 체결

▸ The Institut de Chemie de la Matiere Condensee de Bordeaux, France

▸ Centre de Physique Moleculaire Optique, Talence, France

▸ Institut für Physikalische Chemie, Universität Göttingen, Germany

▸ 고등광기술연구원 (GIST, Korea)

▸ FORSCHUNGSZENTRUM, Karlsruhe GmbH, Germany

5. Workshop 및 Seminar 개최

▸ The 4th Workshop on Vision and Medical Optics

- 일시: 2003. 5. 30
- 장소: 연세대학교 원주캠퍼스 의료기기진흥센터 대강당

▸ International Workshop on Nanophotonics 2003

- 일시: 2003. 10. 20
- 장소: 연세대학교 공학원 259호

▸ The 1st STAR Workshop on Light-Matter Interation in Nanostructures

- 일시: 2003. 11. 25, 장소: 한국과학기술연구원

▸ Seminar 개최 실적

• 10회/년 이상 개최

6. 기술교류 & 자문활동

▸ 기술교류

- 복합다체계의 양자현상 NRL 기술교류회 참여

▸ 자문활동

- 광학 특성 측정과 간섭계에 관한 자문 및 강연
  - 장소: 삼성전기 광디바이스 사업부
  - 일시: 2003. 6. 9
- 비선형 광계측 기술에 관한 자문 및 교육
  - 장소: K-JIST 고등광기술연구소
  - 일시: 2002. 8. 8

제 5 장 향후 연구개발 계획 및 활용계획

제 1 절 향후 연구개발 계획

본 연구개발은 "시공간 고분해능 대면적 비선형 광특성 측정 기술 개발"이라는 최종목표를 설정하고 수행된 총 2단계 5년의 연구과제 중 1단계에 해당한다. 본 연구실은 1단계 연구개발을 통해 공간해상도 100 nm, 시간분해능 10 ps의 비선형 광특성 측정 기술을 확립하였다. 연구개발을 통해 본 연구실에서 독창적으로 개발한 신기능성 탐침 Slide를 배열형태로 제작함으로써 대면적 비선형 광특성 측정 기술 개발의 기반을 마련하였으며, 단일 탐침 Slide와 tapered optical fiber probe의 interconnection을 수행하였다. 또한 비선형 현상 가운데 하나인 자체집광 현상을 보이는 As_2S_3 박막에 대한 FDTD 시뮬레이션과 근접장 광측정으로 최소 spot 이 형성되는 위치나 multiple filamentation 현상 등을 예측하거나 관측하였다. 이와 함께 표면 플라즈몬과의 상호작용이 두드러지게 나타나는 금속-반도체 복합 나노 입자를 제안, 제조함으로써 새로운 연구 주제를 도출하였다. 이와 같은 물질계는 반도체와 금속 사이의 상호작용을 나노미터 수준에서 관측할 수 있다는 점에서 fs dynamics 연구 분야의 발전을 촉진할 것으로 기대된다.

이와 같은 연구성과를 바탕으로 2단계 연구 개발을 통해 시공간 고분해능 비선형 광측정 기술을 한 단계 더 끌어올리고자 한다. 2단계 연구 개발 과제는 1단계 연구 개발에서 얻은 다양한 측정 기법과 시뮬레이션 기법, 나노 물질 제조 기법 등을 체계화하고 최적화함으로써, 공간해상도 30 nm, 시간분해능 100 fs, 대면적 1mm×1mm 의 비선형 광특성 측정 기술 확립이라는 최종 목표를 달성할 계획이다. 아울러서 연구개발 과정 중 부가적으로 얻은 고분해능 광위상 정보 측정 기술과 근접장 파면 측정 기술을 비선형 광측정 분야로까지 확장함으로써 비선형 광측정에 관한 총체적인 연구를 도모하고자 한다.

▸ 공간 고분해능 단일 탐침 Si_3N_4 탑재 Slide의 설계 및 제작:

본 연구실에서는 회절한계를 넘어서는 고분해능 비선형 광특성 측정기술을 확보

하기 위하여 근래에 급속도로 발전하고 있는 근접장 기술에 관한 연구를 지난 수년간 수행하여 왔다. 근접장 검출에 쓰이는 광섬유 탐침은 throughput이 작고, 수명이 짧으며, 내구성이 떨어지는 단점이 있기 때문에 본 연구실에서는 새로운 개념의 고분해능 비선형 광학 측정 및 계측 연구를 수행하기 위한 신기능성 탐침 Slide를 고안하고 탐침 Slide의 최적 제작을 위한 공정과정을 연구하고 있다.(특허출원번호:2002-19474, 2003-30357, 2003-30359)

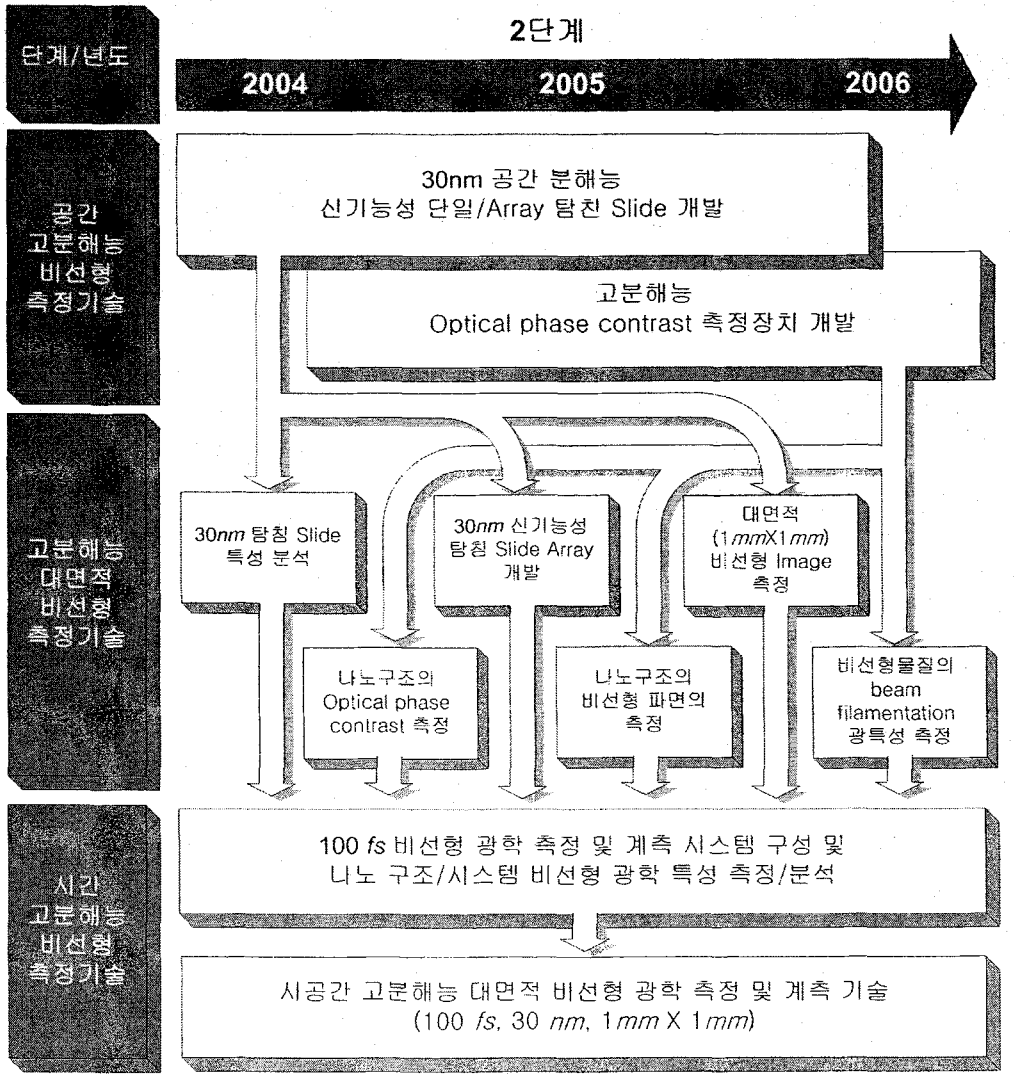

▸ 100fs/30nm 시공간 고분해능 비선형 광학 측정 및 계측 기술 개발:

본 연구실에서는 다양한 비선형 분광기법 및 시간분해 비선형 분광기법을 보유하고 있고 이에 더하여서 독창적인 개념의 탐침 슬라이드를 고안하고 실제로 제작한 경험이 있으므로, 단일 근접장 탐침 Slide의 개구 크기를 점차적으로 줄여 최종적으로 30nm 급의 공간 고분해능을 갖는 탐침을 제작하고 지금까지의 연구경험과 know-how를 바탕으로 100fs/30nm 시공간 비선형 광학 측정 기술을 체계적으로 개발하고자 한다.

▸ 고분해능 광위상정보(Optical phase contrast) 및 근접장 파면 측정기술:

생체시료나 폴리머시료와 같이 미시적인 세계에서는 무수하게 많은 시료들이 내부구조의 비밀을 포함하고 있기 때문에 시료에 영향을 주지 않고 투시할 수 있는 기술이 요구된다. 빛은 굴절률에 따라 광학적인 경로를 달리하기 때문에 내부구조의 변화를 인지하는 유용한 수단으로 활용될 수 있고, 빛이 전달하는 이러한 정보를 광학적 위상정보라고 한다. 본 연구에서는 비선형 특성을 포함한 광학적인 위상정보를 획득하기 위하여 그림 2와 같이 시료 표면에서 반사되는 신호(F)와 근접장 탐침의 끝단에서 반사된 신호(R) 사이의 간섭신호를 이용하고 시료 내부의 포함된 복잡한 정보를 얻고자 한다.(특허출원번호:2004-24445, 2004-24446)

제 2 절 연구 결과의 활용 가능 분야

- 신기능성 단일 탐침 Slide를 이용한 '시공간 고분해능 비선형 광특성 측정/계측' 기술은 향후 반도체 양자점을 비롯한 나노구조 연구 및 나노 소자의 개발과 특성 평가 분석, 그리고 생체시료의 고분해능 비선형 이미징 등에 활용될 수 있을 것으로 기대됨.
- 단일 나노 탐침 Slide와 Tapered Optical Fiber Probe의 interconnection 기술은 단일 양자점 분석 및 의료/생명공학 분야의 연구 개발에 활용될 수 있을 것으로 기대됨.
- 고분해능 위상 측정기술 및 FDTD Simulation 기술은 근접장 광정보 저장 기술 개발 및 고분해능 근접장 생체 시료 분석 등의 분야에 활용될 수 있을 것으로 기대됨.

제 6 장 연구개발과정에서 수집한 해외과학기술정보

▶ NSOM 장비 판매회사 및 회사별 최근 과학기술 동향

1) Nanonics(Israel 소재, http://www.nanonics.co.il) :

- 주로 AFM type의 NSOM이며, AFM controller에 AFM cantilever 대신 bent optical fiber probe를 부착하여 동작함.
- 완제품도 판매하나, 거의 모든 part를 개별적으로 판매함.
- applications:
  - failure analysis of microchips & optical properties of optoelectronic devices
  - polymer imaging, bacteriology & biotechnology
  - data storage applications
  - ultrafast laser spectroscopy
  - fluorescence imaging

2) Digital Instruments(USA 소재) --> 현재 Veeco 에 병합됨 :

- electronic controller가 매우 우수하여, home-made AFM 또는 NSOM 제작자들이 DI사의 controller를 즐겨 사용함.
- applications:
  - fluorescence imaging of a single molecule
  - poralization contrast in liquid crystal
  - metal mask imaging

3) Veeco Instruments (Topometrix병합, USA 소재, http://www.veeco.com) :

- Topometrix는 NSOM 장비 제작 회사로는 가장 많이 알려진 회사로서 NSOM 연구 초기부터 NSOM을 제작 판매하였으며, 주로 biological sample이나 fluorescence imaging에 치중. 현재 Veeco에 병합됨.
- applications:
  - biological fluorescence and absorption imaging
  - medical imaging
  - characterizing optoelectronic devices

- high density data storage & optical lithography
- polarization imaging of magneto optics and polymers
- spectroscopy

4) Jasco (일본 소재, http://www.jasco.co.jp) :

- 최근에 NSOM 제작을 시작하였으며, 저온 cryostat을 부착하여 판매.
- 주로 반도체 spectroscopy에 치중
- applications
  - CD ROM & grating surface scanning
  - PL imaging of bulk GaAs, GaAsP, quantum wire, quantum dots, Alumina
  - near-field Raman mapping of Polydiacetylene

5) WITec (독일 소재, http://www.witec.de) :

- 최근에 NSOM 제작을 시작하였음. AFM cantilever type probe를 특별히 제작된 대물렌즈에 mount함.
- applications:
  - 생체 시료, D-RAM 등

6) NT-MDT (Russia 소재, http://www.ntmdt.ru) :

- 광섬유 탐침 사용
- applications:
  - 생체 시료
  - optoelectronic device characterization
  - spectroscopy
  - chemical reaction control

7) DME (Denmark 소재, http://www.dme-spm.dk) :

- NSOM/AFM/STM 등의 호환성이 가능하도록 part 별로 구입 가능.
- applications:
  - optoeletronic devices
  - telecommunication
  - transparent surfaces

▶ Quantum Dot 제조회사 및 회사별 최근 과학기술 동향

1) Quantum Dot Corp. (www.qdots.com)

- Qdot Nanocrystals : 여러 가지 모양의 CdS (자외선영역), CdSe (가시광영역), CdTe (적외선영역) 코어를 나노 크기의 구조로 만들어 원하는 파장대역의 형광을 내는 양자점 제작.
- Qdot Bioconjugates : Qdot Nanocrystals 을 단백질 oligonucleotides 이나 여러 가지 분자 구조에 결합시킴으로써 해당 분야에 대한 응용이 가능한 양자점 제작.
- Qbead Microspheres : 각기 다른 emission maxima와 intensity를 가지고 있는 양자점의 emission band를 이용하여 spectral barcoding을 실현 가능한 나노 구조물 제작.
- Encoded Cells : 양자점 코어에 ZnS shell과 inner ligand coating을 통해 유독성을 없애 생체에 접목시킬 수 있는 양자점 복합구조 제작

2) Evident Technologies (www.evidenttech.com)

- Core Evidots : 양자점의 가장 기본이 된 상태를 연구하고자 할 때 파장이 490~620nm 영역의 CdSe 양자점, 또는 1000~2300nm 영역의 PbSe 양자점 제작.
- Core-Shell Evidots : 코팅 기술과 TOPO 계면 활성제를 이용하여 안정성과 밝기를 향상 시킬 수 있는 Core-Shell 구조의 CdSe/ZnS 또는 CdTe/CdS 양자점 제작..
- Evidot Composites : 박막, 구슬선, 섬유, 또는 마이크론 크기의 구조를 제조하고자할 때 레진과 메트릭스 물질을 이용하여 나노 구조와 마이크론 구조의 연계 가능한 나노구조 판매.

제 7 장 참고문헌

[Alivisatos(1998)] A.P. Alivisatos, A.L. Harris, N.J. Levinos, M.L. Steigerwald, L. Brus, J. Chem. Phys. **81**, 4001 (1998).

[Betzig(1991)] E. Betzig, J.K. Trautman, T.D. Harris, J.S. Weiner, and R.L. Kostelak, Science **251**, 1468 (1991).

[Bloembergen(1992)] N. Bloembergen, "Nonlinear Optics", Addison Wesley (1992).

[Boyd(1992)] R.W. Boyd, "Nonlinear Optics", Academic Press (1992).

[Feit(1988)] M.D. Feit, and J.A. Fleck, Jr., J. Opt. Soc. Am. B 5 633 (1988).

[Fibich(2000)] G. Fibich and A. L. Gaeta, Opt. Lett. **25**, 335 (2000).

[Halas(2002)] N. Halas, Optics and Photonics News, **13** (8), 26 (2002).

[Karrai(1995)] K. Karrai and R.D. Grober, Appl. Phys. Lett. **66**, 1842 (1995).

[Lee(1999)] M.B. Lee, M. Kourogi, T. Yatsui, K. Tsutsui, N. Atoda, and M. Ohtsu, Appl. Opt. **38**, 3566 (1999).

[Mostafavi(2000)] M. Mostafavi, Y.P. Liu, P. Pernot, J. Belloni, Radiation Physics and Chemistry **59**, 49 (2000).

[Mukamel(1995)] S. Mukamel, "Principles of Nonlinear Optical Spectroscopy", Oxford University Press (1995).

[Newell(1992)] A.C. Newell and J.V. Moloney, "Nonlinear Optics", Addison Wesley (1992).

[O'Connor(1984)] D.V. O'Connor and D. Phillips, "Time Correlated Single Photon Counting", Academic Press (1984).

[Pohl(1984)] D.W. Pohl, W. Denk & M. Lanz, Appl. Phys. Lett. **44**, 651(1984).

[Ruiter(1997)] A.G.T. Ruiter, J.A. Veerman, K.O. van der Werf, and N.F. van Hulst, Appl. Phys. Lett. **71**, 28 (1997).

[Seidel(1990)] H. Seidel, L. Csepregi, A. Heuberger and H. Baumgärtel, J. Electrochem. Soc. **137**, 3612 (1990).

[Shen(1991)] Y.R. Shen, "The Principles of Nonlinear Optics", John Wiley & Sons (1991).

[Song(2000)] K.B. Song, J. Lee, J.H. Kim, K. Cho, and S.K. Kim, Phys. Rev. Lett. 85, 3842 (2000).

[Yatsui(1997)] T. Yatsui, M. Kourogi, and M. Ohtsu, Appl. Phys. Lett. 71, 1756 (1997).

[Zenhausern(1995)] F. Zenhausern, Y. Martin, H.K. Wickramasinghe, Science 269, 1083 (1995).

[Zernike(1973)] F. Zernike and J.E. Midwinter, "Applied Nonlinear Optics", John Wiley & Sons (1973).

부록 : 학술지 게재 주요 연구논문

Optical parametric spectral broadening of picosecond laser pulses in β-barium borate

Seung Mook Lee and Bum Ku Rhee
Department of Physics, Sogang University, CPO Box 1142, Seoul 100-611, Korea

Moongoo Choi and Seung-Han Park
National Research Laboratory of Nonlinear Optics, College of Science, Yonsei University, Seoul 120-749, Korea

(Received 3 March 2003; accepted 11 July 2003)

We present that optical parametric luminescence generated near the degenerate point of a type I optical parametric tuning curve in β-BaB_2O_4 can be used as a spectrally broadened probe beam for a picosecond pump-probe spectroscopy. In particular, we show that it is possible to change the position of the central peak and spectral range in visible and infrared wavelengths by varying the incident angle of pump pulse with respect to the optical axis of barium borate crystal. The picosecond time-resolved diffuse-reflectance experiment is also performed in order to demonstrate usefulness of these spectrally broadened pulses as a probe source. © *2003 American Institute of Physics.* [DOI: 10.1063/1.1609054]

Pump-probe spectroscopic techniques have been recognized as an important tool to study ultrafast processes in biological systems and excited states of molecules, exciton dynamics in semiconductors, photoinduced dissociation processes of atomic systems in gas phase, etc.[1–4] In the pump-probe spectroscopy, in general, an intense pump beam is used to excite the materials and a spectrally broadened weak probe beam is employed to trace the absorption (or transmission) changes caused by the pump beam. When the changes in absorption spectra with and without pump beam are obtained at wide wavelength range, one can extract the valuable information on linear and nonlinear dynamics of the system. Therefore, much attention has been paid to produce spectrally broadened, easily tunable, and reduced-complexity probe beams.

For the femtosecond pump-probe spectroscopy, white-light continuum is widely used as a probe beam. The white light continuum ranging from ultraviolet to near infrared can be easily produced by focusing a powerful ultrashort laser pulses into a transparent medium, such as glasses, alkali halides, transparent crystals, and even gases.[5–13] Folk *et al.* obtained white-light continua ranging from 0.19 to 1.6 μm by illuminating focused femtosecond dye laser pulses into a thin jet of ethylene glycol.[14] Corkum *et al.* were the first to report the continuum generation from high-pressure gases.[15] More recently, Nishioka *et al.* and Kasparian *et al.* extended the spectral range of the white-light continuum into the vacuum ultraviolet and midinfrared regions by using terrawatt Ti:sapphire laser pulses, respectively.[16,17] However, in the condensed media, the structural damage is usually accompanied mainly due to self-focusing and in contrast damage in liquids is self-healing.

For the picosecond regime, water has been regarded as an ideal source for generating the broadband probe pulses.[18,19] It has been reported that the four-wave parametric interaction and the stimulated Raman effects in water are the dominant mechanisms for spectral superbroadening. It has been observed that the self-broadening in D_2O is more pronounced than in H_2O. However, there is a fundamental limit to utilize D_2O as a source to obtain the probe beam because of the high-intensity spikes existed in the superbroadening and the required long interaction length, which make the spectroscopic system quite bulky and complicated. Up to now there is no efficient, compact, and convenient way to obtain spectrally broadened probe beam for the pump-probe spectroscopy in picosecond time domain.

In this letter, we present a method of generating broadband probe beam from a barium borate (BBO) crystal with picosecond Nd:yttritium–aluminum–garnet (YAG) laser pulses. We show that picosecond broadband probe pulses can be produced efficiently in visible and infrared wavelengths by varying incident angle of exciting laser pulses on BBO crystal near operating angle of optical parametric generation with relatively low intensities. A strong dependence of the broadband spectral distribution on incident angle to the BBO crystal is also observed. Furthermore, it is found that the intensity of the obtained broadband probe can be almost two orders of magnitude larger than that of supercontinuum generation in D_2O. Producing the broadband light source in picosecond domain is based on the fact that the angular dependence of frequency bandwidth is large near the degenerate point of optical parametric tuning curve.

Our technique to produce a broadband probe beam is schematically described in Fig. 1. The third and fourth harmonics (355 and 266 nm) of a mode-locked Nd:YAG laser were used to pump β-BBO crystal to make picosecond pulse trains of broadband optical parametric luminescence (OPL)

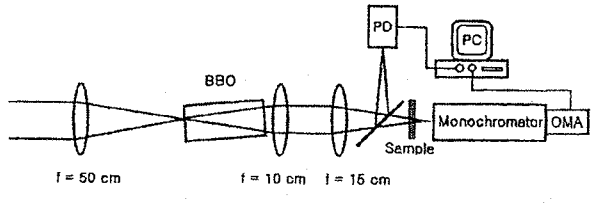

FIG. 1. Experimental setup.

0003-6951/2003/83(9)/1722/3/$20.00

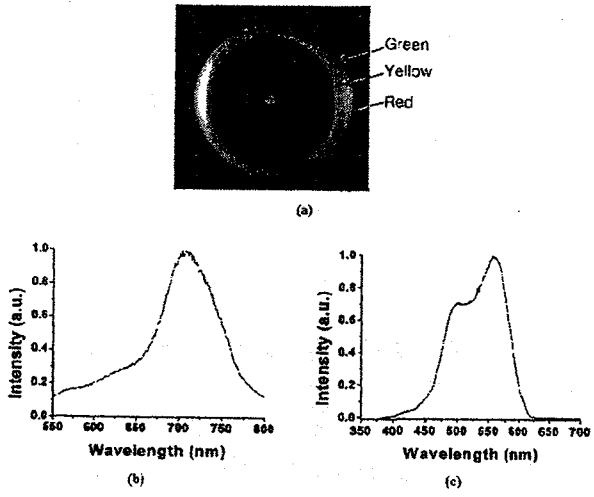

FIG. 2. (a) Spatial pattern of OPL, (b) spectrum of OPL for 355 nm pump, and (c) spectrum of OPL for 266 nm pump.

with the type I phase matching, resulting in extraordinary polarization of pump beam. The pulse duration and repetition rate of the mode-locked Nd:YAG laser were ~40 ps and 10 Hz, respectively. The pump beam of 2.5 mm radius at 355 nm was focused onto the crystal with a convex quartz lens of focal length 50 cm. The focal spot was located at the entrance surface of β-BBO in order to utilize the divergence of the pump beam. The size of β-BBO cut at $\varphi=0°$ and $\theta=22.8°$ (internal angle of crystal) is 5 mm (H) $\times$5 mm (W)$\times$10 mm (L). As a result of optical parametric generation, bright multicolored parametric luminescence of nearly circular shape was observed at a screen ~5 cm away from the exit surface of β-BBO. The color and radius of the ring were strongly dependent upon the angle between the propagation direction and the direction normal to the entrance surface of β-BBO. The total integrated energy of multicolored OPL was measured to be ~200 μJ with a pump pulse energy of ~2 mJ, which is almost two orders of magnitude higher than that from a superbroadened picosecond pulses in a 50:50 mixture of H_2O and D_2O pumped by a focused Nd:YAG laser beam with energy of 7 mJ, which is close to the damage threshold of quartz cell.

A typical colored ring obtained with $\theta=35°$ is shown in Fig. 2(a). This colored ring was collimated by using a lens of focal length 10 cm, focused by a convex lens of focal length 15 cm, and reduced to a focal spot of ~0.5 mm in diameter, as is depicted in Fig. 1. A beam splitter (quartz plate) was placed between the focusing lens and the focal spot. One part of the splitting beams was used as a reference in order to normalize the intensity fluctuation of OPL. The reference and transmitted beams were picked up by an optical fiber and measured using a spectrometer equipped with an optical multichannel analyzer. Figure 2(b) shows an OPL spectrum without sample obtained by taking an average of 30 spectra under the condition of $\theta=35°$. The wavelength of central peak is located at the degenerate point of the tuning curve of type I phase-matched β-BBO optical parametric generation, as expected. If we divided one spectrum by the other without the sample, we could obtain the straight line within an accuracy of 0.5% in the spectral range between 600 and 780 nm,

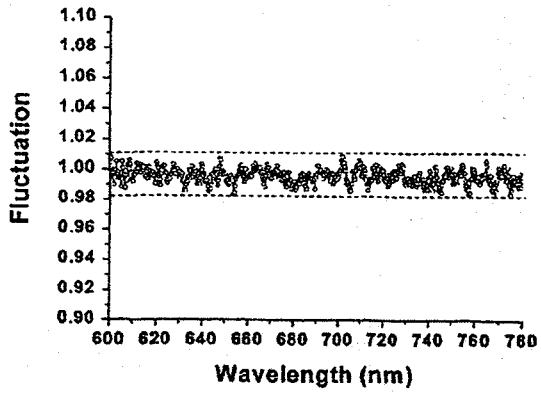

FIG. 3. Intensity fluctuation of normalized optical parametric luminescence.

as displayed in Fig. 3. When we made the broadband OPL by pumping BBO crystal cut at $\theta=44.7°$ and $\varphi=0°$ with the second harmonics of 532 nm radiation from the picosecond mode-locked laser, the similar multicolored ring with spectral peak located at 532 nm. However, we observed quite different spectral shape, as shown in Fig. 2(c), indicating clearly that the spectral range between 460 and 600 nm could be used as a broadband probe with an accuracy of 0.7%. The single pulse energy of 266 nm pump was ~1 mJ. If longer than 14 mm BBO crystal and 266 nm pump with higher energy is used, the limit of spectral bandwidth can be extended to shorter than 400 nm.

In order to demonstrate the potentialities of these spectrally broadened pulses as a probe beam, we performed a picosecond time-resolved diffuse-reflectance measurement for the anthracene-methylviologen charge-transfer (AMCT) complex encapsulated within zeolite-Y by using OPL pumped at 355 nm.[20,21] Both the second- and third-harmonic light pulses were extracted from a mode-locked Nd:YAG laser. The beam size of second-harmonic (532 nm) and third-harmonic (355 nm) wave were ~6 and ~5 mm in diameter, respectively. The second-harmonic beam with single pulse energy of ~4 mJ traversed a variable (up to 4 ns) delay stage before being directed onto the sample cuvette, which contained powder of AMCT complex to excite the charge-transfer complexes. The third-harmonic beam with energy of ~2 mJ was focused onto BBO to produce broadband probe pulses, whose spectra were displayed in Fig. 2(b). The broadband probe beam was focused down to the size of 0.5 mm in order to make the good spatial overlap between pump and probe beams. The intensity distribution of the focused probe beam near focal point is expected to be almost uniform because of its incoherency, unlike the far-field ring-like OPL output. The temporal overlap between the pump and probe beams was carefully checked by measuring the intensity of sum-frequency wave as a function of the temporal delay. The sum-frequency generation was achieved by using the vector phase matching, directing the pump and probe beam with the internal angle of 47.2° and 37.0° to the optical axis of BBO crystal, respectively. The sum-frequency wave of the central wavelength at 304 nm was emerging at the internal angle of 41.7° with respect to the optical axis after nonlinear interaction in BBO. The intensity of sum-frequency wave was strong enough to detect even with photodiode after filtering

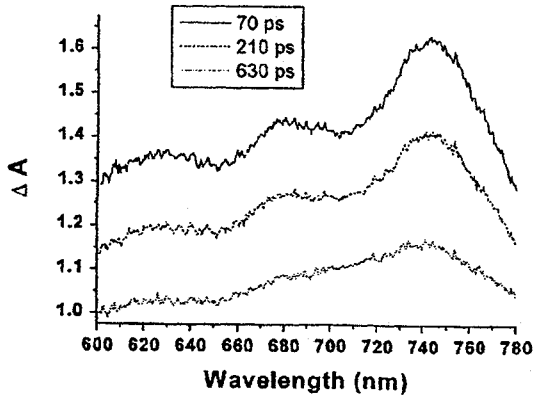

FIG. 4. Measured changes of absorption spectra with various temporal delays of 70, 210, and 630 ps.

302 nm with 25 cm monochromator. For the diffuse-reflectance measurements, an appropriate cutoff filter was positioned in front of a fiber optics to eliminate scattered light from the excited pulse of 532 nm.

The measured changes of absorption spectra (ΔA) with the various temporal delay (70, 210, and 630 ps) were shown in Fig. 4. It is known that two maxima around 620 and 730 nm in Fig. 4 are originated from the absorption due to reduced methylviologen (MV+) and oxidized anthracene (Ant+).[22] Note that each time-resolved transient diffuse-reflection spectrum was obtained from an average of 30 laser pulses, indicating a very good signal to noise ratio. These results are identical to the previously reported spectra, in which a 50:50 mixture of D_2O and H_2O was used to produce spectral superbroadening and over 100 spectra were averaged.[22]

In conclusion, we have found that the broadband OPL generated from the solid-state β-BBO is very efficient, compact, and convenient way to produce a spectrally flat and extremely stable probe beam, compared with the superbroadened radiation of D_2O (or H_2O), in picosecond time domain. Without any amplification and additive elements, the spectral wavelengths in the range from ~460 to ~800 nm were easily obtained. The spectral width and central peak of the OPL are readily adjustable since the color and radius of OPL ring depend on the angle between the propagation direction and the direction normal to the entrance surface. Quantitative understanding the nonlinear processes involved in the angular dependence of OPL is under investigation. We also demonstrate that the broadband OPL can be successfully utilized as a probe beam for the picosecond time-resolved diffuse-reflectance measurement. We hope that the spectral versatility, tunability, and reduced-complexity of the high-intensity broadband OPL will open new perspectives on the picosecond pump-probe nonlinear spectroscopy.

This research was supported by Korea Research Foundation Grant No. (KRF-2000-015-DP0135) for the authors at Sogang University, and the Ministry of Science and Technology through the National Research Laboratory Program (Contract No. M1-0203-00-00832) for the authors at Yonsei University.

[1] T. Baumert, M. Grosser, R. Thalweiser, and G. Gerber, Phys. Rev. Lett. **67**, 3753 (1991).
[2] Dana M. Calistru, S. G. Demos, and R. R. Alfano, Phys. Rev. Lett. **78**, 374 (1997).
[3] P. C. Becker, D. Lee, A. M. Johnson, A. G. Prosser, R. D. Feldman, R. F. Austin, and R. E. Behringer, Phys. Rev. Lett. **68**, 1876 (1992).
[4] L. Nugent-Glandorf, M. Scheer, D. A. Samuels, A. M. Mulhisen, E. R. Grant, X. Yang, V. M. Bierbaum, and S. R. Leone, Phys. Rev. Lett. **87**, 193001 (2001).
[5] A. Brodeur and S. L. Chin, Phys. Rev. Lett. **80**, 4406 (1998).
[6] K. Igarashi, S. Saito, M. Kishi, and M. Tsuchiya, IEEE J. Sel. Top. Quantum Electron. **8**, 521 (2002).
[7] G. Y. Yang and Y. R. Shen, Opt. Lett. **9**, 510 (1984).
[8] F. A. Ilkov, L. Sh. Ilkova, and S. L. Chin, Opt. Lett. **18**, 681 (1993).
[9] G. S. He, G. C. Xu, Y. Cui, and P. N. Prasad, Appl. Opt. **32**, 4507 (1993).
[10] A. Brodeur, F. A. Ilkov, and S. L. Chin, Opt. Commun. **129**, 193 (1996).
[11] K. R. Wilson and V. V. Yakovlev, J. Opt. Soc. Am. B **14**, 444 (1997).
[12] K. Midorikawa, H. Kawano, A. Suda, C. Nagura, and M. Obara, Appl. Phys. Lett. **80**, 923 (2002).
[13] J.-P. Likforman, A. Alexandrou, and M. Joffre, Appl. Phys. Lett. **73**, 2257 (1998).
[14] R. L. Fork, C. V. Shank, C. Hirlimann, R. Yen, and W. J. Tomlinson, Opt. Lett. **8**, 1 (1983).
[15] P. B. Corkum, C. Rolland, and T. Srinivasan-Rao, Phys. Rev. Lett. **57**, 2268 (1986).
[16] H. Nishioka, W. Odajima, K. Ueda, and H. Takuma, Opt. Lett. **20**, 2505 (1995).
[17] J. Kasparian, R. Sauerbrey, D. Mondelain, S. Niedermeier, J. Yu, J.-P. Wolf, Y.-B. Andre, M. Franco, B. Prade, S. Tzortzakis, A. Mysyrowicz, M. Rodriguez, H. Willw, and L. Woste, Opt. Lett. **25**, 1397 (2000).
[18] W. L. Smith, P. Liu, and N. Bloembergen, Phys. Rev. A **15**, 2396 (1977).
[19] A. Penzkofer, A. Beidoum, and H.-J. Lehmeier, Opt. Quantum Electron. **25**, 317 (1993).
[20] G. P. Kelly, P. A. Leicester, F. Wilkinson, D. R. Worrall, L. F. V. Ferreira, R. Chittock, Toner, and W. Toner, Spectrochim. Acta, Part A **46**, 975 (1990).
[21] N. Ikeda, K. Imagi, H. Masuhara, N. Nakashima, and K. Yoshihara, Chem. Phys. Lett. **140**, 281 (1987).
[22] K. B. Yoon, S. M. Hubig, and J. K. Kochi, J. Phys. Chem. **98**, 3865 (1994).

Phase-shifting lateral shearing interferometer with two pairs of wedge plates

Hyun-Ho Lee, Jang-Hoon You, and Seung-Han Park

National Research Laboratory of Nonlinear Optics, College of Science, Yonsei University, Seoul 120-749, Korea

Received April 15, 2003

We present a compact and robust phase-shifting lateral shearing interferometer that produces shearing fringes in orthogonal directions without any mechanical rotation or precise alignment. It consists of two pairs of wedge plates, a beam splitter, and a single CCD camera. Both phase-shifting and tilt for lateral shearing are achieved with two pairs of wedge plates, which can reduce systematic errors caused by external vibration and atmospheric disturbance. © 2003 Optical Society of America

OCIS codes: 120.3180, 120.5050, 220.4840.

The lateral shearing interferometer (LSI) has been commonly used as a tool to test optical elements, lasers, surfaces, lenses, optical pickup systems, and near-field optical phases. One of its main advantages is that it eliminates the necessity for a separate ideal reference wave front because the original wave front interferes with a sheared copy of that wave front. This advantage greatly reduces alignment cost and measurement time. Lateral shearing can be induced by parallel plates,[1,2] gratings,[3–5] birefringence,[6,7] prisms,[8,9] Mach–Zehnder configurations,[10,11] and Michelson arrangements.[12,13]

In recent years, various types of LSI have been developed for particular use in inspection of aspheric lenses and surfaces.[1–14] Although numerous techniques have been developed for lateral shearing, only a few methods, such as shifting of a plane mirror, use of a double grating stepper,[14] and use of a liquid-crystal retarder,[15] have been reported for phase shifting. In general, for phase shifting, an expensive piezoelectric transducer with a driver and, in the case of a liquid-crystal device, with precise coatings to control the reflection at the glass–liquid interfaces are required. In addition, it is necessary to move a CCD camera or to install two CCD cameras to capture two interferograms in orthogonal directions to reconstruct the original wave front from the measured phases. Good mechanical stability against vibration as well as against rotation is also needed to maintain the constant incident angle of the light toward the shear plate while measuring the interferograms.

In this Letter we present a compact and robust phase-shifting LSI that uses two pairs of wedge plates, a beam splitter, and a single CCD camera to overcome these difficulties. In particular, the two pairs of wedge plates are employed to induce a tilt in the wave front for lateral shearing and to produce orthogonal phase-shifted shear fringes. In our newly configured LSI setup, no mechanical movement to change the shearing direction or coordinate transformation to make the fringes of equal size is required.

A schematic diagram of our interferometer is displayed in Fig. 1. The two pairs of wedge plates (WPSx and WPSy) are installed, with shear and tilt kept parallel, in two orthogonal shear directions. The x- and y-shear interferograms are selectively grabbed by a CCD camera and two shutters. As mentioned above, in other interferometers[5,14] the optical components should be rotated to produce interferograms in different shear directions. Because rotation error affects the coefficients of the noncircularly symmetric Zernike terms, accurate rotation is required for reconstruction of the wave front. In our setup, however, the interferometer can measure without the need for any optical elements to be moved.

Lateral shear and phase shifting are achieved with the wedge-plate set illustrated in Fig. 2 in detail. A tilt angle of θ_1 between front and rear surfaces of the wedge plates is utilized to shear the original beam. The outer (right-hand) surface of wedge plate WP1 is normal to the optical axis, and the outer (left-hand) surface of WP2 is tilted to the optical axis by θ_1. The laterally sheared beams reflected by these two surfaces are imaged onto a CCD array. The wedge plates are attached by immersion in liquid with the same refractive index as the wedge plates. The tilt angle (θ_1), which is the cumulative angle of two wedge plates, can be controlled by rotation of one of the wedge plates.

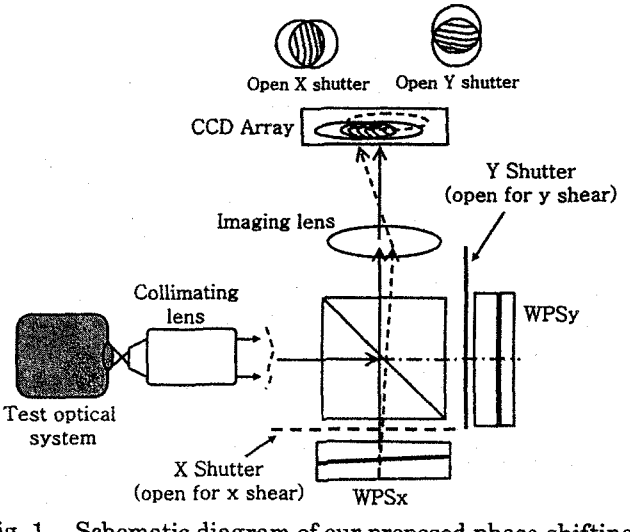

Fig. 1. Schematic diagram of our proposed phase-shifting LSI with two pairs of wedge plates, a beam splitter, and a single CCD camera.

0146-9592/03/222243-03$15.00/0

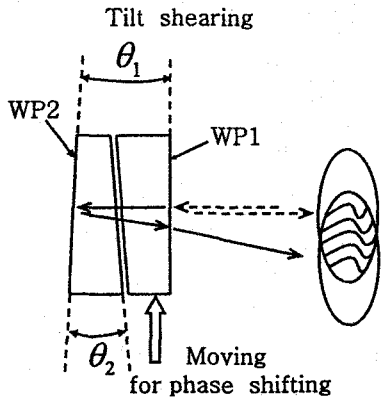

Fig. 2. Pair of wedge plates for phase shifting and tilt shearing.

The amount of tilt can easily be estimated from the measured interferogram.

The pair of wedge plates is utilized as a physically robust phase shifter as well as an accurate tilt inducer. We produce the phase shift by sliding one of the wedge plates in contact along the wedge direction, resulting in an increase or a decrease of total thickness of WP1 and WP2 with wedge angle θ_2, as shown in Fig. 2. We adopt an inexpensive translator with low resolution instead of using an expensive piezoelectric translator with nanometer precision as is often employed for the conventional LSI. The interferograms generated by a pair of wedge plates are quite insensitive to mechanical vibrations because two surfaces that reflect the incident beams are physically in contact. When two plates of ~0.5° wedge (θ_2) are used to make a phase shifter, the wedge plate should be translated near 17 μm to yield a quarter-wavelength phase shift at $\lambda = 633$ nm. Note that longer phase shifts require smaller wedge angles θ_2.

The measured x- and y-shear interferograms are shown in Figs. 3(a) and 3(b), respectively. One of the two shutters is selectively opened, and then the corresponding shear interferogram is captured. When both shutters are open simultaneously, however, an interference fringe with low frequency can be obtained, as displayed in Fig. 3(c), which indicates that the interference pattern is produced by the on-axis normal surfaces of two wedge-plate sets. Using these low-frequency fringes, which are quite useful for making precise on-axis alignments, permits the two shearing interferograms of the same coordinates and the same scales to be captured by a single CCD array. Therefore no additional coordinate transform is required, and relatively small errors in aperture selection are introduced. As shown in Figs. 3(a) and 3(b), however, tilt (θ_1) affects the defocus term in the Zernike coefficients of the original wave front even if both tilt and shear directions are parallel in each interferogram and the shear ratios are equal. Because the amounts of tilt cannot be completely equal and their directions cannot be perfectly orthogonal for the two pairs of wedge plates, systematic errors may also have an influence on the astigmatism.

To find the original wave front from the two shear wave fronts we use the reconstruction algorithm proposed by Rimmer and Wyant.[4] The relationship between the sheared wave front and the original wave front $W(x, y)$ is assumed to be[16]

$$\Delta W_x = W(x + a, y) - W(x, y) + X_x x + \Delta Y_x y, \quad (1)$$

$$\Delta W_y = W(x, y + b) - W(x, y) + Y_y y + \Delta X_y x, \quad (2)$$

where ΔW_x, ΔW_y, a, and b are the phases and the shear amounts in the x and y shear interferograms, X_x and Y_y are the tilts in shear directions generated by tilt angle (θ_1) of WPSx and WPSy, and ΔX_y and ΔY_x are the tilts in the directions orthogonal to the shear directions produced mainly by the misalignment of two wedge-plate sets, respectively. Systematic errors (X_x, Y_y, ΔX_y, and ΔY_x) appear in the defocus and astigmatism terms of the wave front reconstructed by the algorithm. Therefore they are compensated for by the Zernike coefficients obtained by preliminary measurement of the reference plane wave front. After the correction, high resolution of the root-mean-square wave front, less than $\lambda/1000$, is obtained. It should be emphasized that all the phase-shifted shear fringes in orthogonal directions were measured on an ordinary tabletop without stabilization or damping facilities.

In conclusion, we have proposed a new type of phase-shifting lateral shearing interferometer in which two pairs of wedge plates are utilized as phase shifters and a lateral-shear inducer. The cumulative angle of the wedge plates and sliding a wedge plate provides the lateral shear and the phase shift necessary for evaluating the beam's wave front. Our configuration does not require any rotation of optical components to change the shearing direction, thereby reducing systematic errors and errors that are due

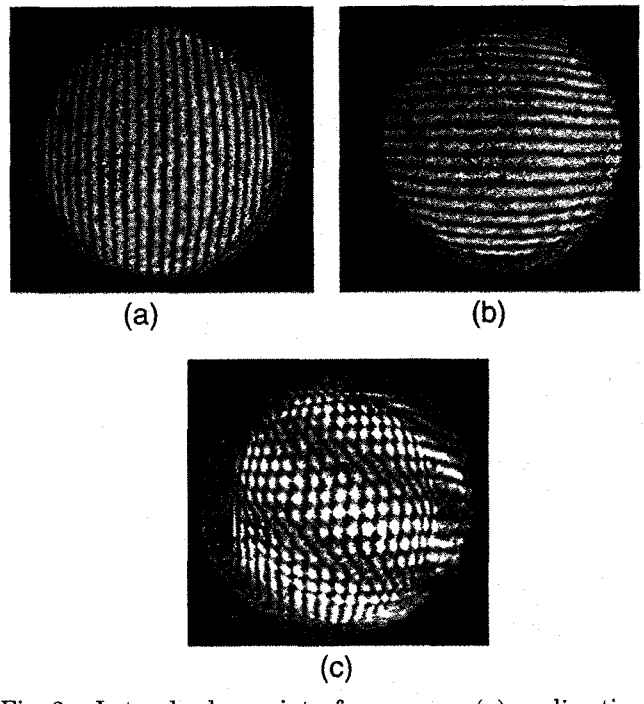

Fig. 3. Lateral shear interferograms: (a) x direction, (b) y direction, (c) both shutters open.

to vibration. Therefore we expect that the proposed phase-shifting LSI will be practically applied for evaluating various optical components and systems.

This research was supported by the Ministry of Science and Technology of Korea through the National Research Laboratory Program (contract M1-0203-00-00832). S. H. Park's e-mail address is shpark@phya.yonsei.ac.kr.

References

1. M. V. R. K. Murty, Appl. Opt. **3,** 531 (1964).
2. P. Hariharan, Appl. Opt. **14,** 1056 (1975).
3. V. Ronchi, Appl. Opt. **3,** 437 (1964).
4. M. P. Rimmer and J. C. Wyant, Appl. Opt. **14,** 142 (1975).
5. H. Schreiber and J. Schwider, Appl. Opt. **36,** 22 (1997).
6. A. K. Saxena, Appl. Opt. **18,** 16 (1979).
7. J. W. Hardy and A. J. MacGovern, Proc. SPIE **816,** 180 (1987).
8. J. B. Saunders, Appl. Opt. **6,** 1581 (1967).
9. W. J. Cho and S. W. Kim, Opt. Eng. **36,** 3 (1997).
10. M. V. Mantravadi, in *Optical Shop Testing,* 2nd ed., D. Malacara, ed. (Wiley, New York, 1992), Chap. 4.
11. G. Paez, M. Strojnik, and G. G. Torales, Appl. Opt. **39,** 28 (2000).
12. M. V. R. K. Murty, Appl. Opt. **9,** 5 (1970).
13. T. Siebert and B. Schmitz, Proc. SPIE **3637,** 225 (1999).
14. G. W. R. Leibbrandt, G. Harbers, and P. J. Kunst, Appl. Opt. **35,** 6151 (1996).
15. D. W. Griffin, Opt. Lett. **26,** 140 (2001).
16. W. Shen, M.-W. Chang, and D.-S. Wan, Opt. Eng. **36,** 905 (1997).

Journal of the Korean Chemical Society
2004, *Vol. 48, No. 3*
Printed in the Republic of Korea

감마선을 이용한 수용액상의 CdS 양자점 제조 및 광학적 특성

정은희 · 이재훈 · 임상엽 · 이창열† · 최영수† · 최중길† · 박승한*
연세대학교 이과대학 물리학과
†연세대학교 이과대학 화학과
(2004. 3. 15 접수)

Fabrication and Optical Characteristics of CdS Quantum Dot Structures in Aqueous Solution Using a Gamma-ray Irradiation Technique

Eun-Hee Jeang, Jae-Hoon Lee, Sang-Youp Yim, Chang-Youl Lee†, Young-Soo Choi†, Joong-Gill Choi†, and Seung-Han Park*
Department of Physics, Yonsei University, Seoul 120-749, Korea
†Department of Chemistry, Yonsei University, Seoul 120-749, Korea
(Received March 15, 2004)

요 약. 감마선을 이용하여 수용액상에서 안정화 된 CdS 반도체 양자점을 제조하고, 제조된 양자점의 광학적 흡수스펙트럼을 분석하였다. CdS 양자점 제조시 카드뮴을 제공하는 물질로는 cadmium sulfate를 사용하였고, 황을 제공하는 물질로는 2-mercaptoethanol을 사용하였으며, 매개체로는 감마선이 조사된 물에 존재하는 환원제 e_{aq}^-을 이용하였다. 감마선 조사 전과 후에 제조된 CdS 양자점의 흡수스펙트럼을 비교한 결과, 감마선 조사 후에는 300 nm~400 nm 사이에서 CdS 양자점 형성에 의한 엑시톤 흡수 봉우리가 명확히 관측됨을 확인할 수 있었다. 또한 감마선의 조사 시간을 5분, 10분, 15분으로 증가시켜 감마선의 양을 다르게 조사시킨 결과 엑시톤 흡수 파장이 338 nm, 347 nm, 367 nm로 장파장 쪽으로 이동함을 확인함으로써, 감마선의 조사량을 조절하면 CdS 양자점의 크기를 변화시킬 수 있음을 알 수 있었다.

주제어: CdS 양자점, 감마선, 수용액, 엑시톤흡수봉우리

ABSTRACT. CdS semiconductor quantum dot (QD) structures in aqueous solution are fabricated by using a gamma-ray irradiation technique and their optical absorption spectra are investigated. Cadmium sulfate solution, 2-mercaptoethanol solution, and reducing agent e_{aq}^- are employed to produce CdS molecules, leading to CdS quantum dots. The measured linear absorption spectra before and after γ-ray irradiation clearly show exciton peaks between 300 nm and 400 nm, which indicate the formation of CdS QD's. It is also observed that the exciton peaks are red-shifted with increasing the γ-ray irradiation time from 5 min to 15 min. Therefore, it is concluded that the mean QD sizes can be systematically controlled with the dosage of the γ-ray irradiation.

Keywords: CdS Quantum Dot, Gamma-ray Irradiation, Aqueous Solution, Exciton Peaks

서 론

반도체 양자점은 그 크기에 따라 광학적, 물리적 특성이 변하는 특이한 성질이 있어, 그동안 많은 연구 그룹들이 양자점 제조방법 및 그 응용에 관한 연구를 수행하여 왔다.[1,2] 이러한 양자점 제조방법 중에서 가장 오래되고 널리 사용된 제조방법으로 II-VI족 반도체 화합물인 양자점을 유리모재에 제조하는 방법을 들 수 있는데, 이 방법은 안정적인 양자점을 제조하기가 어려운 단점이 있었다.[3] 이와 같은 단점을 보완하여 안정적인

양자점을 제조하기 위해서는 원자들 간의 반응결합이 빨리 일어나게 해야 하고 동시에 크기성장은 천천히 일어나게 해야 하므로 유리모재 대신 용액 상에서 존재하는 양자점을 제조하는 방법이 여러 화학자들에 의해 개발되었다.[4-6]

용액 상에서 양자점을 제조할 경우 모체인 용액은 양자점을 안정화시키는 역할을 하게 되며, 양자점의 구조는 화학적인 반응에 의해 화학적인 평행상태에서 만들어지게 된다. 특히, 양자점간의 뭉침을 방지하고 용해도를 증가시키기 위해서 캡핑 리간드(capping ligand)를 이용하며, 양자점의 크기를 효과적으로 제어하기 위해서 온도 조절을 이용한다. 그러나 이러한 온도조절방법 또한 양자점 크기 변화를 부분적으로 확인할 수밖에 없는 한계가 있다.

따라서 최근 Treguer *et al.*[7], Belloni *et al.*[8], Mostafavi et al.[9]와 같은 학자들을 중심으로 감마선을 이용하여 상온의 용액 상에서 양자점 구조를 제조하고자 하는 연구가 활발히 개발되고 있다. 감마선을 조사시켜 수용액상에서 양자점을 제조하는 방법은 양자점이 원자크기의 상태에서 더 큰 크기로 진행하는 과정을 단계별로 관측할 수 있어 양자점의 크기를 정교하게 조절할 수 있다는 장점이 있으며,[9] 모든 제조과정이 상온에서 수용액상에서 이루어지므로 생물학적인 연구에 쉽게 활용될 수 있다는 장점이 있어 큰 주목을 받고 있다.

본 연구에서는 이와 같은 감마선을 이용한 양자점 제조방법을 이용하여 수용액상에서 cadmium sulfate와 2-mercaptoethanol을 혼합하고 감마선으로 이온화시킴으로써 CdS 양자점을 제조하였다. 특히, 감마선의 양을 변화시켜 가면서 양자점을 제조하고 그 광학적 흡수스펙트럼을 측정하여 분석함으로써 감마선 조사량에 따라 양자점의 크기를 체계적으로 조절할 수 있음을 확인하였다.

실 험

II-VI족 반도체 화합물인 CdS 양자점을 수용액상의 콜로이드 상태로 제조하기 위하여, 본 연구에서 사용한 제조방법의 특징은 모체로 사용한 수용액에 감마선을 조사시킴으로써 수많은 이온상태의 물질들이 존재하도록 하고 이들 간에 화학적인 반응이 이루어지도록 한다는 점이다. 감마선 조사로 생성된 환원제 e_{aq}^-가 카드뮴과 황을 결합시켜주는 매개체 역할을 하므로 CdS 양자점이 생성될 수 있다. 실험에 사용한 시약은 Aldrich사의 cadmium sulfate($CdSO_4$, M.W.=78.1), 2-mercaptoethanol ($HOCH_2CH_2SH$, M.W.=208.5), sodium phosphate (Na_3PO_4)이었다. 이 때 cadmium sulfate는 카드뮴의 모체용액이 되고, 2-mercaptoethanol는 황의 모체용액이 된다.

실험을 시작하기 전 불순물을 제거하기 위하여 HNO_3:HCl=1:2로 섞은 왕수로 용기들을 세척하였다. 이는 감마선 조사방법이 결정핵 생성반응을 이용한 방법이므로 미세한 불순물에도 민감하게 반응하기 때문이다. 왕수로 세척을 마친 후, 왕수를 완전히 제거하기 위하여 용기들을 다시 증류수로 깨끗이 세척하였다. 모든 제조과정은 산화를 억제하기 위해 아르곤 기체 내에서 수행되었다. 카드뮴의 모체용액은 10^{-3} M의 농도의 $CdSO_4$를 사용하고 약 10분정도 stirring 시킨 뒤, pH를 측정한 결과 4.6으로 유지되어 산성임을 확인하였다. 황의 모체용액을 제조하기 위해 우선 완충용액(buffer solution)인 sodium phosphate를 증류수에 용해시켜 몰농도가 2.0×10^{-2} M 되도록 만들었다. 이 완충용액은 마지막 작업에서의 CdS 용액의 pH가 7.5가 되도록 하여 반응을 최적화시킴은 물론, CdS를 생성할 때 필요한 H^+ 이온을 계속 공급해준다. 이렇게 제조된 완충용액은 pH가 11.3으로서 강한 염기성을 가지고 있었다. 만들어진 완충용액에 2-mercaptoethanol($HOCH_2CH_2SH$)을 0.1 M이 되도록 넣어 황의 모체용액을 제조하였다. 이렇게 만든 2-mercaptoethanol은 산성이므로 완충용액을 섞어 pH가 9.0 이 되게 하였다. CdS 양자점 제조 시 필요한 시약과 각각의 몰농도와 pH는 *Table* 1에 요약하였다.

이렇게 만들어진 카드뮴의 모체용액과 황의 모체용액을 적당한 부피로 혼합하여 각각의 몰농도를 조절하였다. 이 때 각각의 몰농도는 $CdSO_4$가 2.5×10^{-4} M, $HOCH_2CH_2SH$가 7.5×10^{-2} M 되도록 하여 $CdSO_4$와 $HOCH_2CH_2SH$의 몰농도의 비율을 1:300으로 유지하게

Table 1. CdS 양자점 제조 시 사용된 시약, 몰농도 및 pH 조건

시 약	몰농도	pH
Cadmium sulfate	10^{-3} M	4.6
Sodium phosphate	2×10^{-2} M	11.25
2-mercaptoethanol	2.5×10^{-2} M 5.0×10^{-2} M 7.5×10^{-2} M	9

하였다. 이때 pH는 카드뮴의 산성과 황의 염기가 섞여 7.5가 되었다. 이 작업에서 pH의 역할은 반응을 최적화할 뿐만 아니라 안정화시키는 역할을 하므로 매우 중요하다. 만약 pH가 7.5로 유지가 되지 않으면 안정화된 화학반응이 잘 일어나지 않게 된다.[9] 몰농도 비율이 1:300으로 한 이유는 Cd^{2+} 이온이 e_{aq}^-와 반응하는 속도가 $HOCH_2CH_2SH$가 e_{aq}^-와 반응하는 속도보다 훨씬 빠르기 때문이다. 따라서 Cd^{2+} 이온과 SH^- 이온이 반응할 확률이 많아지도록 SH^-를 더 많이 첨가하였다. 이 때 Cd^{2+} 이온이 e_{aq}^-와 반응하는 속도는 5.5×10^{10} $M^{-1}s^{-1}$ 이고 $HOCH_2CH_2SH$가 e_{aq}^-와 반응하는 속도는 1.2×10^{10} $M^{-1}s^{-1}$ 이므로 Cd^{2+} 이온의 반응속도가 $HOCH_2CH_2SH$ 경우보다 약 4.5배 정도 빠르다고 알려져 있다.[10] 이와 같이 몰농도의 비로 섞여진 CdS 용액은 공기로부터 밀폐되어야 하므로 질소로 탈기체화(degassing) 시킨 후 CdS 용액이 화학반응을 통해 CdS 양자점이 생성될 수 있도록 ^{60}Co 7000Ci를 이용하여 감마선을 조사시켰다. 감마선을 조사시킬 때 CdS 양자점의 크기를 조절하기 위하여 5분, 10분, 15분씩 조사시간을 변화시켜 가면서 용액에 감마선을 조사하였다.

감마선에 의해 조사된 물은 다음 식 (1)과 같이 이온화된다.[9,11]

$$H_2O \rightarrow e_{aq}^-, H^+, H^\bullet, OH^\bullet, H_2, H_2O_2 \qquad (1)$$

이 때 라디칼 종류인 $H^\bullet$와 $OH^\bullet$는 식 (2)와 같이 2-mercaptoethanol과 결합하여 아래와 같이 제2황화물로 재결합하게 된다.

$$OH^\bullet(H^\bullet) + HOCH_2CH_2SH \rightarrow HOCH_2CH_2S^\bullet + H_2O(H_2) \qquad (2)$$

위의 (2)반응에서 생성된 라디칼들은 다시 아래의 (3) 반응으로 결합하게 된다.

$$2HOCH_2CH_2S^\bullet \rightarrow (HOCH_2CH_2S)_2 \qquad (3)$$

또한, 감마선에 의해 이온화된 물에 생성된 수많은 환원제 e_{aq}^-는 $HOCH_2CH_2SH$와 반응하여 SH^- 이온을 생성한다.

$$HOCH_2CH_2SH + e_{aq}^- \rightarrow CH_2CH_2OH + SH^- \qquad (4)$$

(4)반응의 속도는 $K_4 = 1.2\times10^{10}M^{-1}s^{-1}$이고, 아래와 같은 환원제 e_{aq}^-와 카드뮴이온과의 (5)반응은 반응속도가 $K_5 = 5.5\times10^{10}M^{-1}s^{-1}$로 알려져 있으며 아래와 같은 반응에 의하여 카드뮴 이온에 전자를 공급하게 된다.[10]

$$Cd^{2+} + e_{aq}^- \rightarrow Cd^+ \qquad (5)$$

CdS 용액을 제조하는 과정에서 설명하였듯이, $HOCH_2$-CH_2SH의 농도가 $CdSO_4$의 농도의 300배정도가 되므로 (5)반응은 (4)반응에 비해 무시될 수 있다. 비록 (5)에 의해서 Cd^{2+}가 생성된다하더라도 그것의 redox potential이 매우 낮으므로 Cd^+는 SH^- 이온 생성에 간접적으로 영향을 미치게 된다. 즉 환원제 e_{aq}^-는 (5)반응보다 (4)반응에 기여하므로 e_{aq}^-와 반응을 하지 않은 카드뮴이온들은 (4)반응으로 생성된 SH^-이온과 아래와 같이 반응하여 CdS와 H^+ 이온을 만들게 된다.

$$Cd^{2+} + SH^- \rightarrow CdS + H^+ \qquad (6)$$

따라서 수용액상에서 분자로 존재하던 카드뮴과 황은 CdS로 만들어 지게 된다[9]. 또한 감마선의 조사량이 모든 Cd^{2+} 이온들이 CdS로 만들어 질만큼 충분하면 CdS는 다음의 뭉침 과정을 통해서 CdS 클러스터를 형성하게 된다.[7]

$$\begin{aligned} CdS + Cd &\rightarrow (CdS)_2 \\ CdS + (CdS)_2 &\rightarrow (CdS)_3 \\ &\vdots \\ (CdS)_m + (CdS)_n &\rightarrow (CdS)_{m+n} \end{aligned} \qquad (7)$$

Fig. 1은 감마선을 이용한 수용액상의 CdS 양자점 제조과정을 요약하여 간단하게 도식화한 것이다.

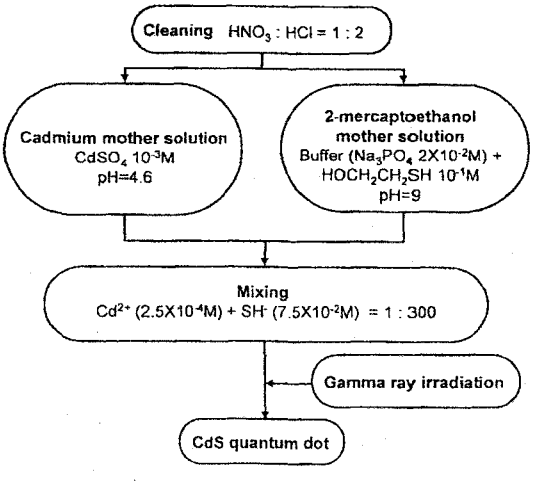

Fig. 1. 감마선을 이용한 CdS 양자점의 제조 과정.

결과 및 고찰

Fig. 2는 CdS 양자점의 생성과 크기 변화를 확인하기 위하여 감마선을 조사시키기 전에 측정한 카드뮴과 황을 섞은 용액의 흡수스펙트럼과, 감마선을 조사시킨 후 측정한 흡수스펙트럼을 보여주고 있다. *Fig.* 2에서 볼 수 있듯이 감마선을 조사하기 전에는 3.0 eV(413 nm)에서 4.0 eV(310 nm)의 파장 사이에서 CdS 양자점 구조의 엑시톤에 의한 흡수 봉우리가 관측할 수 없었으나, 감마선을 조사한 후에는 3.78 eV(328 nm)에서 CdS 양자점 형성에 의한 흡수 봉우리를 선명하게 관측할 수 있었다. 이 흡수 봉우리의 위치로부터 CdS 반도체 양자점의 크기를 이론적으로 계산하여 보면 CdS 양자점의 크기는 ~0.9 nm 임을 예측할 수 있다.1 따라서 감마선에 의하여 제조한 CdS 양자점의 크기는 일반적으로 온도 조절에 의한 합성법으로 제조한 양자점의 크기보다 더 작을 수 있음을 알 수 있다.[1-6]

Fig. 3은 감마선의 조사시간을 변화시키며 측정한 흡수스펙트럼을 관측한 것이다. 5분, 10분, 15분 동안 감마선을 조사시킨 후의 엑시톤 흡수 봉우리의 위치가 각각 3.67 eV(338 nm), 3.57 eV(347 nm), 3.38 eV(355 nm)이므로, 감마선의 양이 증가할수록 흡수 봉우리가 적색편이(red shift) 함을 알 수 있다. 조사 시간이 5분, 10분, 15분일 경우 조사된 감마선의 양은 각각 약 0.4 kGy, 0.9 kGy, 및 1.4 kGy에 해당한다. 따라서 엑시톤 흡수 봉우리의 위치를 바탕으로 이론적으로 예측해 볼 때 엑시톤 흡수 봉우리의 적색편이 결과는 CdS 반도체 양자점이 ~0.9 nm에서 ~1.5 nm의 크기로 성장하였음을 보여주고 있다. 또한 *Fig.* 3에서 점선으로 표시한 흡수 스펙트럼에 대한 Gaussian fitting 결과는 가장 낮은 에너지를 갖는 엑시톤 흡수 봉우리의 폭이 감마선을 10분, 혹은 15분 조사한 양자점의 경우 보다 감마선을 5분 조사한 CdS 양자점의 경우에 더 넓다는 사실을 보여주고 있다. 이는 크기가 작을수록 결정의 형태를 이루는 반응이 불안정하고 크기의 제어가 어려워진다는 것을 의미한다. 따라서 감마선을 충분히 조사시켜야만 양자점의 합성반응을 안정적으로 이루어지게 할 수 있어 결정의 크기도 균일하게 만들 수 있으며, 이에 따라 흡수 봉우리의 폭도 좁게 할 수 있음을 알 수 있다. 또한 *Fig.* 3은 10분 이상 감마선을 조사시킨 CdS 용액의 흡수봉우리 위치가 10분 이하로 조사시킨 경우보다 더 적색편이 하였음을 보여주고 있다. 즉 감마선을 0.4 kGy에서 0.9 kGy로 증가시킨 경우에는 파장이 9 nm 만큼 장파장으로 이동하였지만, 0.9 kGy에서 1.4 kGy로 증가시킨 경우에는 20 nm 이동하였음을 알 수 있다. 따

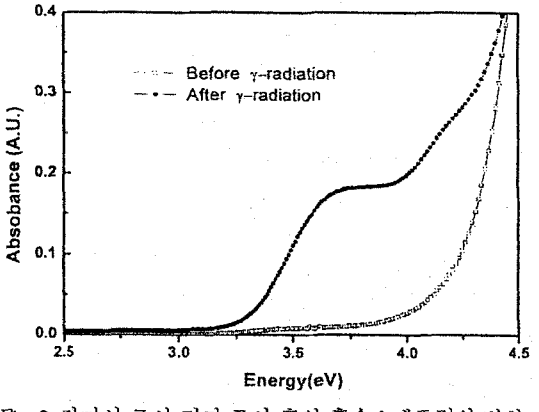

Fig. 2. 감마선 조사 전과 조사 후의 흡수스펙트럼의 변화.

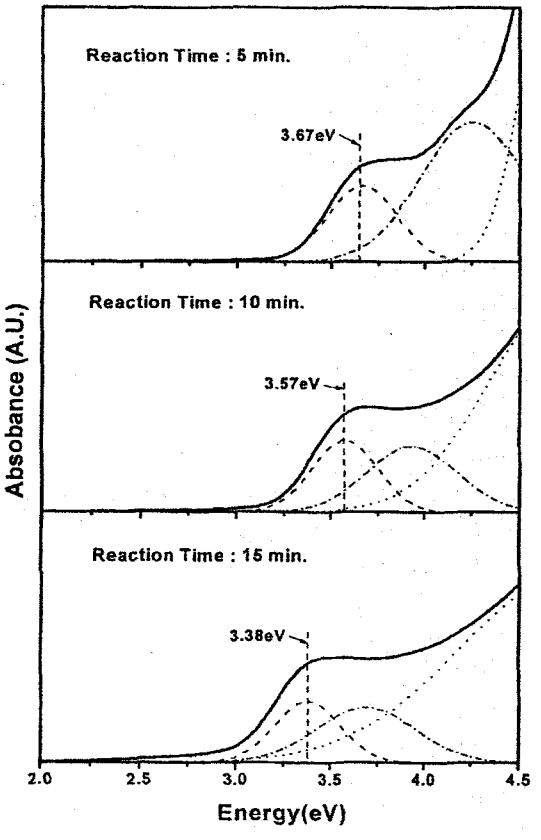

Fig. 3. 조사 감마선의 양에 따른 CdS 양자점의 흡수스펙트럼의 변화.

라서 감마선의 양을 0.9 kGy이상 조사하면, CdS 양자점 크기의 조절이 더욱 용이함을 알 수 있다.

결 론

감마선을 조사하여 양자점을 제조하는 방법은 모든 제조과정이 상온에서 이루어진다는 장점을 갖고 있다. 또한 감마선의 양을 조절함으로써 양자점의 크기를 1 nm 이하의 수준에서 정밀하게 변화시킬 수 있을 뿐만 아니라 그 변화과정도 단계별로 확인 할 수 있는 장점이 있다. 본 연구에서는 카드뮴과 황을 물속에서 혼합하고 감마선을 조사시킴으로써 안정적인 화학반응을 일어나게 하여 CdS 양자점을 제조하고, CdS 양자점의 형성을 흡수스펙트럼으로 관측하여 간접적으로 확인하였다. 또한 감마선의 양을 변화시켜 조사시킨 결과 CdS 엑시톤 흡수 봉우리가 적색편이하는 것을 확인함으로써 양자점의 크기를 체계적으로 조절할 수 있음을 간접적으로 확인할 수 있었다. 특히 감마선의 양이 0.9 kGy 이상이 될 때 안정적인 CdS 양자점을 제조할 수 있음을 알 수 있었으며 0.9 kGy 이상에서 감마선의 양을 조절하면 양자점의 크기 조절이 용이함을 알 수 있었다.

본 연구는 과학기술부 국가지정연구실(NRL: M1-0203-00-0082)사업의 지원으로 수행되었습니다.

인 용 문 헌

1. Banyai, L.; Koch, S. W. *Semiconductor Quantum Dots*; World Scientific: London, U.K., 1993; p 14.
2. Ko, M-J.; Plawsky, J.; Birnboin, M.; Mater, J. *Sci. Lett.* **1998**, *17*, 917.
3. Borelli, N. F.; Hall, D. W.; Holland, H. J.; Smith, D. W. *J. Appl. Phys.* **1987**, *61*, 5399.
4. Brus, L. E. *J. Chem. Phys.* **1984**, *80*, 4403.
5. Weller, H.; Schmidt, H. M.; Koch, U.; Fojtik, A.; Baral, S.; Henglein, A.; Kunath, W.; Weiss, K.; Dieman, E. *Chem. Phys. Lett.* **1986**, *124*, 557.
6. Alivisatos, A. P.; Harris, A. L.; Levinos, N. J.; Steigerwald, M. L.; Brus, L. *J. Chem. Phys.* **1988**, *89*, 4001.
7. Treguer, M.; de Cointet; Remita, C. H.; Khatouri, J.; Mostafavi, M.; Amblard, J.; Belloni, J.; de Keyzer, R. *J. Phys. Chem. B.* **1998**, *102*, 4310.
8. Belloni, J.; Mostafavi, M.; Remita, H.; Marignier, J. L.; Delcourt, M. O. *New. J. Chem.* **1998**, *22*, 1239.
9. Mostafavi, M.; Liu, Y. P.; Pernot, P.; Belloni, J. *Radiation Phys. and Chem.* **2000**, *59*, 49.
10. Buxton, G.; Grenstock, C. L.; Helman, W. P.; Ross, A. B. *J. Phys. Chem. Ref. Data* **1998**, *17*, 513.
11. Swayambunathan, V.; Hayes, D.; Schmidt, K.; Liao, X. Y.; Meisel, D. *J. Am. Chem. Soc.* **1990**, *112*, 3831.

Fabrication and Optical Characteristics of CdS/Ag Metal-Semiconductor Composite Quantum Dots

Eun-Hee Jeang, Jae-Hoon Lee, Koo-Chul Je, Sang-Youp Yim, Seung-Han Park,* Young-Soo Choi,† Joong-Gill Choi,† Mona Treguer,‡ and Thierry Cardinal‡

National Research Laboratory of Nonlinear Optics, Yonsei University, Seoul 120-749, Korea
†Department of Chemistry, Yonsei University, Seoul 120-749, Korea
‡ICMCB, CNRS, 87 av. Dr. Schweitzer, 33608 Pessac cedex, University Bordeaux I, France
Received April 13, 2004

Key Words : Quantum dot, Metal-semiconductor composite quantum dot, Plasmon resonance, Gamma ray irradiation, Quantum-confined Stark shift

There have been great interests in the optical, electrical, and chemical properties of quantized nanoparticles, such as semiconductor quantum dots (QDs).[1] Semiconductor QD structures particularly have attracted attentions because of their strong three dimensional quantum confinement effects. Researches have been held to develop better methods to fabricate such semiconductor QDs, showing great progress during the past decade. One of the most early developed fabrication methods is to embed II-VI semiconductor compound QDs into glass matrices.[2,3] However, recently, many research groups have established chemical fabrication methods of colloidal QDs dispersed in solution, which are comparatively more stable than those in glasses.[4-6] In particular, a radiolysis method utilizing a gamma ray source at room temperature has been actively and successfully conducted, which allows us to monitor the size of the sample during each fabrication process.[7-9] These colloidal QDs are produced by chemical reactions in equilibrium states, where the solution matrices act as a stabilizer, offering fast reaction time between the atoms as well as a slow growth rate during the fabrication procedure, helping to improve stability. In general, capping ligand is usually added to avoid aggregation of the nanoparticles and increase the solubility. Along with semiconductor QDs, solid metal nanoparticles also display distinctive and potentially productive properties. Characteristics of surface enhanced Raman scattering and surface second harmonic generation due to local field enhancement associated with plasmon resonance are well known examples of such the specialties.[10-12] Metal nanoparticles also have a large and fast third order optical nonlinearity opening possibilities for optical switching devices.[12] Fabrication methods of metal nano-structured particles, like in the case of semiconductor nanoparticles, have been continuously improved to reduce inhomogeneous broadening, optimizing their optical properties.

If the metal nano-structure is incorporated into the QD system, coupling between the plasmon resonance effect and the quantum size effect of the semiconductor QD may develop new aspects of nano-composite material systems and also widen applications for noble nano-devices.[13-17] In this article, the fabrication and optical characteristics of CdS/Ag semiconductor-metal composite QD structures are presented. The CdS QDs were made of cadmium sulfate and 2-mercaptoethanol by gamma ray irradiation in aqueous solution and silver was partially covered around the fabricated CdS QDs. The measured absorption spectra showed exciton peaks due to the quantum confinement effect as well as the surface plasmon resonance effect.[18,19] A red-shift of the CdS exciton absorption peak was observed, strongly indicating an enhancement of the local field in the semiconductor core. High Resolution Transmission Electron Microscopy (HRTEM) was also carried out to verify formation of CdS QDs and CdS/Ag composite QDs.

Experiments

The CdS QDs were prepared in water under the following five step processes as depicted in Figure 1. All processes were held under N_2 gas environment to prevent oxidation. First, cadmium sulfate ($CdSO_4$, M.W. = 78.13) was dissolved into super pure water to make a Cd^{2+} mother solution of 10^{-3} M at pH 4. Next, 0.1 M $HOCH_2CH_2SH$ mother solution of

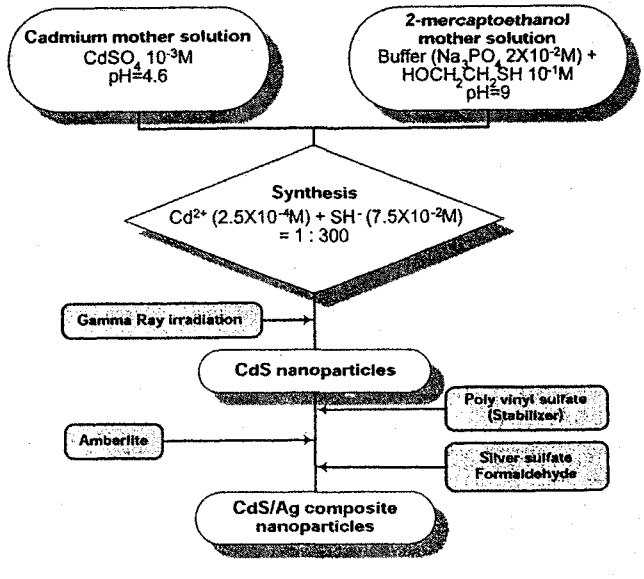

Figure 1. Five step fabricate processes of CdS quantum dots.

pH 9 was produced by combining 2-mercaptoethanol ($HOCH_2CH_2SH$, M.W. = 208.46) in a buffer solution made by dissolving sodium phosphate (Na_3PO_4) in water. Third, both solutions were mixed by adding the mother solution of Cd^{2+} and $HOCH_2CH_2SH$ solution with the ratio of concentration as 1 : 100, 1 : 200 and 1 : 300 at pH 7.5. Fourth, ^{137}Cs facility of 2500Ci was used to irradiate the solutions in the steady-state regime with a gamma-ray dosage of 0.3 kGy, 0.6 kGy, and 0.9 kGy, to produce CdS QDs using the hydrated electron e^-_{aq} as reducing species. Finally, in order to fabricate metal coated CdS/Ag with the previously made CdS QDs, the excess of 2-mercaptoethanol had to be removed. Then, a poly vinyl sulfate mother solution of 2×10^{-4} M was added to stabilize the CdS QDs, while resin and amberlite were used to remove the excess of 2-mercaptoethanol. 1 ml of the silver mother solution of 1.6×10^{-3} M using silver sulfate (Ag_2SO_4) was also annexed into the solution for the silver capping process. Finally, formaldehyde solution of 10^{-3} M was added to reduce the silver sulfate at the surface of the CdS QDs.

HRTEM investigations were performed using a Philips CM30 electron microscope, equipped with a high resolution stage to get information not only of the structure, but also of the texture of the materials at a nanometric scale. The spatial resolution in HR mode was 0.18 nm (point to point). The CM30 is equipped with a Low Illumination Digital camera which can directly catch the numerical micrography, providing a Fourrier Transform (FT) operation of the images on a full scale or on a selected Region of Interest (ROI).

Experimental Results

Figure 2 shows typical HRTEM pictures of a CdS QD and CdS/Ag composite QDs, which were fabricated by using the aforementioned method. As shown in Figure 2(a), an almost perfectly circular CdS QD can be fabricated, which has three different systems of fringes (3 crossed white arrows). The FT of a ROI indicated by a white dashed circle on the micrography gives the following inter reticular distances between the fringes: 2.41 ± 0.12 Å, 2.36 ± 0.11 Å and 2.035 ± 0.10 Å. Figure 2(b) displays the micrography of CdS QDs (low contrast) doped by Ag (high contrast). The ROI

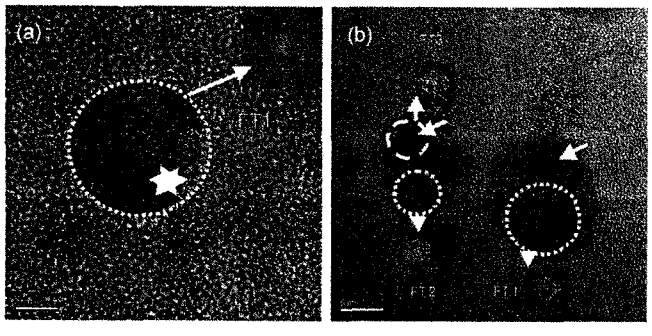

Figure 2. High-Resolution TEM image of (a) a CdS quantum dot and (b) CdS/Ag composite quantum dots. (The white small dashed circle corresponds to the ROI of the FT_1 and FT_2 and the white large dashed circle to the FT_3).

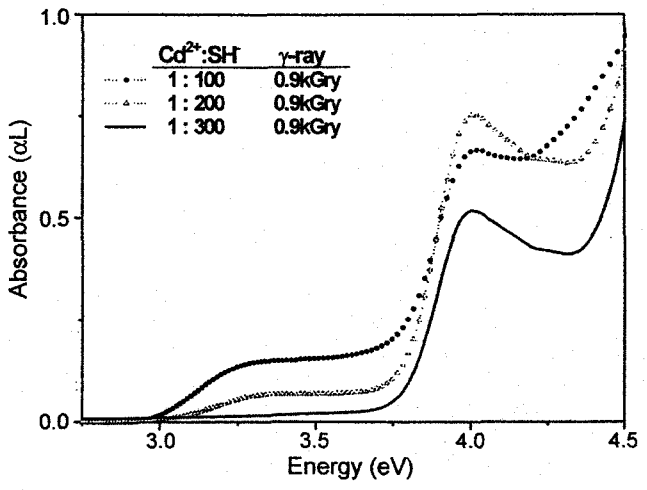

Figure 3. Absorption spectra of CdS quantum dots for varying concentration ratios of 2-mercaptoethanol.

selected presents two different systems of atomic fringes. The FT_1 and FT_2 for the ROI_1 and ROI_2 reveals the formation of CdS with inter reticular atomic distance of 3.417 ± 0.15 Å, 3.042 ± 0.15 Å, 2.410 ± 0.12 Å, 2.35 ± 0.11 Å, and 2.035 ± 0.10 Å, which are in accordance with value corresponding to CdS crystals in JCPDF files. The FT_3 of the ROI_3 exhibits a Debye-Scherrer pattern with fringes at 2.41 ± 0.12 Å and 2.213 ± 0.11 Å, indicating the partial growth of Ag hexagonal nano-crystals on the surface of the CdS QDs.

The effect of the concentration of 2-mercaptoethanol has been investigated on the preparation of smaller sized CdS QDs. In Figure 3, the absorption spectra for different ratios of $[Cd^{2+}]/[SH^-]$ is displayed. One can distinguish two bands at ~4.00 eV and ~3.35 eV corresponding to CdS QDs having an average radius of ~1.29 nm and ~1.75 nm, respectively. As the concentration of 2-mercaptoethanol, which acts as a stabilizer for the CdS QDs increase, the absorption band around 3.35 eV decrease in intensity and disappear

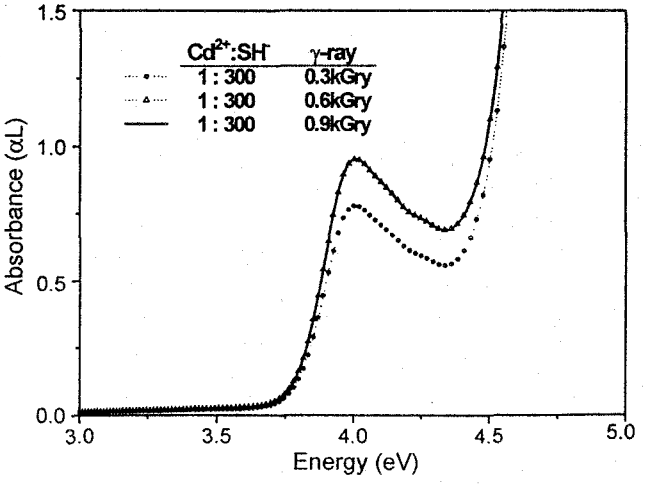

Figure 4. Absorption spectra of CdS quantum dots for different ã-ray dosage.

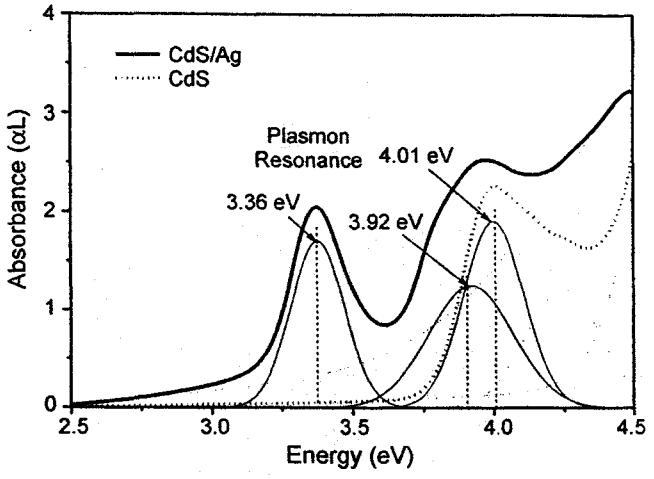

Figure 5. Absorption spectra after capping CdS quantum dots with silver ($[Cd^{2+}]/[SH^-]$ = 1/300, γ-ray = 0.9 kGry).

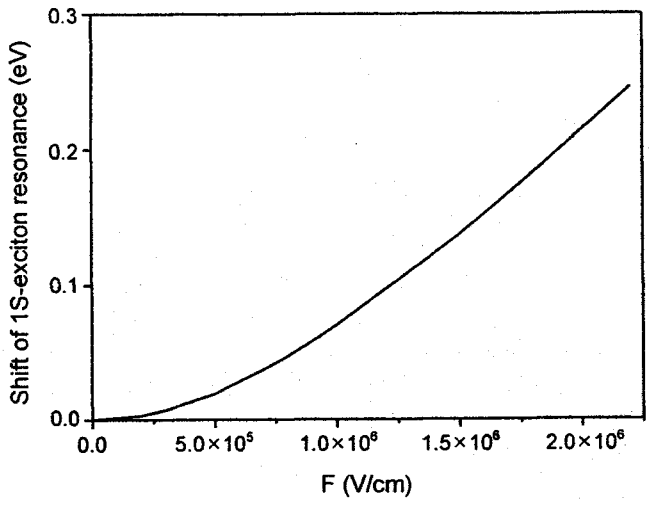

Figure 6. Calculated Stark shifts for a CdS QD of radius 1.29 nm as a function of external electric field based on the effective-mass Hamiltonian.

completely for a ratio $[Cd^{2+}]/[SH^-]$ of 1/300. This effect indicates that for stabilizing the particles, large amounts of 2-mercaptoetanol is necessary.

In Figure 4, the effect of the dose on the growth of CdS QDs is presented. Above a dose of 0.6 kGy, the maximum absorption at 4 eV remains constant indicating a complete reaction and a complete use of the cadmium concentration to form CdS QDs. For capping silver on the surface of the particles, therefore, a dose of 0.9 kGy and a concentration ratio $[Cd^{2+}]/[SH^-]$ of 1/300 has been used.

After the silver is added into the colloidal solution, two absorption peaks are apparent between 3.0 eV and 4.25 eV, as shown in Figure 5. Gaussian fitting of the absorbance reveals that a new peak is observed at 3.36 eV, which arises from the plasmon resonance of silver nanostructures originating from silver structures coating the CdS semiconductor QDs. In addition, the Gaussian fitting of exciton and plasmon resonance peaks shows that the pre-existent absorption peak at 4.01 eV has shifted to a lower energy by 0.09 eV to 3.92 eV. The red-shift of the absorption peak is attributed to be an effect due to the local-field enhanced by a metal structure surrounding the semiconductor core.

We have calculated the Stark shifts based on the effective-mass Hamiltonian in the presence of an external electric field, as shown in Figure 6. From this calculation, the local field is estimated to be approximately 1×10^6 V/cm for the observed red-shift of 0.09 eV. The calculations are determined by the electron-hole pair energy levels and the dipole moment matrix elements, which are obtained by the results of the numerical matrix diagonalization method.[20] Thus, we conclude that the red-shift of the absorption peak corresponding to the semiconductor core implies the strong local field effect in metal-coated semiconductor composite QD systems. The red-shift of the exiton peak as a function of the silver thickness is under investigation.

This research was supported by the Ministry of Science and Technology of Korea through the National Research Laboratory Program (Contact No. M1-0203-00-0082).

References

1. Banyai, L.; Koch, S. W. *Semiconductor Quantum Dots*; World Scientific: Singapore, 1993.
2. Borelli, N. F.; Hall, D. W.; Holland, H. J.; Smith, D. W. *J. Appl. Phys.* **1987**, *61*, 5399.
3. Brus, L. E. *J. Chem. Phys.* **1984**, *80*, 4403.
4. Weller, H.; Schmidt, H. M.; Koch, U.; Fojtik, A.; Baral, S.; Henglein, A.; Kunath, W.; Weiss, K.; Dieman, E. *Chem. Phys. Lett.* **1986**, *124*, 557.
5. Alivisatos, A. P.; Harris, A. L.; Levinos, N. J.; Steigerwald, M. L.; Brus, L. *J. Chem. Phys.* **1998**, *81*, 4001.
6. Jeong, Y. I.; Ryu, J. G.; Kim, Y. H.; Kim, S. H. *Bull. Korean Chem. Soc.* **2002**, *23*, 872.
7. Treguer, M.; Cointet, C.; Remita, H.; Khatouri, J.; Mostafavi, M.; Amblard, J.; Belloni, J.; Keyzer, R. *J. Phys. Chem. B* **1998**, *102*, 4310.
8. Belloni, J.; Mostafavi, M.; Remita, H.; Marignier, J. L.; Delcourt, M. O. *New. J. Chem.* **1998**, *22*, 1239.
9. Mostafavi, M.; Liu, Y. P.; Pernot, P.; Belloni, J. *Radiation Physics and Chemistry* **2000**, *59*, 49.
10. Nie, S.; Emory, S. R. *Science* **1997**, *275*, 1102.
11. Jang, N. H. *Bull. Korean Chem. Soc.* **2002**, *23*, 1790.
12. Antoine, R.; Brevet, P. F.; Girault, H. H.; Bethell, D.; Schiffrin, D. J. *J. Chem. Soc. Chem. Commun.* **1997**, 1901.
13. Averitt, R. D.; Westcott, S. L.; Halas, N. J. *J. Opt. Soc. Am. B* **1999**, *16*, 1824.
14. Moskovits, M. *Rev. Mod. Phys.* **1985**, *57*, 783.
15. Metiu, H. *Prog. Surf. Sci.* **1984**, *17*, 153.
16. Hache, F.; Ricard, D.; Flytzanis, C.; Kreibig, U. *Appl. Phys. A* **1998**, *47*, 347.
17. Ricard, D.; Roussignol, P.; Flytzanis, C. *Opt. Lett.* **1985**, *10*, 511.
18. Wokaun, A. *Solid State Phys.* **1984**, *38*, 224.
19. Joseph, W. H.; Zhou, H. S.; Takami, S.; Hirasawa, M.; Honma, I.; Komuyama, H. *J. Appl. Phys.* **1993**, *73*, 1043.
20. Hu, Y. Z.; Londberg, M.; Koch, S. W. *Phys. Rev. B* **1990**, *42*, 1713.

Available online at www.sciencedirect.com
SCIENCE DIRECT®
Chemical Physics Letters 394 (2004) 324–328
CHEMICAL PHYSICS LETTERS
www.elsevier.com/locate/cplett

Optical response of silver coating on CdS colloids

Frederic Rocco [a], Arvind K. Jain [a], Mona Treguer [a], Thierry Cardinal [a,*], Sylvie Yotte [b], Philippe Le Coustumer [b], Chang Youl Lee [a], Seung Han Park [c], Joong Gill Choi [c]

[a] *ICMCB, CNRS, 87 av. Dr. Schweitzer, University Bordeaux 1, 33608 Pessac cedex, France*
[b] *CDGA, Avenue des Facultés, University Bordeaux 1, 33405 TALENCE cedex, France*
[c] *Optics Laboratory, College of Science, Yonsei University, 134 Shinshon-dong, 120-749 Seoul, South Korea*

Received 1 June 2004; in final form 6 July 2004
Available online 28 July 2004

Abstract

Aqueous colloidal systems of composite silver metal and CdS semiconductor of different size were investigated. Coating the CdS colloids with silver islands leads to composite structures with electronic properties differing considerably to the sum of the separate particles. Evidence for the deposition of the silver on CdS is obtained from optical spectroscopy and High Resolution Transmission Electronic Microscopy.

1. Introduction

In correlation with the development of powerful laser sources, nanoparticles derived from metal and semiconductor have received particular attention because of their unusual linear and non-linear optical properties. The semiconductor particles in glasses have attracted attention as new non-linear optical material, since they possess a large third-order optical susceptibility in comparison to pure silica. Nevertheless, their non-linear optical response remains too low for practical use. Recently, it has been suggested that the well defined surface plasmon resonance exhibited by metallic nanosystem can enormously enhanced the oscillator strength of particles or molecules [1]. Theoretical and experimental investigations have demonstrated that non-linear Kerr effect could be enhanced by several orders of magnitude when the Mie resonance of a metal is combined with nanosemiconductor [2]. Those optical enhancement phenomena are expected by engineering spherical composite material consisting of a semiconductor core with a metallic shell, or vice versa. Of particular interest is the composite: CdS@Ag. The dielectric CdS quantum dots have an intrinsic large non-linear response due to an exciton resonance; whereas, among all metals, silver exhibits the most pronounced Mie resonance. So far, different methods of synthesis for coating the CdS dielectric nanoparticles with a metallic silver shell have been proposed in the literature. Ko et al. [3] has explored melt/quench method to achieve CdS@Ag in glass matrix. Soft chemistry has also been to prepare CdS@Ag by precipitation technique. Neuendorf et al. [4] have demonstrated that the nanocomposites constiting of a coating of metal exhibit enhanced intrinsic non-linear optical bistability. However, efforts have to be made to improve quality and reproductibility of the samples. In addition, no clear structural investigations for evidencing the implantation of silver on the semiconductor interface have been performed. In the present report, the preparation of CdS nucleus with silver island for two different sizes of CdS is described. The particles are made by reducing silver ions in a solution of CdS particles with a limited formation of individual silver particles. The absorption spectra and structural investigations are reported. The investigations confirm the high sensitivity of the optical

* Corresponding author. Fax: +33 (0) 1 5 56 84 27 61.
E-mail address: cardinal@icmcb.u-bordeaux1.fr (T. Cardinal).

0009-2614/$ - see front matter © 2004 Elsevier B.V. All rights reserved.
doi:10.1016/j.cplett.2004.07.022

properties of the colloidal particles on the chemical nature of the surface.

2. Experimental

2.1. Preparation of the nanocomposite CdS@Ag

2-Mercaptoethanol, cadmium sulfate, cadmium perchlorate, sodium sulfide, polyvinylsulfate PVS (MW = 10^5), methanol, sodium hexametaphosphate (HMP), formaldehyde, silver nitrate or sodium silver cyanide were of the highest purity available (Ardrich, Acros, Alfa Aeasar). Milli-Q grade water was used in all the preparations. All other chemicals were analytical grade. The silver coating was achieved on two size of CdS colloidal particles (<1 and about 15 nm) prepared from two different routes.

2.1.1. Smaller sized CdS particles (<1 nm)

Monodisperse colloidal CdS was prepared, by irradiating with the ^{137}Cs γ-rays source (3000Ci, 1.8 kGy/h), solutions of $CdSO_4$(2.5×10^{-4} M) and 2-mercaptoethanol (7.5×10^{-2} M) at a pH = 7.5 (buffer:sodium phosphate) in a closed glass vessel using the procedure described elsewhere [5,6]. In our experiments, the solutions have been exposed to γ-rays to a dose of 0.3 kGy, which leads to the formation of $(CdS)_n$ which have a mean diameter of 0.9 nm.

2.1.2. Larger sized CdS particles (about 15 nm)

The larger CdS colloid preparation followed a method decribed by Kumar and Jain [7] with slight modifications. $Cd(ClO_4)_2$ solution (0.1 mol dm^{-3}) was added drop-wise to HMP solution in a 500 ml flat bottom flask to obtain a reaction mixture having 3×10^{-4} mol dm^{-3} of each of these reactants. The pH was adjusted to nine and argon gas was flushed for about 15 min. Stoechiometric amount of SH^- was injected under vigorous stirring. The solution was finally flushed with N_2 for about 5 min.

2.1.3. Silver deposition on CdS seeds

In order to coat the CdS colloids, two methods were used to reduce Ag^+ ions. Firstly, a radiolytic method was tried which in other case has been quite useful [8]. $NaAg(CN)_2$ was added to CdS colloidal suspension at pH 7.5 as well as 0.3 mol of CH_3OH. The solution was degased in a sealed glass vessel by N_2O gas for 30 min. Exposure to γ-rays leads to the formation of organic radicals that transfer electrons to CdS particles. The stored electrons reduce the silver ions on the surface of CdS particles. However, it was found that part of the radicals reduced the silver ions directly in solutions, the result being that individual silver particles were also formed.

Second, formaldehyde was used as the reducing agent. When silver ions are reduced by formaldehyde in the absence of colloidal particles, an induction period of several minutes is observed. However, when CdS particles are present, the reduction occurs instantaneously and individual Ag_n particles are not produced. The following procedure was followed: first, the polyvinyl sulfate polymer was added to CdS solution to avoid the coalescence of the particles. Excess of ionic compounds was removed from the sol before PVS addition by treatment with Amberlite; second, 2×10^{-4} M formaldehyde was added to 50 ml of CdS solution (pH = 7.5). The solution was in a round flask under nitrogen. Several milliliters of deareted silver nitrate solution (5×10^{-5} and 10^{-3} M) was slowly injected under strong striring. During the injection, the spectral change took place immediately. The CdS concentration in the final solution was 2.5×10^{-4} M and the total concentration of silver added varied between 5×10^{-5} and 5×10^{-4} M.

2.2. Apparatus

The absorption spectra of colloidal suspensions were recorded using a cary5E spectrophotometer with a spectral resolution of 2 nm in an optical cell with an optical path of 10 mm.

For electron microscopy, small drops of solution were adsorbed on Cu grids coated with carbon membrane followed by the evaporation of the solvent in the air. The High Resolution Transmission Electronic Microscopy investigations were performed using a Philips CM30 electron microscope (300 keV). The spatial resolution is 0.18 nm. The CM30 is equipped with Low Illumination Digital camera from Gatan company to catch directly numerical micrography. Using the Gatan software, it is possible to perform Fourier Transform (FT) operation. This tool is useful for very fine analysis of very small domains, typically few nanometers.

3. Results and discussion

Fig. 1 shows the absorption spectra for the colloidal CdS particles less than 1 nm and the changes observed after the deposition of silver at various concentration. Before the deposition of silver, the irradiated solution of colloidal CdS is almost colorless (Fig. 1). The spectrum of colloidal CdS solution has a maximum at 330 nm and the onset is about 390 nm (≈3.05 eV); the absorption coefficient is 3000 l mol^{-1} cm^{-1}. A similar spectrum has been observed previously [6]. No change in the 300–330 nm region in the spectrum of the colloidal CdS is observed after removing the excess of mercaptoethanol groups and the addition of the polyvinylsulfate which has a weak absorption in the UV. The

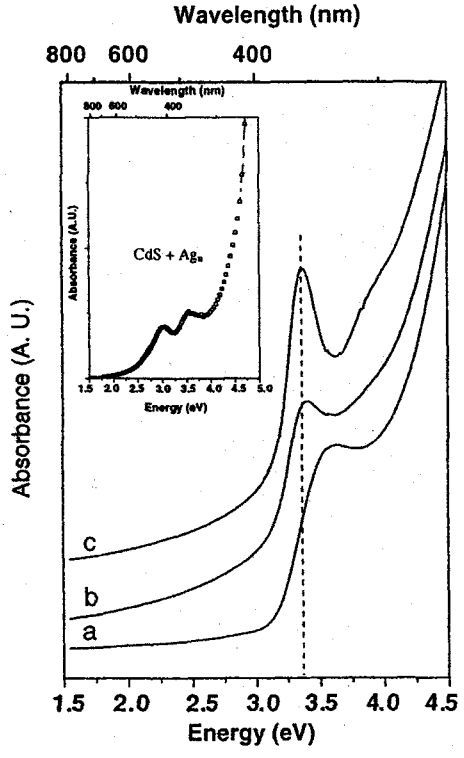

Fig. 1. Absorption spectra of CdS (2.5×10^{-4} M) before: (a) and after deposition of two different silver solution concentration, respectively, 5×10^{-5} M; (b) and 10^{-4} M; (c) [PVS] = 2.5×10^{-4} M. Irradiation dose: 0.3 kGy. *Inset.*: Spectrum of a mixture of separate, coexisting clusters of CdS (2.5×10^{-4}) and Ag_n (1×10^{-4} M) without interaction.

electron microscope pictures revealed well-separated crystalline CdS particles with a rather fine size distribution of 0.9 nm diameter. When silver is reduced, in a second step, by an aldehyde on the CdS nucleus, the composite particles present specific optical spectra with a maximum wavelength around 367 nm (≈3.4 eV). No strong absorption band in the 380–400 nm region due to the development of pure colloidal silver can be observed. In addition, as the silver concentration increases, the right-hand side peak is red-shifted (Fig. 1). The spectrum corresponding to the particles after silver growth is different from the one of a mixture of coexisting clusters of CdS and silver without any interaction. The spectrum would be in that case a sum of the two components characterized by two distinct maxima at around 345 nm (≈3.6 eV) and at around 420 nm (≈3 eV) as shown in the inset of the Fig. 1. Furthermore, note that the absorbance of the composite solution in the UV is much more intense below 340 nm than pure individual silver. These features of the absorption spectrum were attributed to composite with silver metallic formation on CdS. The electron micrograph indicates that the average size of mixed clusters is larger than that of pure CdS ones. However, the stuctural characterization of the nanocomposite is rather difficult due to their small size (about 1 nm). The silver deposition has been demonstrated through studies on larger CdS seeds described in the following paragraph.

The larger CdS particles prepared as decribed in the experimental section exhibit size about 15 nm and broad size distribution (from 1 up to 24 nm) according to TEM investigations. The absorption spectra of the CdS particles obtained by the precipitation method exhibit an onset at about 480 nm (≈2.6 eV), corresponding to the yellow coloration of the solution (Fig. 2). According to the optical band gap of hexagonal crystalline CdS at 2.52 eV at room temperature and the description of Brus [9] of the quantum confinement of semiconductor nanoparticles, our absorption spectrum data are in good agreement with particles about 15 nm and tend to bulk absorption feature. After reduction of silver on the surface of the CdS particles, a broad absorption band is observed around 370 nm (≈3.3 eV). For larger silver concentration, this band becomes narrower and is progressively red shifted to 390 nm (≈3.2 eV). The position of the bands appearing for composite materials between 350 and 390 nm is in accordance with the band observed for the smaller CdS particles picking at 367 nm. For both size, the optical responses of the composite materials are similar and indicate that silver has been formed on CdS as confirmed by the HRTEM investigation below.

High resolution micrograph pictures of uncoated and coated CdS are shown on Figs. 3 and 4, respectively. Before silver deposition, a perfect circular crystal of pure CdS of 16 nm of diameter can be observed. The electron diffraction experiments of this sample exhibit the typical parameters of hexagonal CdS. After silver deposition, the high resolution micrograph pictures of particles mostly exhibit darker contrast regions included into

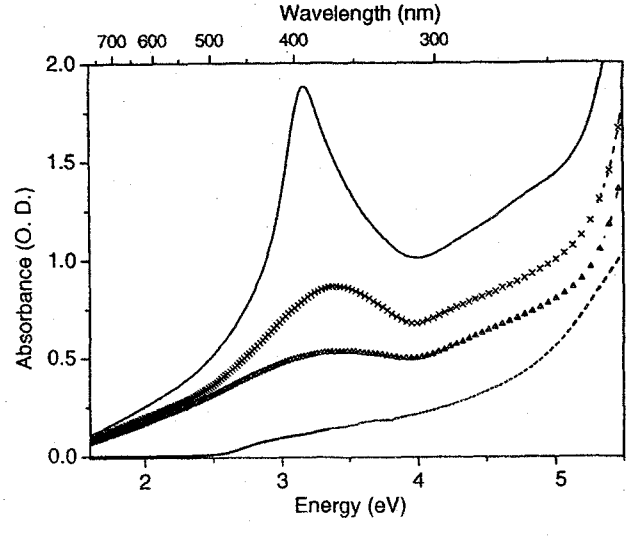

Fig. 2. Absorption spectra of colloidal CdS before(-·-·-) [CdS] = 3.0×10^{-4} M and after deposition of various silver amount: 5.0×10^{-4} (—), 3.0×10^{-4}M (×); 2.0×10^{-4} M (Δ).

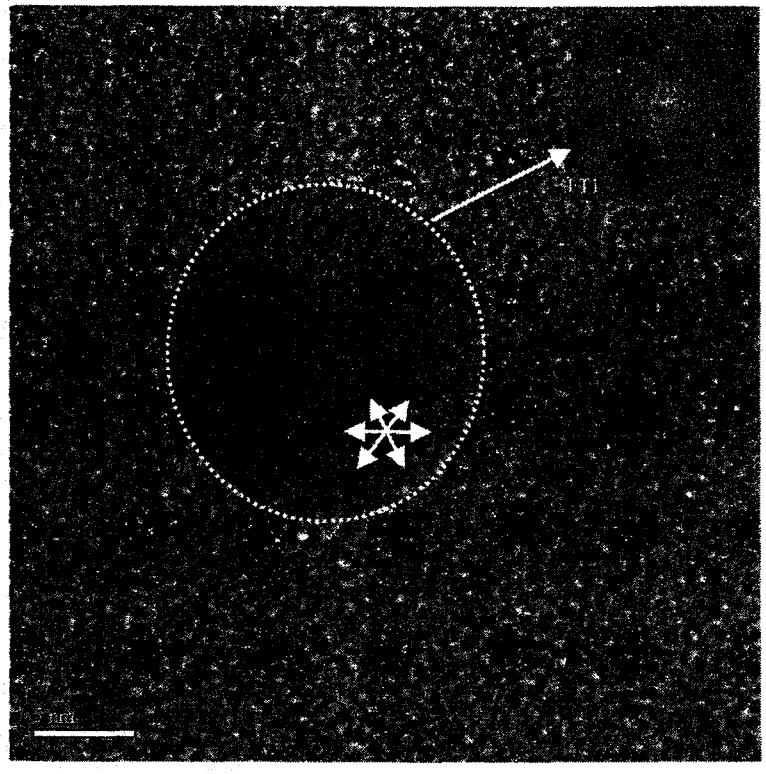

Fig. 3. High resolution micrography of CdS. The white circle represents the region where the TF has been done.

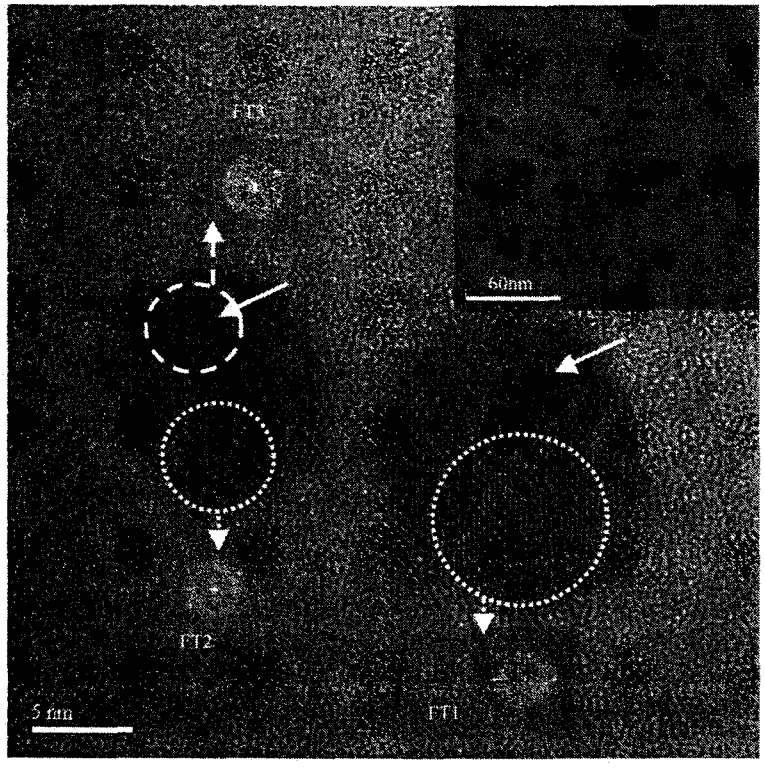

Fig. 4. High resolution micrography of CdS after silver coating. [CdS] = 3.0×10^{-4}; [Ag] = 5.0×10^{-4} M *Inset.*: Representative TEM image of silver coated CdS colloids.

the light gray CdS crystals. Fig. 4 shows two nanocrystals of different size: 10 nm of diameter (left one) and 12 nm (right one). Both of them present smaller domains more contrasted of about 5 nm of diameter (white arrows). Since thickness for each particle is the same (no thickness gradient along particles has been

observed), the difference of contrast has been attributed to a difference of chemical composition. The Fourier Transform (FT_1 and FT_2) gives, respectively, the following inter reticular atomic distances of 3.417 ± 0.15, 3.042 ± 0.15, 2.410 ± 0.12, 2.35 ± 0.11 and 2.035 ± 0.10 Å. While the FT_3 gives the following results: 2.41 ± 0.12, and 2.213 ± 0.12 Å. The maximum error for each measurement has been estimated to 5%. The lattice plane distances identified correspond to those of pure CdS and a silver phase: hexagonal Ag or acanthite Ag_2S. Since the lattice distance typical for those latter are close, none of those observations allow us to conclude on the exact nature of the Ag phase. Nevertheless, the comparison of our results of Figs. 1 and 2 from the spectra of CdS–Ag_2 S core-shell nanoparticles reported by several autors [10,11] clearly favor the formation of pure silver phase. The CdS particles coated with Ag_2S display a long absorption tail covering the entire visible spectra region. In addition, the concentrations of silver used are far above the concentration of 1% up to which Ag_2S can be formed in the CdS lattice [12]. Therefore, we conclude that pure silver islands were formed on the CdS particles. We cannot exclude that in the interfacial region between the CdS and Ag silver sulfide is present, since a substitution of Cd^{2+} ions in the CdS particles by Ag^+ takes place immediately [10]. This phenomenon is probably occurring in our case. However, no isolated Ag_2S particles were seen by HRTEM, only few individual Ag phase were observed (less than 1%) indicating also that the right experimental conditions have been found for avoiding the formation of individual silver particles. An image analysis on a survey of approximately 70 particles yields that 30% of the CdS particles were coated with silver. The fairly low yield of silver coating is probably due to the difference of lattice parameters of the both materials which favors the growth of the metal only on preferential directional lattice planes. This study confirms the high sensitivity of the optical properties of colloidal particles on the chemical nature of their surface. The presence of the metallic matter, even at low concentration (island and not a complete shell), on the interface, strongly influences the resonance frequencies of the small as well as the large CdS particles. The presence of a foreign material on the interface of colloids may have larger importance, even than its size effects.

Acknowledgements

This research has been sponsored by the Korean Ministry of Science and Technology and the French Embassy in Seoul. The authors would like also to acknowledge the support of CNRS and KOSEF (Grant No. 8884), of the French embassy in Seoul for this study and of the Ministry of Science and Technology through the National Research Laboratory Program (Contract No. M1-0203-00-0082).

References

[1] G.L. Fisher, R.W. Boyd, R.J. Gehr, S.A. Jenekhe, J.A. Osaheni, J.E. Sipe, L.A. Weller-Brophy, Phys. Rev. Lett. 74 (10) (1995) 1871.
[2] N. Kalyaniwalla, J.W. Haus, R. Inguva, M.H. Birnboim, Phys. Rev. A 42 (9) (1990) 5613.
[3] M.J. Ko, J. Plawsky, M. Birnboim, J. Non-Cryst. Solids 203 (1996) 211.
[4] R. Neuendorf, M. Quinten, U. Kreibig, J. Chem. Phys. 104 (16) (1996) 6348.
[5] V. Swayambunathan, D. Hayes, K. Schmidt, X.Y. Liao, D. Meisel, J. Am. Chem. Soc. 112 (1990) 3831.
[6] M. Mostafavi, Y. Liu, P. Pernot, J. Belloni, Radiat. Phys. Chem. 59 (2000) 49.
[7] A. Kumar, A.K. Jain, J. Photoch. Photobio. A 156 (2003) 207.
[8] A. Henglein, J. Phys. Chem. 97 (1993) 5457.
[9] L.E. Brus, J. Chem. Phys. 80 (1984) 4403.
[10] L. Spanhel, H. Weller, A. Fotjik, A. Henglein, Ber. Bunsenges. Phys. Chem. 91 (1987) 88.
[11] G. Hota, Colloids and Surfaces A 232 (2004) 119.
[12] K.T. Wilke, Naturwissenschaften 42 (1955) 603.

《연구논문》 Hankook Kwanghak Hoeji, Volume 15, Number 3, June 2004

광섬유 탐침의 반사를 이용한 파면 분석 근접장 주사 광간섭계

유장훈 · 임상엽 · 이현호 · 박승한†

연세대학교 이과대학 물리학과

㉾120-749 서울특별시 서대문구 신촌동 134번지

(2004년 3월 25일 받음, 2004년 5월 6일 수정본 받음)

광섬유 탐침의 끝 단에서 반사하는 광을 이용하는 근접장 주사 광간섭계를 제안하고, 제안한 근접장 주사 광간섭계를 이용하여 초점의 위치와 집광 초점면에서의 파면을 분석하였다. 파면의 분석은 광섬유 탐침의 끝 단에서 반사된 빛과 시료표면에서 반사된 빛을 간섭 시키고, 탐침의 끝 단을 $\lambda/4$씩 위상천이 시키면서 4장의 간섭무늬를 얻은 후, 위상천이 알고리즘을 통하여 광학 수차를 구하는 방법을 이용 하였다. 실험 결과 근접 주사시의 초점의 위치를 파장의 3분의 1 이하로 제어할 수 있음을 알 수 있었으며, 제안한 근접장 주사 광간섭계를 이용하여 구한 집광 초점면에서의 파면 수차 값이 트와이만-그린 간섭계를 이용하여 구한 파면 수차 값과 잘 일치함을 확인할 수 있었다.

주제어 : near-field scanning optical microscope, wave-front analysis, interferometer, nonlinear optics.

I. 서 론

최근 물질의 구조와 특성을 원자에서 분자 정도의 크기에 이르는 미시적인 수준에서 직접 관찰하고 조절하고자 하는 나노 기술에 관한 학문적 또는 산업적인 연구가 큰 주목을 받고 있다. 극미세 세계의 구조와 특성을 규명하고자 하는 이와 같은 나노기술의 발전은 주사 터널링 현미경(scanning tunneling microscopy: STM), 주사 힘 현미경(scanning force microscopy: SFM), 근접장 주사 광학 현미경(Near-field scanning optical microscope: NSOM) 등 주사 탐침 현미경(scanning probe microscope: SPM) 기술의 급속한 발전에 그 근거를 두고 있다. 이 중에서도 특히 시료 표면 부근에 국소적으로 구속되어 있는 근접장 광신호를 표면 근처의 일정한 거리에 위치한 매우 작은 개구(aperture)를 통하여 검출함으로써, 기존 광학계가 갖고 있는 회절 한계 이상의 고 분해능을 제공하는 근접장 주사광학 현미경 기술은 미세 구조를 영상화함과 동시에 상세한 분광학적인 정보를 제공할 수 있다는 점에서 21세기 나노기술 분야의 핵심기술 중의 하나로서 자리잡고 있으며, 현재 양자소자 특성평가, 고밀도 저장기기 개발, 분자 및 생체공학 연구 등 정보기술 및 생명기술 분야에 광범위하게 활발히 응용되고 있다.[1-3]

최근에는 고분해능의 근접장 탐침을 이용한 자체집광 현상과 같은 비선형 특성 연구가 활발히 진행되고 있다. 특히, 비선형 물질을 광기록용 매체시료로 사용하고 기록밀도의 한계를 극복하려는 시도가 있다.[4,5] 이러한 광기록용 시료의 비선형성을 조사 · 분석하려면 초점 면에서의 집광되는 광의 수차 특성이 매우 중요한 요소로 작용한다. 또한 비선형 시료에서의 자체집광 현상은 임계 광량을 넘어설 경우 시료의 구조적인 변화도 동반하기도 하는데,[6,7] 이러한 구조적인 변화는 집광 되는 광의 강도 뿐 아니라, 입사되는 광의 구면수차와 코마 등 집광 초점이 갖게 되는 파면의 성질에 의존한다. 따라서, 광학적 파면 분석은 광소자 응용에 있어서 매우 중요한 과정으로 인식되고 있다.

초점 면에서의 파면측정 과정에서 시료가 초점에서 벗어나는 경우에는 왜곡되거나 실제와는 상이한 정보를 얻게 되기 때문에, 시료 표면과 집광 초점 면의 상대적인 위치를 반드시 정밀하게 조절하여야 한다. 특히, 개구수가 높은 광학계를 사용하는 경우에는 제어해야 되는 초점의 심도가 ㎛이하이므로 매우 정교한 측정이 요구된다. 초점의 상대적인 정밀 위치 제어를 위하여 Z-scan 방법이 주로 사용되고 있으나, Z-scan 방법으로 초점의 위치를 sub-micron 이내로 제어한다는 것은 그리 쉬운 일이 아니다.[8]

따라서 본 논문에서는 근접장 주사 광학 현미경의 광섬유 탐침 끝에서 반사되는 광을 이용하여, 시료에 집광되는 초점의 공간적인 위치와 광의 파면을 측정할 수 있는 새로운 기능의 근접장 주사 광간섭계를 제안하고 연구한 결과를 제시하고자 한다. 제안한 근접장 주사 광간섭계는 초점면 가까이 위치한 근접장 광섬유 탐침의 끝 단으로부터 반사된 광과 시료에서 반사된 광이 서로 간섭을 일으키는 현상을 이용하였으며, 이 방법을 이용하여 초점의 위치를 측정할 경우 초점의 위치를 파장의 3분의 1 이하로 제어할 수 있음을 알 수 있었다. 또한, 탐침의 끝 단을 $\lambda/4$씩 위상천이시켜 얻은 간섭무늬들로부터 위상천이 알고리즘을 통하여 구한 집광 초점 면에서의 파면 수차 값이 트와이만-그린 간섭계를 이용하여 측정한 파면 수차 값과 잘 일치함을 확인 할 수 있었다.

†E-mail: shpark@phya.yonsei.ac.kr

II. 근접장 주사 광간섭계의 구성

제안한 근접장 주사 광간섭계의 개략도는 그림 1과 같다. 근접광을 관측하기 위해서는 사용하는 광의 파장보다 작은 직경의 광섬유 탐침을 이용하고 시료와 탐침 간 거리를 파장보다 짧게 유지시키는 shear-force 검출에 의한 시료-탐침 간 거리 유지가 필수적이다. Shear-force 검출은 수정 진동자(tuning fork)의 공명특성을 이용하는 방법이 널리 사용되고 있다.[9-12] 거리조절 신호로써 수정 진동자(tuning fork)의 진폭신호를 검출한 후 이미 설정된 기준값과 비교하면 탐침과 시료 사이의 거리를 일정하게 유지시킬 수 있다. 탐침은 주로 광섬유의 끝을 뾰족하게 만들고 100 nm 이하의 opening aperture 주위에 금이나 알루미늄 코팅을 하여 사용한다. 그러나 시료-탐침간 거리가 근접장에 접근한 경우에도 수정 진동자로부터 발생하는 검출신호가 영(zero)이 되지 못하는 문제점이 있다.[13,14] 이러한 문제점을 해결하고자 본 연구에서는 수정진동자의 주파수 특성을 비대칭적으로 만들어 높은 특이상수 값을 용이하게 얻을 수 있게 하면서, 검출신호가 탐침 접촉 시에 거의 나타나지 않도록 하는 방법을 적용하였다.[15] Piezoelectric 진동판 위에 수정 진동자를 부착시키고 수정 진동자의 한쪽 다리에 광섬유 탐침을 부착하여 탐침의 끝이 진동하도록 하였다. 그림 2(a)는 수정 진동자에 광섬유 탐침이 부착된 상태의 사진이다. 진동판을 비대칭으로 설계하여 수정 진동자의 진동 모드를 여러 개 발생시키고, 공명특성 곡선이 저주파 영역에서 급격히 증가하는 형태를 선택적으로 사용하였다. 이러한 비대칭적인 공명특성은 특이상수(Q-factor)를 쉽게 높일 수 있다. 특이상수의 정의된 값은 공진주파수를 공명특성 곡선의 반치폭(FWHM)으로 나누어 준 값이다. 근접장 광학 현미경의 탐침이 시료의 표면에 접근함에 따라 수정진동자의 공명주파수는 20 Hz 정도 증가하고, 진폭도 감소하는 것이 알려져 있다.[10] 따라서 공진주파수 부근의 저주파 영역의 주파수특성을 거리조절 신호로 이용하게 되고, 저주파수 영역의 기울기가 급격하면 할수록 거리 조절 신호의 감도가 증가하게 된다. 실제적인 특이상수 값은 그림 2(b)와 같이 저주파영역 만의 반치폭(HWHM)을 2배하고 이를 특이상수 값으로 고려하였다. 즉, 특이상수는 $Q=F_0/(2\Delta f)$로 정의할 수 있고 얻어진 값은 2730이었다. 이는 일반적으로 광섬유 탐침이 부착된 수정 진동자에서 얻어지는 특이상수 값(Q=1000)과 비교하여 상대적으로 높은 값이며, 일반적인 대칭적 공명주파수 특성을 이용하여 구한 결과보다도 우수한 특성이라고 볼 수 있다.[9] 따라서, 저주파수 영역의 기울기를 가파르게 만들기 위하여 수정진동자(tuning fork)의 공진주파수 특성곡선을 비대칭적으로 만들어 사용하는 경우에 그림 2(b)와 같이 Q-factor값이 큰 신호를 쉽게 얻을 수 있었다. 또한, 탐침이 시료에 근접할 때 잔류하는 기저신호(Background signal)를 그림 2(b)에서와 같이 현저하게 감소 시킬 수 있었다. 본 실험에서 사용한 수정 진동자의 공진주파수는 32768 Hz이었다.

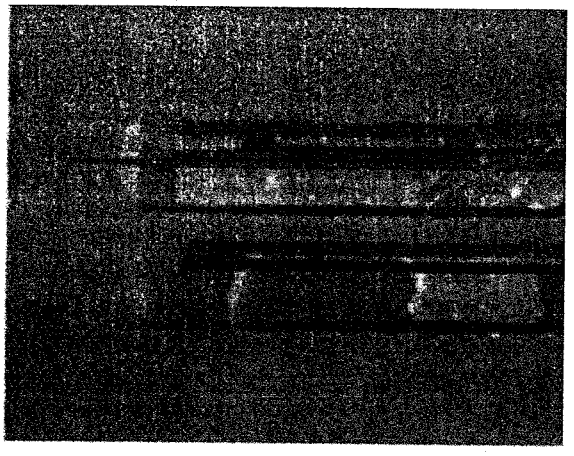

(a)

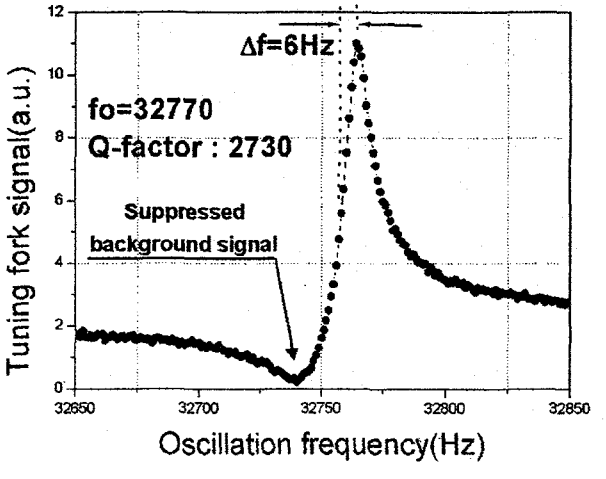

(b)

그림 2. 수정 진동자에 부착된 광섬유 탐침과 비대칭 공명특성.

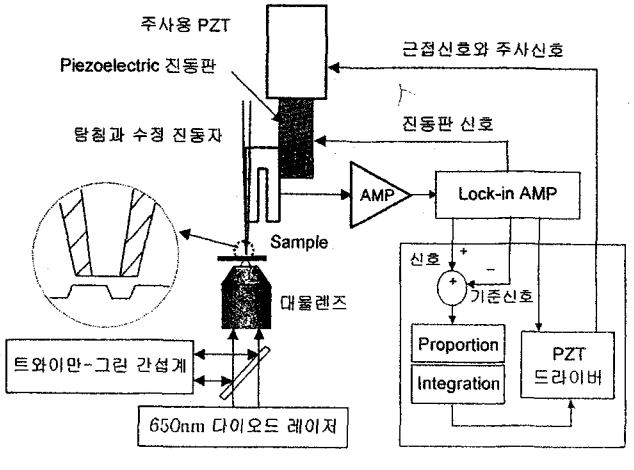

그림 1. 광섬유 탐침으로부터의 반사를 이용한 근접장 주사 광학 간섭계의 구조.

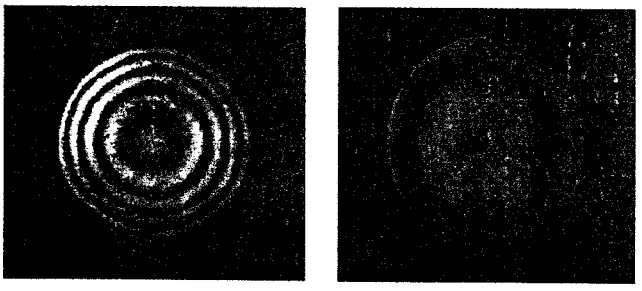

(a) (b)

그림 3. 나노 탐침이 근접장으로 접근함에 따라 시료 표면과 탐침으로 반사되어 생성된 간섭무늬: (a) Z~수 ㎛인 경우, (b) Z~10 nm에 근접한 경우, 여기서 Z는 탐침과 시료표면 사이의 거리.

한편, 그림 1에서와 같이 다이오드 레이저로부터 방출된 광이 대물렌즈를 통과한 후 시료 표면에 집광이 되게 하였고, 시료 표면에서 반사한 일부의 광은 대물렌즈를 다시 통과한 후 되돌아 가게 하였다. 이때, 근접장 탐침을 초점 면 근처에 위치시키면 나노 크기의 탐침으로부터 반사된 광이 새로운 광원으로써 역할을 하게 되므로, 탐침끝과 시료 표면으로부터 각각 반사된 광은 서로 간섭되어 그림 3(a)와 같은 동심원의 간섭무늬를 만들게 된다. 이때, 동심원의 중심이 간섭무늬의 중심과 일치하도록 조정하면서 탐침과 초점의 위치를 직선상에 정렬할 수 있으며, 동심원의 개수는 탐침이 시료의 표면에 근접할수록 줄어들게 된다. 대물렌즈를 통하여 시료에 집광된 광이 초점 이탈이 없는 경우, 탐침이 시료 표면의 근접장까지 접근하였을 때, 그림 3(b)와 같이 하나 이하의 동심원을 만들 수 있었다.

광섬유 탐침의 끝 단은 50 nm 정도의 열린 개구와 그 주위에 200 nm 정도의 두께로 금속 코팅된 구조를 가지고 있어서, 끝 단으로부터 반사된 광이 새로운 점 광원을 만들기 위한 적합한 모양을 가지고 있다. 탐침은 위치의 이동도 자유롭고, 탐침에서 반사된 광과 시료 표면에서 반사된 광을 서로 간섭시킨 상태에서, 탐침의 끝 단을 $\lambda/8$씩 이동시키면서 $\lambda/4$씩 위상천이 된 4장의 간섭무늬를 측정하고, 측정한 간섭무늬에 위상천이 알고리즘을 적용함으로써 초점에서의 파면수차를 구할 수 있도록 하였다. 이때 광원으로는 650 nm 레이저 다이오드를 사용하였으며, 시료로는 0.6 mm 두께의 광디스크를 사용하였다. 시료의 굴절률은 1.58이었다. 대물렌즈로는 0.7 mm의 두께가 보정된 개구수(N.A.) 0.6인 대물렌즈를 사용하였다. 또한, 제안한 근접장 주사 광간섭계를 이용하여 구한 파면 수차의 정확성을 확인하기 위하여, 시료 표면에서 되돌아 온 광의 일부를 광분할기를 통하여 트와이만-그린 간섭계에 입사시켜서, 기준 반사 면에서 반사된 광과 간섭을 일으키게 함으로써 간섭무늬를 만들고, 이 간섭무늬를 분석함으로써 파면 수차를 독립적으로 구할 수 있도록 구성하였다.

III. 초점 이탈과 파면 수차 측정 및 분석

위에서 언급한 바와 같이 대물렌즈를 통하여 시료에 집광된 광이 초점 이탈이 없는 경우에는 탐침 끝을 시료 표면에 근접장까지 접근하였을 때 하나 이하의 동심원만을 만들 수 있기 때문에, 동심원의 간섭무늬가 한 개 이하만 나타나도록 하면, 대물렌즈의 초점이 광디스크의 표면에 정확히 맺히도록 대물렌즈의 위치를 조절할 수 있었다. 탐침과 시료사이의 거리는 10~20 nm 정도로 제어하면서 집광된 광의 중심 경로와 탐침이 일직선 상에 정렬하도록 각별히 주의하였다. 이와 같이 동심원의 간섭무늬가 한 개 이하만 나타나도록 하여 초점의 위치를 정한 후, 대물렌즈와 시료의 위치를 고정한 상태에서, 탐침 끝 단을 파장의 8분의 1만큼씩 시료로부터 멀리 이동시키면서 그림 4의 (a)~(d)와 같은 $\lambda/4$씩 위상천이된 4장의 간섭무늬를 얻었다. 근접장(~10 nm)에서 PI control을 수행하면 sub-nanometer 이하의 정밀도를 가지고 거리유지가

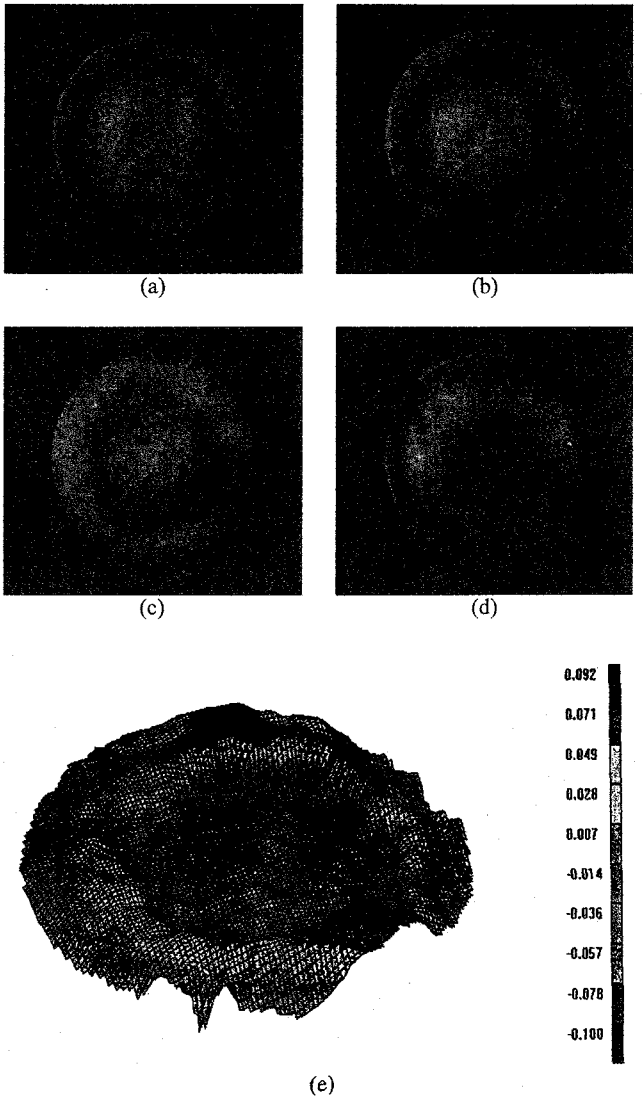

(a) (b) (c) (d) (e)

그림 4. 근접장에서 시료 표면과 광섬유 탐침의 끝 단으로부터 반사된 광들이 서로 간섭되어 얻어진 간섭무늬: (a) Z=~10 nm, (b) Z~90 nm, (c) Z~170 nm, (d) Z~250 nm, (e) (a)~(d)의 간섭무늬를 사용하여 계산된 파면, 여기서 Z는 탐침과 시료 표면 사이의 거리.

표 1. 제안한 근접장 주사 광간섭계를 통한 파면수차의 측정

항목	수차값(λ)	방향(도)	오차(λ)
초점이탈	-0.690		±0.005
코마	0.026	51.93	
비점수차	0.073	-84.19	
구면수차	-0.222		±0.005
RMS수차	0.035		
Peak값			

되고, 이때, 기준이 되는 fringe를 측정한 후에, PI control를 정지시킴과 동시에 Z축 거리 조절을 수행하는 주사용 PZT에 인가되는 전압을 조절하여 80 nm 정도의 거리를 이동시킨다. 이는 $\lambda/8$ 되는 값이며 시료 표면과 탐침에서 각각 반사되는 두 개의 반사광 사이에는 $\lambda/4$ 되는 위상차이를 갖게 된다. 거리 이동 후에 CCD를 이용하여 fringe를 다시 측정하고, 반복적인 수행을 통하여 4장의 위상천이된 간섭무늬를 얻을 수 있었다. 여기서 사용된 주사용 PZT는 nanometer이하의 거리조절이 가능한 소자이며 위상천이 과정에서는 ±10 nm 이하의 정밀도가 요구되지는 않기 때문에, PI control을 적용하지 않는 경우에도 파면의 위상 값을 복원할 수 있었다. 이때 4장의 간섭무늬로부터 위상천이 알고리즘을 이용하여 그림 4(e)와 같은 최적초점에서의 파면을 구할 수 있었으며, 이때 파면 수차의 값은 표 1과 같음을 알 수 있었다. 이때, 파면을 구하기 위하여 탐침의 끝단을 이동시켜야 하는 거리는 250 nm 정도이며, 초점 심도와 비교하여 상대적으로 작은 값이기 때문에 위상천이 과정에서 점 광원으로써의 역할이 충분히 유지되는 것으로 판단된다.

시료에서 반사된 광을 사용한 경우에 대칭적인 수차만이 측정 되고, 코마나 비점수차와 같은 비대칭 수차는 이론적으로 상쇄되어야 하지만, 본 실험에서는 미세하기는 하지만 코마나 비점수차가 존재하였다. 이는 미세한 초점 이탈이 존재하거나, 입사하는 광경로와 되돌아가는 광경로가 서로 정확히 일치하지 않거나, 광이 이미지소자로 진행하는 과정에서 추가적으로 발생하는 비점수차가 검출된 것 등으로 판단된다. 따라서, 근접장 주사 광간섭계로 측정한 이러한 초점이탈의 정도와 파면 수차 측정의 정확성을 살펴보기 위하여 트와이만-그린 간섭계를 이용하여 구한 측정 값들을 비교하여 보았다. 우선 탐침을 시료 표면에서 제거하여 탐침 끝에서 반사되는 광이 없도록 한 후, 시료 표면에서 반사하여 대물렌즈를 통하여 되돌아 온 광의 일부를 광분할기를 통하여 트와이만-그린 간섭계에 입사시켰다. 일반적으로, 트와이만-그린 간섭계를 통한 측정광은 시료 표면에 광이 정확히 집광되고 수차가 없다면 간섭무늬는 곧은 직선이 되지만, 시료가 광의 초점에서 벗어나 있다면 간섭무늬는 동심원을 만들게 된다. 이는 초점이탈 수차가 발생되어 간섭무늬를 휘게 만들기 때문이다. 이때, 광학 수차가 추가로 존재한다면 간섭무늬만을 관측하는 방법으로는 최소의 수차를 만족하는 조건을 결정하기 쉽지 않으므로, 초점의 위치를 바꾸면서 초점이탈에 따른 간섭무늬와 파면 수차를 측정하였다.

그림 5은 대물렌즈의 위치를 조정하여 (a) 시료 표면에 초점이 미치지 못한 경우와, (b) 최적의 초점에 위치한 경우, 그리고 (c) 초점이 시료 표면을 지나친 경우에 구한 간섭무늬를 보여주고 있다. 이 간섭무늬로부터 구한 그림 5의 (a), (b), (c)에서의 초점이탈 수차(W_{20})는 각각 -0.281λ, -0.694λ, -1.113λ 이었으며, RMS(root mean square)수차 값은 각각 0.040λ, 0.038λ, 0.041λ 이었다. 따라서, 대물렌즈의 위치가 이동하면서 초점이탈 수차가 구면수차와 상호 보정 되어 초점 이탈 수차(W_{20})가 -0.694λ 인 조건에서 최소의 파면 수차(0.038λ)를 보임을 알 수 있다.

이 결과는 본 논문에서 제안한 근접장 주사 광간섭계로부터 측정된 초점이탈 수차 값(W_{20}= -0.690λ)과 파면 수차 값(0.035λ)이 오차 범위($\pm 0.005\lambda$)안에서 잘 일치함을 보여준다. 또한, 파면 수차를 기준으로 하여 반복 측정 하면 초점이탈 수차 값(W_{20})이 $-0.690 \pm 0.050\lambda$ 이하가 되도록 제어가 가능함을 확인 할 수 있었다. 여기서, $\pm 0.050\lambda$ 범위의 초점 이탈 수차 값은 위치 공차로는 $\sim 0.280l\lambda$ ($2W_{20} / NA^2$) 이하에 해당된다.[16]

구면 수차의 주된 원인은 대물렌즈가 보정하는 기판의 두께가 0.7 mm인데 비하여 시료의 두께는 0.6 mm인 것에 기인한다고 생각되며, 이러한 구면 수차로 인하여 초점 이탈이 영(Zero)이 아닌 W_{20}=-0.690λ 근방에서 최소의 수차 값을 만족하였다. 이론적인 예측을 위하여 대물렌즈가 보정하는 0.7 mm 두께(D_l)의 기판은 굴절률을 1.50(n_l)이라고 가정할

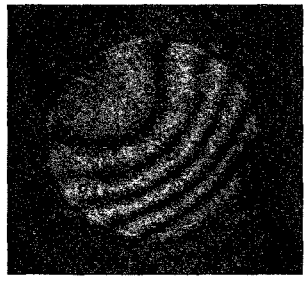

(a)

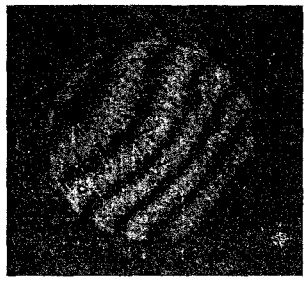

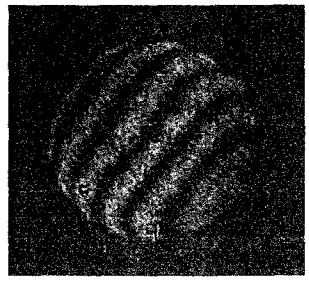

(b) (c)

그림 5. 나노 탐침을 제거하고 측정한 간섭무늬 : (a)시료 표면에 초점이 미치지 못한 경우, (b)시료 표면에 초점이 집광된 경우, (c) 초점이 시료 표면을 지나쳐서 벗어난 경우.

때, 실험에 사용한 0.6 mm 두께(D_2)의 광디스크의 굴절률은 1.58(n_2)이므로, 이론적인 3차 구면수차가 아래 식 (1) 과 같이 0.790 λ 발생하고 RMS wave-front error(σ)가 아래 식 (2)에서 최소가 되는 조건으로부터 초점이탈 수차도 W_{20} = $-W_{40}$ = −0.790 λ 근처의 값을 가질 것으로 예측된다.

$$W_{40} = \frac{1}{8}\left[D_1\frac{n_1^2-1}{n_1^3} - D_2\frac{n_2^2-1}{n_2^3}\right](NA)^4 \approx 0.790\lambda \quad (1)$$

$$\sigma^2 = \frac{1}{12}(W_{20}+W_{40})^2 + \frac{1}{180}W_{40}^2 \quad (2)$$

실험값(W_{20} = −0.690 λ)과 비교하여 발생한 초점 이탈의 오차(~0.1 λ)는 고차의 구면수차로부터 기인한다.

제안된 근접장 주사 광간섭계를 사용하면 기존의 트와이만-그린 간섭계의 기준 반사경으로부터 발생할 수 있는 시스템 에러를 제거할 수 있고, 여러 번의 반복된 측정을 통하여 얻을 수 있는 최소 수차의 조건을 단 한번의 측정으로 확인할 수 있다는 장점이 있으며, 동심원의 간섭무늬를 관측하면서 매우 정밀한 초점이탈의 조건을 찾음과 동시에, 파면 수차를 구할 수 있다는 장점이 있음을 알 수 있다. 또한, 본 논문에서 제안한 파면측정이 가능한 근접장 주사 광간섭계를 이용하면 근접장에서 시료에 집광된 최소크기를 갖는 초점의 광분포와 시료의 표면형상을 동시에 측정할 수도 있다. 따라서, 고밀도 광기록계에서 사용되는 기록매체 혹은 Bio-sample을 포함한 나노 크기의 시료 특성 분석, 광초점에서의 공간적인 광세기 분포가 매우 중요한 역할을 하는 자체집광 현상과 같은 비선형 연구, 광메모리용 디스크의 재생신호의 양호함을 판별하는 수차 및 지터(Jitters) 특성 분석 등에 활용될 수 있으리라 기대된다.[17]

IV. 결 론

본 논문에서는 이동 가능한 나노 크기의 광섬유 탐침에서 반사하는 광과 시료 표면에서 반사하는 광 사이의 간섭을 이용하는 새로운 기능의 근접장 주사 광 간섭계를 제안하였다. 파장이 650 nm인 다이오드 레이저 광원을 개구수(N.A.)가 0.6인 대물렌즈를 통과시킨 후 0.6 mm 두께의 광디스크 표면에 집속시킨 후, 제안한 근접장 주사 광간섭계를 이용하여 초점의 위치와 초점에서의 파면을 측정하였다. 측정한 초점의 위치와 초점 면에서의 파면을 트와이만-그린 간섭 방법에 의한 측정값과 비교 분석한 결과, 제안한 근접장 주사 광간섭 방법을 이용할 경우 초점의 위치를 sub-micron이하(< λ/3)로 제어할 수 있음을 알 수 있었다. 또한, 탐침의 끝 단을 λ/4씩 위상천이 시킨 후 구한 4장의 간섭무늬에 위상천이 알고리즘을 적용하여 구한 파면 수차가 트와이만-그린 간섭계를 이용하여 구한 파면 수차와 잘 일치함을 확인할 수 있었다. 본 연구의 결과는 고밀도 기록계에 사용되는 비선형 물질의 광디스크 분석을 위하여 초점 및 표면형상의 관계뿐만 아니라 수차와의 상관관계를 예측하는 평가기술로서 효과적으로 활용될 수 있으리라 기대된다.

감사의 글

본 연구는 과학기술부 국가지정연구실(NRL:M1-0203-00-0082) 사업의 지원으로 수행되었습니다.

참고문헌

[1] E. A. Ash, and G. Nicholls, "Super-resolution aperture scanning microscope," *Nature*, vol. 237, pp. 510-512, 1972.

[2] D. W. Pohl, W. Denk, and M. Lanz, "Optical stethoscopy: image recording with resolution l/20," *Appl. Phys. Lett.*, vol. 44, pp. 651-653, 1984.

[3] E. Betzig, J. K. Trautmann, T. D. Harris, J. S. Weiner, and R.L. Kostelak, "Breaking the diffraction barrier: optical microscopy on a nanometric scale," *Science*, vol. 251, pp. 1468-1470, 1991.

[4] W.C. Liu, C.Y. Wen, K.H. Chen, W.C. Lin, and D.P. Tsai, "Near-field images of the AgOx-type super-resolution near-field structure," *Appl. Phys. Lett.*, vol. 78, pp. 685-687, 2001.

[5] L. P. Shi, T. C. Chong, H. B. Yao, P. K. Tan, and X. S. Miao, "Super-resolution near-field optical disk with an additional localized surface plasmon coupling layer," *J. Appl. Phys.*, vol. 91, pp. 10209-10211, 2002.

[6] H. Hisakuni, K. Tanaka, "Optical Microfabrication of Chalcolgenide Glasses," *Science*, vol. 270, pp. 974 (1995).

[7] O. Salminen, N. Nordman, P. Riihola, and A. Ozols, "Holographic recording and photocontraction of amorphous As2S3 films by 488.0 nm and 514.5 nm laser light illumination," *Opt. Comm.*, vol. 116, pp. 310-315, 1995.

[8] K. Song, J. Lee, J. Kim, K. Cho, and S. Kim, "Direct Observation of Self-Focusing with Subdiffraction Limited Resolution Using Near-Field Scanning Optical Microscope," *Phys. Rev. Lett.*, vol. 85, pp. 3842-3845, 2000.

[9] K. Karrai, R. D. Grober, "Piezoelectric tip-sample distance control for near field optical microscopes," *Appl. Phys. Lett.*, vol. 66, 1842-1844, 1995.

[10] A. G. T. Ruiter, J. A. Veerman, K. O. van der Werf, and N. F. van Hulst, "Dynamic behavior of tuning fork shear-force feedback." *Appl. Phys. Lett.* vol. 71, pp. 28-30, 1997.

[11] R. D. Grober, J. Acimovic, J. Schuck, D. Hessman, P. J. Kindlemann, J. Hespanha, and A. S. Morse, K. Karrai, I. Tiemann, and S. Manus, "Fundamental limits to force detection using quartz tuning forks," *Rev. Sci. Instrum.* vol. 71, pp. 2776-2780, 2000.

[12] W. A. Atia and C. C. Davis, "A phase-locked shear-force microscope for distance regulation in near-field optical

microscopy," *Appl. Phys. Lett.*, vol. 70, pp. 405-407, 1997.
[13] R. S. Decca, H. D. Drew, and K. L. Empson, "Mechanical oscillator tip-to-sample separation control for near-field optical microscopy," *Rev. Sci. Instrum.*, vol 68, pp. 1291-1295, 1997.
[14] J. Salvi, P. Chevassus, A. Mouflard, S. Davy, M. Spajer,and D. Courjon, "Piezoelectric shear force detection: A geometry avoiding critical tip/tuning fork gluing," *Rev. Sci. Instrum.*, vol. 69, pp. 1744-1746, 1998.
[15] "Enhancement of shear-force detection sensitivity using asymmetric response of tuning forks for near-field scanning optical microscopy," submitted to Appl. Phys. Lett., 2004.
[16] G.Bouwhuis, J. Braat, A. Huijser, J. Pasman, G. Van Rosmale and K. Schouhamer Immink: Principles of optical disc system (Adam Hilger Ltd., Bristol and Boston) pp. 41, 1986.
[17] J. Yoo, C. Lee, K. Cho, H.Choi, and J.Lee, "An optical head with special annular lens for laser disc-compatible digital versatile disc pickup," *Jpn. J. Appl. Phys.*, vol. 37, pp. 2184-2188, 1998.

Near field scanning optical interferometer using facet reflection of a tapered optical fiber

Jang-Hoon Yoo, Sang-Youp Yim, Hyun-Ho Lee, and Seung-Han Park†

National Research Laboratory of Nonlinear Optics, Yonsei University, Seoul 120-749, Korea
† *E-mail: shpark@phya.yonsei.ac.kr*

(Received March 25, 2004, Revised manuscript May 6, 2004)

We propose a near- field scanning optical interferometer (NSOI) based on the facet reflection of a nano-sized moveable tapered optical fiber. The interferometer can measure the position and the wave-front of a focused spot simultaneously. The interfering fringes are generated by the reflected beams from the sample surface and from the fiber facet. The wave-front analysis at the focusing position is obtained by using a phase shifting technique with a four-step algorithm. It is found that the resolution for controlling the focal position of our proposed NSOI is less than $\lambda/3$ and the measured wave-front aberration at the focal position is in good agreement with the ones obtained by a Twyman-Green interferometer.

OCIS Codes : 120.3180, 120.5050, 180.5810, 220.4840.

Finite-difference time-domain analysis of self-focusing in a nonlinear Kerr film

Hyun-Ho Lee, Kyu-Min Chae, Sang-Youp Yim, and Seung-Han Park

National Research Laboratory of Nonlinear Optics, Yonsei University, Seoul 120-749, Korea
shpark@phya.yonsei.ac.kr

Abstract: By using a finite-difference time-domain method, we analyze self-focusing effects in a nonlinear Kerr film and demonstrate that the near-field intensity distribution at the film surface can reach a stable state at only a few hundred femtoseconds after the incidence of the beam. Our simulations also show that the formation of multiple filamentations in the near-field is quite sensitive to the thickness of the nonlinear film and the power of the laser beam, strongly indicating the existence of nonlinear Fabry-Perot interference effects of the linearly polarized incident light.

OCIS codes: (260.5950) Self-focusing; (190.0190) Nonlinear optics; (190.3270) Kerr effect; (190.4720) Optical nonlinearities of condensed matter

References and links

1. R. Y. Chiao, E. Garmire, and C. H. Townes, "Self-trapping of optical beams," Phys. Rev. Lett. **13**, 479 (1964).
2. V. I. Talanov, "Self-focusing of waves in nonlinear media," JETP Lett. **2**, 138 (1965).
3. J. A. Fleck, Jr., and P. L. Kelley, "Temporal aspect of the self-focusing of optical beams," Appl. Phys. Lett. **15**, 313 (1969).
4. M. D. Feit, and J. A. Fleck, Jr., "Beam nonparaxiality, filament formation, and beam breakup in the self-focusing of optical beams," J. Opt. Soc. Am. B **5**, 633 (1988).
5. K. D. Moll, A. L. Gaeta, and G. Fibich, "Self-similar optical wave collapse: observation of the townes profile," Phys. Rev. Lett. **90**, 203902-1 (2003).
6. G. Fibich and A. L. Gaeta, "Critical power for self-focusing in bulk media and in hollow waveguides," Opt. Lett. **25**, 335 (2000).
7. G. Fibich and B. Ilan, "Multiple filamentation of circularly polarized beams," Phys. Rev. Lett. **89**, 013901-1 (2002).
8. G. Fibich and B. Ilan, "Vectorial and random effects in self-focusing and in multiple filamentation," PHYSICA D **157**, 112 (2001).
9. G. Fibich, W. Ren, and X.-P. Wang, "Numerical simulations of self-focusing of ultrafast laser pulses." Phys. Rev. E **67**, 056603 (2003).
10. R. M. Joseph, A. Taflove, "Spatial soliton deflection mechanism indicated by FDTD Maxwell's equations modeling," IEEE Photon. Tech. Lett. **6**, 1251 (1994).
11. R. W. Ziolkowski, and J. B. Judkins, "Full-wave vector Maxwell equation modeling of the self-focusing of ultrashort optical pulses in a nonlinear Kerr medium exhibiting a finite response time," J. Opt. Soc. Am. B **10**, 186 (1993).
12. K. B. Song, J. Lee, J. H. Kim, K. Cho, and S. K. Kim, "Direct observation of self-focusing with subdiffraction limited resolution using near-field scanning optical microscope," Phy. Rev. Lett. **85**, 3842 (2000)
13. Y. Choi, J. H. Park, M. R. Kim, W. Jhe, and B. K. Rhee, "Direct observation of self-focusing near the diffraction limit in polycrystalline silicon film," Appl. Phys. Lett. **78**, 856 (2001)
14. J. Tominaga, T. Nakano, and N. Atoda, "An approach for recording and readout beyond the diffraction limit with an Sb thin film," Appl. Phys. Lett. **73**, 2078 (1998).
15. K. S. Yee, "Numerical solution of initial boundary value problems involving Maxwell's equations in isotropic media," IEEE Trans. Antennas Propagat. **14**, 302 (1966).

#4213 - $15.00 US
Received 20 April 2004; revised 20 May 2004; accepted 26 May 2004

1. Introduction

Self-focusing, a well-known nonlinear phenomenon, has been extensively investigated, since the intensity-dependent refractive-index gradient may effectively reduce the diffraction limited spot-size [1,2]. Theoretically, the beam propagation method (BPM)[3,4], nonlinear Schrödinger equation (NLSE) [5-9], and finite-difference time-domain (FDTD) method [10,11] etc. have been employed to understand the temporal and spatial electromagnetic-field variations in nonlinear bulk media, including the self-focusing effect. By using a non-paraxial BPM based on the Helmholtz equation, Feit and Fleck [4] reported that the non-paraxial treatment of the nonlinear process limits the decrease in beam size to the order of one optical wavelength, leading to multiple foci, beam breakup and filament formation. Fibich and Ilan [7] showed that multiple filamentation can be suppressed for the circularly polarized beams in a Kerr medium using a scalar equation to describe self-focusing in the presence of vectorial and non-paraxial effects. The finite-difference time-domain (FDTD) method, which represents the electromagnetic-field vectors in the time domain without paraxial approximation, has also been utilized to study the complex nonlinear phenomenon. Especially, the time-dependent features of nonlinear material, such as the femtosecond optical pulse propagation in a nonlinear Kerr medium [11] and the formation of temporal solitons [10], have been investigated with the FDTD method, since it is a convenient tool to describe the temporal dynamics of nonlinear materials.

The self-focusing phenomenon, including beam breakups and multiple filamentations, has been experimentally observed in bulk medium only for sufficiently intense laser beams. Recently, however, it has been shown that self-focusing effects can be directly observed in nonlinear thin films with a low-power continuous-wave (CW) laser by using a near-field scanning optical microscope [12-14]. Song *et al.* [12] showed that filaments with a minimum size of 0.3 μm were observed in 1.7 μm thick arsenic trisulfide (As_2S_3) films with a 1.6 mW laser diode. Choi *et al.* [13] reported that the optically focused beam size can be decreased below the diffraction-limit in a 0.3 μm thick polycrystalline silicon (p-Si) film in the near-field region. Since self-focusing in thin films have more complex features than that in bulk media due to multiple reflections, few theoretical approaches for the nonlinear processes in the thin films have been discussed. In this letter, we present a three-dimensional (3D) FDTD analysis of the self-focusing effects in the nonlinear Kerr thin-films at various configurations. Our simulations show that the nonlinear Kerr film exhibits quite different filamentation features than that of bulk materials due to nonlinear Fabry-Perot interference of linearly polarized incident light.

2. FDTD analysis of self-focusing in a nonlinear Kerr film

The interaction of a beam of light and a nonlinear optical medium can be expressed in terms of the nonlinear polarization. In the time domain, the nonlinear electric polarization (in MKS units) is given by [11]

$$\mathbf{P}^{NL}(x,t) = \varepsilon_0 \int_{-\infty}^{\infty} \chi^{(3)}(t-\tau)\left|\mathbf{E}(x,\tau)\right|^2 \mathbf{E}(x,t)d\tau \tag{1}$$

where $\chi^{(3)}(t)$ is the time-dependent third-order nonlinear susceptibility. The third-order nonlinear susceptibility of Kerr-type materials can be assumed as an instantaneous-response model: $\chi^{(3)}(t) \cong \chi_0^{(3)}\,\delta(t)$, since the relaxation time of Kerr-type materials is of the order of or less than 10 fs [10,11]. Then, the nonlinear electric polarization can be obtained by

$$\mathbf{P}^{NL}(x,t) \cong \varepsilon_0 \chi_0^{(3)}\left|\mathbf{E}(t)\right|^2 \mathbf{E}(t) \tag{2}$$

where $\chi_0^{(3)}$ is the third-order electric susceptibility. In our simulation, we assume that the first and third-order electric susceptibilities are constant. In this model, the self-induced

#4213 - $15.00 US
Received 20 April 2004; revised 20 May 2004; accepted 26 May 2004

refractive index gradients grow linearly with the laser intensity, $n = n_0 + n_2 \varepsilon |\mathbf{E}|^2 / 2 = n_0 + n_2 I$, where n_0, n_2, and I are the linear refractive index, nonlinear refractive index, and laser beam intensity, respectively. Finally, the electric field in the nonlinear Kerr material is assumed to be as follows [8,10,11]:

$$\mathbf{E}(t) = \frac{\mathbf{D}(t)}{\varepsilon_0 (1 + \chi^{(1)} + \chi_0^{(3)} |\mathbf{E}(t)|^2)} \tag{3}$$

where $\chi^{(1)}$ is are the first-order electric susceptibility

In each iteration step of the FDTD method, the latest value of **E** can be calculated from the latest value of **D** and the old value of **E**. Therefore, Eq. (3) gives us a complete description of the computational FDTD model for the Kerr nonlinearity. Since the electric field components (E_x, E_y, E_z) are separated spatially by Yee algorithm in the 3D FDTD method [15], in addition, the electric fields are interpolated on the grid for the calculation of $|\mathbf{E}(t)|^2$ in Eq. (3).

For FDTD simulations, it is also assumed that the nonlinear Kerr thin film is deposited on a glass substrate and the linearly-polarized CW laser light of wavelength (λ_0) 632.8 *nm* is incident on the film after passing through the grass substrate. In addition, it is assumed that the incident light of radius 1 μm has a Gaussian intensity distribution and the refractive index (n_0) and the nonlinear refractive index (n_2) of the film are 2.61 and $4\times10^{-10}\ m^2/W$ ($\chi_0^{(3)} \cong 9.244\times10^{-21}\ m^2/V^2$), respectively. Therefore, in our configuration the average intensity of a Gaussian beam produced from a 5 *mW* laser provides approximately I_{ave} = power / 2π (beam radius)$^2 \cong 0.796\times10^9\ (W/m^2)$, giving the effective refractive index and wavelength of $n_{eff} = n_0 + n_2 I_{ave} \cong 2.928$ and $\lambda_{eff} = \lambda_0 / n_{eff} \cong 216\ nm$, respectively. With all these assumptions, the near-field intensity distributions at the film surface are calculated as functions of total power of the incident beam and film thickness by using the 3D FDTD method.

Figure 1 shows the temporal dynamics of the near-field intensity distribution at the film surface for a time period of 2 picoseconds. The stabilization process of the filamentation in a nonlinear Kerr film is clearly revealed. When the intense light is incident on the film surface, one can expect that the two time-dependent elements, originating from the change of the refractive index and the momentum vector of focused beam, produce much more complex features compared to bulk materials because of the multiple reflections on both sides of the nonlinear film. As can be seen in Fig. 1, however, it is found that the near-field intensity distribution at the film surface reaches a stable state at around 300 femtoseconds after the beam incidence. In addition, our simulations show that the time to reach a stable filament formation is quite sensitive to the film thickness, beam power, and wavelength, strongly indicating that nonlinear Fabry-Perot interference is playing a significant role in the Kerr film.

In order to check the existence of multiple interference effects in the Kerr film, we compare the FDTD simulation result of the thin film with that of the bulk medium. We calculate the intensity distribution in the bulk medium after the same propagation distance without reflections from the second boundary, as shown in Fig. 2. It is clearly found that multiple filamentation does not appear in the nonlinear Kerr bulk medium in contrast to the case of the thin film.

#4213 - $15.00 US
Received 20 April 2004; revised 20 May 2004; accepted 26 May 2004

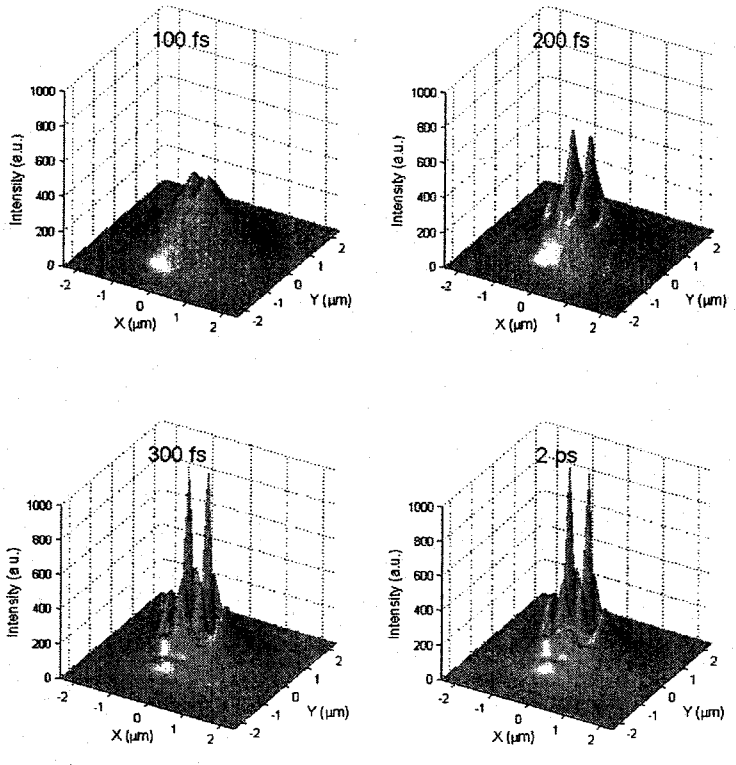

Fig. 1. Temporal dynamics of intensity distribution at 336nm-thick film surface obtained by 3D FDTD method.

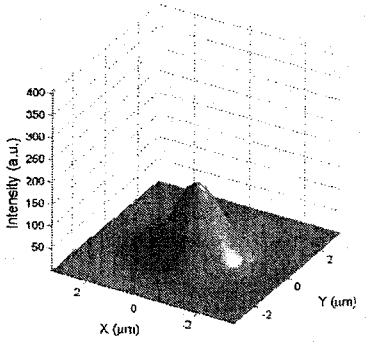

Fig. 2. Intensity distribution in a nonlinear Kerr bulk medium after propagating 336nm from the surface.

#4213 - $15.00 US
Received 20 April 2004; revised 20 May 2004; accepted 26 May 2004

Figure 3 displays the intensity distribution at the film surface after the beam from the 5.0 *mW* laser passes through films of various thicknesses, where the direction of polarization is along the vertical axis. The results show that the self-focusing effect is maximized for films of thickness $0.5\lambda_{eff}$, $1\lambda_{eff}$, $1.5\lambda_{eff}$, and $2\lambda_{eff}$. Note that the electric fields in the film can be maximized due to the nonlinear Fabry-Perot interference. As shown in Fig. 3, the near-field intensity distribution of $1.5\lambda_{eff}$ and $2\lambda_{eff}$ thick films display beam breakups into two filaments of sub-diffraction-limited spot sizes, while others do not show filamentations clearly. This strongly suggests that filamentation is dominantly determined by the condition of the nonlinear Fabry-Perot interference. In addition, we found that the film of $0.5\lambda_{eff}$ and $1\lambda_{eff}$ thickness do not generate the filamentation, indicating the existence of a threshold thickness for the filamentation.

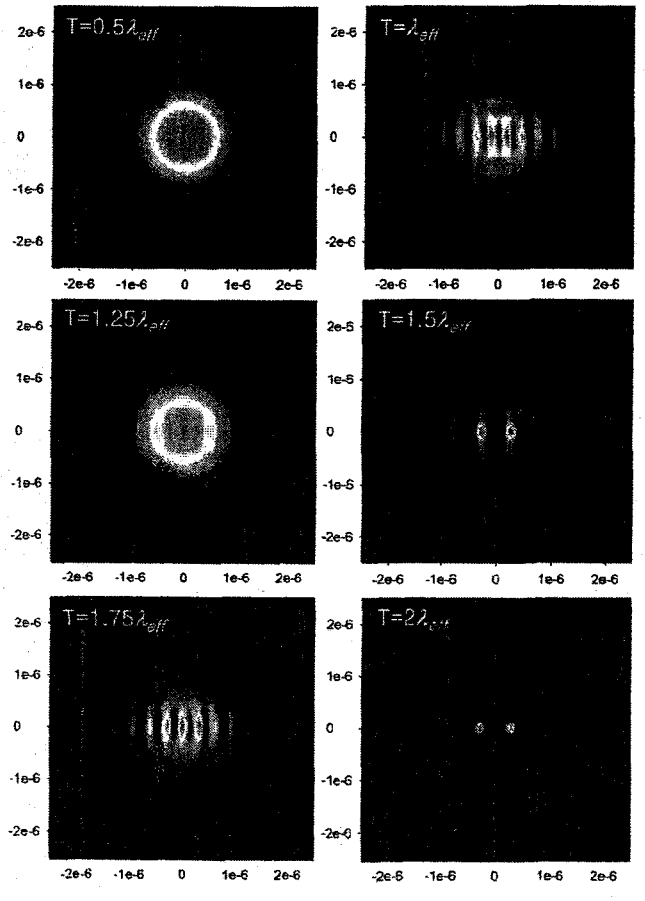

Fig. 3. Near-field intensity distribution of film with various thickness obtained by 3D FDTD method.

#4213 - $15.00 US
Received 20 April 2004; revised 20 May 2004; accepted 26 May 2004

Figure 4 displays the near-field intensity distribution of the $1.5\lambda_{eff}$ thick film for four different laser beam powers. When the beam power increases, the number of filaments due to the beam breakup dramatically grows because of the increase of the effective thickness of the film with increasing intensity. Note that the nonlinear refractive index is proportional to the incident beam power. Much more complicated multiple filamentations are produced for higher input intensities, indicating that the nonlinear Fabry-Perot resonance condition is quite sensitive to the effective film thickness.

Recently, multiple filamentation in bulk media has been known to be induced not only by random noise in the input beam but also by beam polarization [8]. Due to the gradient of the nonlinear refractive-index in the film of sub-wavelength thickness, the momentum vector of the incident beam is deflected toward the center of the Gaussian beam. The beams which are deflected to the direction parallel to the polarization of the input beam and to the direction perpendicular to the polarization have different reflection conditions. Therefore, by the oblique incidence of a linearly-polarized beam due to focusing, the polarization-dependent symmetry breaking can be occurred even when the input beam is radially symmetric.

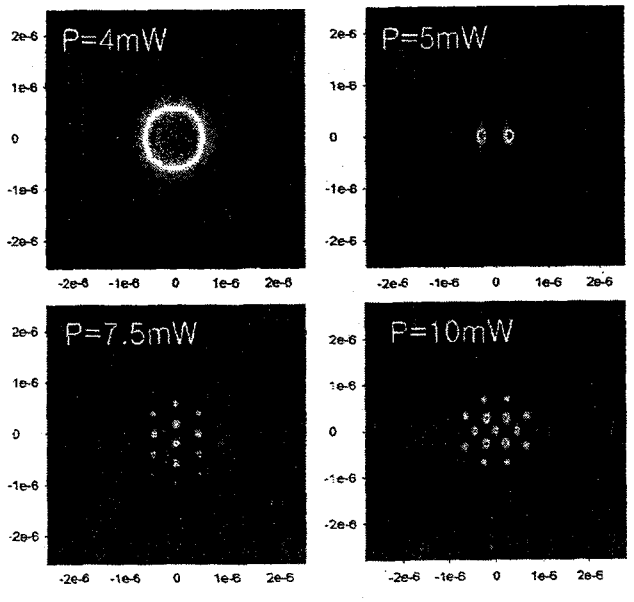

Fig. 4. Near-field intensity distribution of a nonlinear Kerr film for various beam powers obtained by 3D FDTD method.

3. Conclusion

In conclusion, we analyze the self-focusing phenomenon of nonlinear Kerr film for several configurations using the FDTD method. The temporal dynamics and the near-field intensity distributions of multiple filamentation in various film thicknesses and input beam powers are investigated theoretically. In particular, we demonstrate that linearly polarized beams can lead to multiple filamentation in nonlinear Kerr film, where filaments are narrowed below the diffraction-limit. We also find that filamentation in film is very sensitive to the nonlinear film thickness and the laser beam power, strongly indicating nonlinear Fabry-Parot interference effects on nonlinear Kerr films. Our simulations of filamentation in the nonlinear Kerr film in

#4213 - $15.00 US
Received 20 April 2004; revised 20 May 2004; accepted 26 May 2004

the near field region can be applied to optical storage and near field devices, which require a detailed intensity distribution of a sub-diffraction limited spot size.

Acknowledgments

This research was supported by the Ministry of Science and Technology through the National Research Laboratory Program (Contact No. M1-0203-00-0082).

#4213 - $15.00 US

Received 20 April 2004; revised 20 May 2004; accepted 26 May 2004

Evolution of electromagnetic interference through nano-metallic double-slit

Kyu-Min Chae, Hyun-Ho Lee, Sang-Youp Yim, and Seung-Han Park

National Research Laboratory for Nonlinear Optics, College of Science, Yonsei University, Seoul 120-749, Korea
shpark@phya.yonsei.ac.kr

http://phya.yonsei.ac.kr/~optics

Abstract: We investigated the characteristics of the near- and far-field regions of the interference for nano-metallic double-slits using a two-dimensional finite-difference time-domain (FDTD) method. We have found that the patterns in the near-field region have a phase difference of π with respect to those in the far-field region. A boundary, which separates the interference patterns of the two regions exists as a half circle and grows as the distance between the two slits increase. It is also found that evanescent waves can be enhanced and confined by coating the double-slit with a dielectric cladding.

OCIS codes: (310.6860) Thin films, optical properties; (310.1620) Coatings; (050.1220) Apertures; (260.3160) Interference; (180.3170) Interference microscopy; (180.5810) Scanning microscopy.

References and links

1. C.J. Boukamp„ "Diffraction Theory," Rep. Prog. Phys. **17**, 35 (1954).
2. M. Born and E. Wolf, *Principles of Optics*, 7th ed. (Cambridge University Press, Cambridge 1999).
3. T.W. Ebessen, H.J. Lezec, H.F. Ghaemi, and T. Thio, "Extraordinary optical transmission through sub-wavelength hole arrays," Nature **391**, 667 (1998).
4. J.A. Porto, F.J. García-Vidal, and J.B. Pendry, "Transmission Resonances on Metallic Gratings with Very Narrow Slits," Phys. Rev. Lett. **83**, 2845.(1999)
5. E. Popov, M. Nevière, S. Enoch, and R. Reinisch, "Theory of light transmission through subwavelength periodic hole arrays," Phys. Rev. B **62**, 16100 (2000).
6. L. Martín-Moreno, F.J. García-Vidal, H.J. Lezec, K.M. Pellerin, T. Thio, J.B. Pendry, and T.W. Ebbesen, "Theory of Extraordinary Optical Transmission through Subwavelength Hole Arrays," Phys. Rev. Lett. **86**, 1114 (2001)
7. Qing Cao and Philippe Lalanne, "Negative Role of Surface Plasmons in the Transmission of Metallic Gratings with Very Narrow Slits," Phys. Rev. Lett. **88**, 57403 (2002).
8. P.N Stavrinou, and L. Solymar, "The propagation of electromagnetic power through subwavelength slits in a metallic grating," Opt. Commun. **206**, 217 (2002).
9. F.I. Baida and D. Van Labeke, "Three-dimensional structures for enhanced transmission through a metallic film: Annular aperture arrays," Phys. Rev. B **67**, 155314 (2003).
10. J.M. Steele, C.E. Moran, A. Lee, C.M. Aguirre, and N.J. Halas, "Metallodielectric gratins with subwavelength slots: Optical properties," Phys. Rev. B **68**, 205103 (2003).
11. Pei-Kuen Wei, Hsieh-Li Chou, and Wun-Shain Fann, "Optical near field in nanometallic slits," Opt. Express **10**, 1418 (2002), http://www.opticsexpress.org/abstract.cfm?URI=OPEX-10-24-1418.
12. Hugo F. Schouten, Taco D. Visser, Greg Gbur, Daan Lenstra, and Hans Blok, "Creation and annihilation of phase singularities near a sub-wavelength slit," Opt. Express **11**, 371 (2003), http://www.opticsexpress.org/abstract.cfm?URI=OPEX-11-4-371.
13. Hugo.F. Schouten, Taco D. Visser, Daan Lenstra, and Hans Blok, "Light transmission through a subwavelength slit: Waveguiding and optical vortices," Phys. Rev. E **67**, 36608 (2003).
14. Y. Takakura, "Optical Resonance in a Narrow Slit in a Thick Metallic Screen," Phys. Rev. Lett. **86**, 5601 (2001).
15. C. Bainier, D. Courjon, F. Baida, and C. Girard, "Evanescent interferometry by scanning optical tunneling detection," J. Opt. Soc. Am. A **13**, 267 (1996).

#4212 - $15.00 US
(C) 2004 OSA

Received 20 April 2004; revised 11 June 2004; accepted 13 June 2004
28 June 2004 / Vol. 12, No. 13 / OPTICS EXPRESS 2870

16. L. Novotny, B. Hecht , and D. W. Pohl, "Interference of locally excited surface plsmons," J. Appl. Phys. **81**, 1798 (1997).
17. A. Taflove, S. C. Hagness, *Computational Electrodynamics: The Finite-Difference Time-Domain Method*, 2nd ed. (Artech House, Boston 2000).

1. Introduction

The analysis of light transmission through a slit with a subwavelength width in a thin plate has started in early days, dating back to Lord Rayleigh [1,2]. Recently, Ebbesen *et al.* observed extraordinary optical transmission through sub-wavelength hole arrays [3]. Because of these unexpected demonstrations, light propagations in periodic arrays of nano-slits and nano-apertures have received much attention due to their extraordinary behavior and potential applications in biologic and photonic devices [4-10]. In addition to the researches on the periodic arrays, a few studies on single nano-slit have also been performed [11-14].

To our best knowledge, however, there has not been an intensive study on the near-field properties of nano-metallic double-slit, specifically on the interference of evanescent waves in the near-field region. Considering that interference patterns of a double-slit in the far-field region is distinct from diffraction patterns of single and periodic slits, interference patterns of a double-slit in the near-field region is expected to be salient. A few authors have already studied interference of evanescent waves or surface plasmons. Bainier *et al.* reported the interaction of an evanescent standing wave with nanometer-sized objects [15] and Novotny *et al.* investigated surface plasmon interactions on a finite silver layer [16]. However, the interference of evanescent waves in nano-metallic double-slit has not been reported. In this letter, therefore, we present the characteristics of nano-metallic double-slit in near- and far-field regions using two-dimensional finite-difference time-domain (FDTD) method. With this analysis, we have distinguished several differences between the two interference patterns of nano-metallic double-slit in the near- and far-field region. We believe that the differences originate from the fact that evanescent waves are dominant in the near-field region whereas propagating waves are dominant in the far-field region.

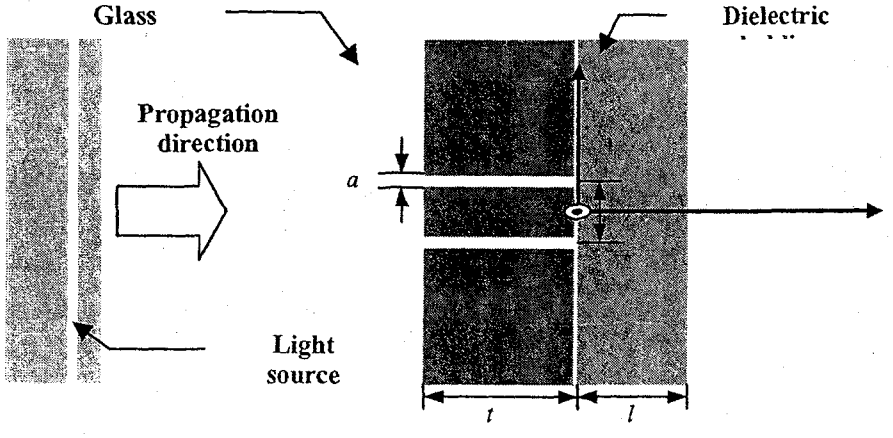

Fig. 1. Schematics of modeled space of a nano-metallic double-slit. Soft source is used for the illumination.

Figure 1 shows the modeled space of a nano-metallic double-slit. The PEC in the figure describes a material whose electric conductivity is infinite, where the initials stand for the perfect electric conductor, i.e., a perfect metal. The nano-metallic slit is assumed to be

#4212 - $15.00 US
Received 20 April 2004; revised 11 June 2004; accepted 13 June 2004

composed of perfect metal and illuminated by a Gaussian beam of λ = 500 nm. Perfect metal means that both skin depth and the amplitude of electric field are zero at the metal surface. In addition to the analysis of nano-metallic double-slit with no cladding, the slit with a dielectric cladding was also analyzed to assure the possibility that evanescent waves can be enhanced and confined with the dielectric cladding. Besides, numerous simulations were performed varying the distance between the two slits, the slit thickness, and the thickness of the dielectric cladding, i.e., the values of *d*, *t*, *l*. It is assumed that the width of both slits, *i.e.*, the value of *a*, is 50 nm and the refractive index of the glass substrate and the dielectric cladding is 1.5. The origin of the modeled space is the center of the double-slit on the line just one sampling point right from the metal/air interface, as shown in Fig. 1.

2. Field distribution due to polarization direction

When both the structure to be modeled and the incident wave are uniform in the z-direction, we can split Maxwell's curl equations into two groups. One group consists of only H_x, H_y, and E_z, and the other only E_x, E_y, and H_z. The field components of the first group are called transverse-magnetic modes with respect to z (TM_z) in two dimensions and the other transverse electric modes with respect to z (TE_z) [17]. We can notice that the polarization of incident light in the TM_z mode is normal to the plane, *i.e.*, x-y plane and that the TE_z mode is parallel to the plane. With the assumption of uniformity in the z-direction, therefore, we can calculate the near- and far-field properties of nano-metallic double-slits using two-dimensional FDTD simulation for two polarization directions. There are a few differences between the TM_z modes and the TE_z modes for the different polarization direction. The first is the difference of transmission. For the TM_z modes, because electric field is tangential to the metal surface in the slit, light cannot transmit through the slit unless the slit is thin enough. Therefore, transmission decreases exponentially as the thickness of the slit increases. For TE_z modes, however, high transmission can be acquired since light can be guided well by metal-slits.

Another difference is the position and shape of the peak at the exits of the two slits, as shown in Fig. 2, which shows the intensity distribution in the region after the slit/air interface for the TM_z and TE_z modes. In the result for the TM_z mode, light is confined to the middle of the slit since the amplitude of electric field is diminished to approximately zero in the region near the metal surface. For the TE_z mode, however, we can see that two sharp peaks appear at the edges of slits. This is due to the fact that light propagates via metal surface at the edges, and not between the slits. This result is consistent with the result of Wei *et al.* [11].

In Figs. 2(c) and (d), we can see that the double-slit forms interference fringes in the near-field region as well as in the far-field region and the interval between fringe maxima is half of wavelength as expected. The interference pattern is also different for the two modes. Interestingly, in the near-field region, interference patterns of TE_z modes seem to have a phase difference of π with respect to that in far-field region. We can easily discern the phase difference from the different line profiles of Fig. 2(d). The dashed line, i.e., the intensity profile in the near-field region, reaches a valley at the center while the intensity of the far-field reaches a peak at that point. From the difference, we can say that the two interference patterns in near- and far-field regions have phase difference of π for TE_z modes. In addition, the intensity variation of the near-field interference pattern is greater than that of the far-field interference pattern. In contrast to TE_z modes, it is hard to find any distinct difference between near- and far-field interference patterns for TM_z modes. Actually, it is even difficult to identify near-field interference for TM_z modes. From these results, we can conclude that the interference patterns of TE_z modes change their characteristics as light propagates from the near-field region to the far-field region. The differences of the interference patterns in near- and far-field regions will be further discussed in the next section. Since, the distinction appears only for TE_z modes, we will discuss the results of TE_z modes simulation from now on.

#4212 - $15.00 US
Received 20 April 2004; revised 11 June 2004; accepted 13 June 2004

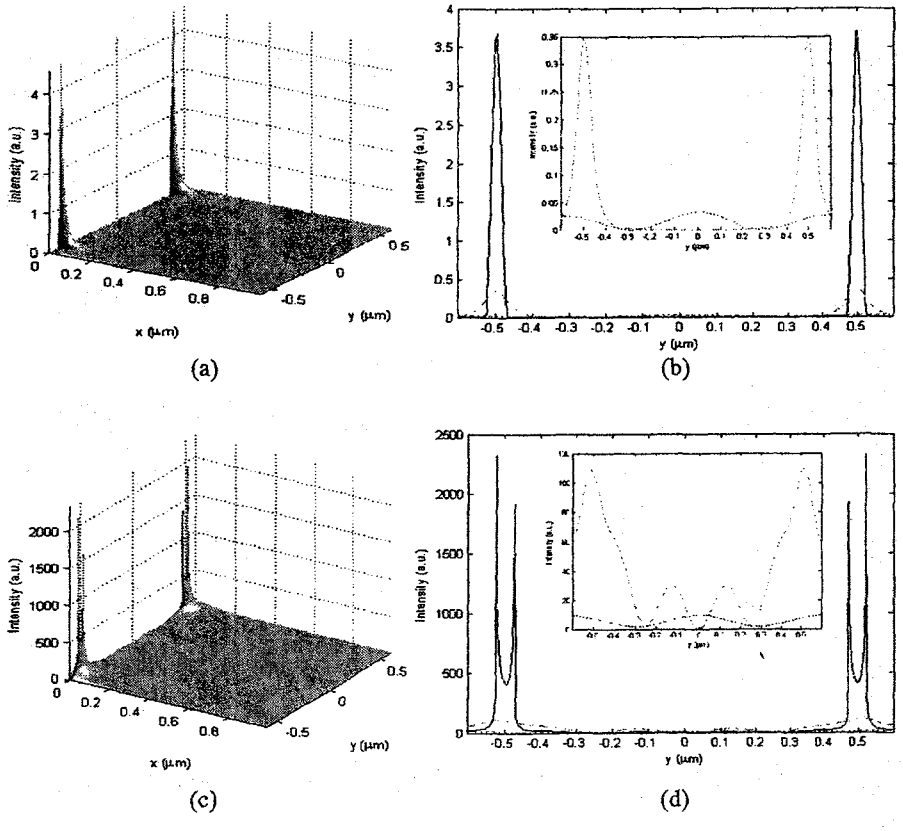

Fig. 2. Intensity distribution of the two-dimensional simulation when the slit width is a = 50nm and slit thickness is $t \approx 20$ nm. (a) Shaded display of TM_z mode intensity distribution when the distance between two slits; d = 1μm. (b) Line profile of (a). (c) Shaded display of TE_z mode intensity distribution when the distance between two slits is d = 1μm. (d) Line profile of (c). Solid line represents the line profile just above the metal/air interface, dashed line is the line profile of x = 50 nm, and dotted line represents the line profile of x = 1μm. The insets of (b) and (d) are the magnifications of dotted and dashed line profiles.

3. Interference of nano-metallic double-slits in near- and far-field regions

In the far-field region, propagating waves generate interference patterns. In the near-field region, however, interference patterns are principally shaped by evanescent waves since evanescent waves are stronger than propagating waves in near-field region. Therefore, interference patterns may have different characteristics from that of the far-field region. Figure 3 shows other displays for the results of Figs. 2(c) and (d), featuring the differences between two interference patterns in near- and far-field regions. As expected, in the far-field region, constructive interference occurs at the line of y = 0, which is illustrated in Fig. 3(d). In contrast to the interference pattern of the far-field region, that of the near-field region is destructive at the points of equal distance from two slits. As pointed out above, we believe that the difference is originated from the fact that the evanescent wave, appearing as an electric field normal to the metal/air interface, is dominant in the near-field region and out of phase at the exits of two slits whereas the propagating wave is dominant in the far-field region and in phase at the exits.

#4212 - $15.00 US
Received 20 April 2004; revised 11 June 2004; accepted 13 June 2004

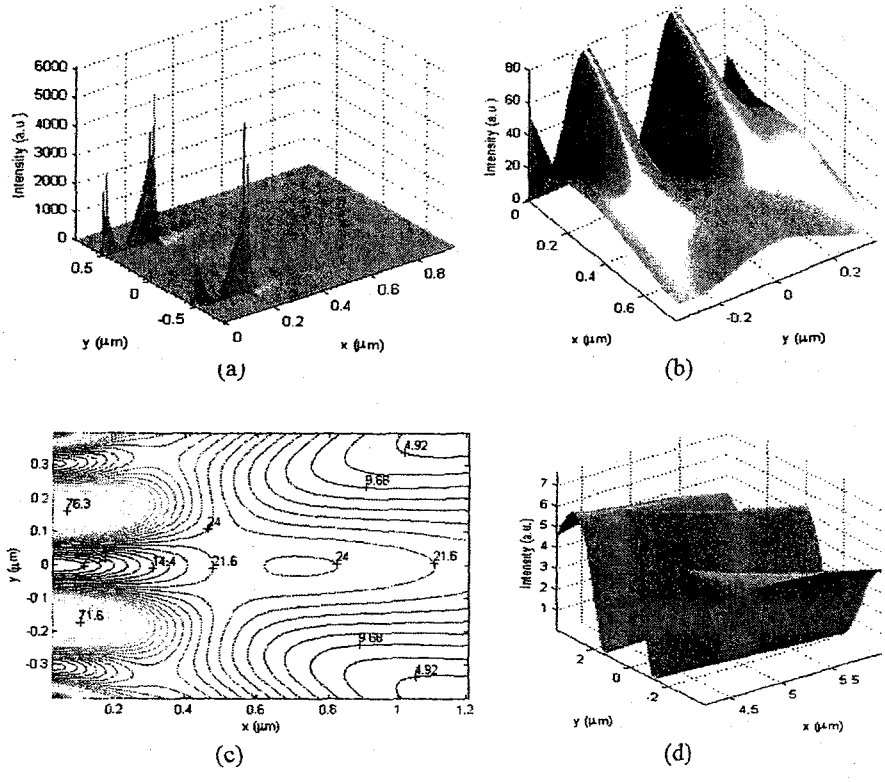

Fig. 3. Interference patterns in near-field and far-field regions when d = 1μm and λ = 620 nm: (a) Intensity distribution from the entrance of the two slits, (b) Magnified intensity distribution of the region between the two slits after the metal/air interface, (c) contour display of (b), (d) far-field interference pattern.

Because both waves in the near- and far-field regions emanate from the same slits, it seems to be inconsistent with the fact that the electric field at the exits of the two slits is out-of-phase in one region, while they are in phase in another. However, considering the superposition principle of electromagnetic waves and the fact that evanescent waves do not propagate to the far-field region, this paradox can be easily explained. If there are mixtures of two modes at the exits of double-slit, one corresponding to the evanescent wave, having phase difference at the exits of slits and appearing as an x component of the electric field, and the other a propagating wave with no phase difference, appearing as a y component, the difference between near- and far-field interferences will arise.

Figure 4 confirms this explanation. The x component of the electric field distribution at the slit edges appears anti-symmetric about the center of the double-slit whereas the y component is symmetric. Evanescent waves are assumed to be induced by E_x, the x-component of the electric field, at the slit exits since the x-axis is normal to the metal/air interface, and the propagating waves have the same polarization direction at the exit of slit as the incident waves, i.e., the direction of y-axis. We think that the phase difference originates from the fact that charge oscillations in the region between the two slits give opposite effects to each slit. Considering the differences between interference patterns in both regions, it is legitimate to say that the interference patterns evolve from the near-field region, where

#4212 - $15.00 US
Received 20 April 2004; revised 11 June 2004; accepted 13 June 2004

destructive interference occurs at the places where distances from the two slits are equal, to the far-field region, where constructive interference occurs.

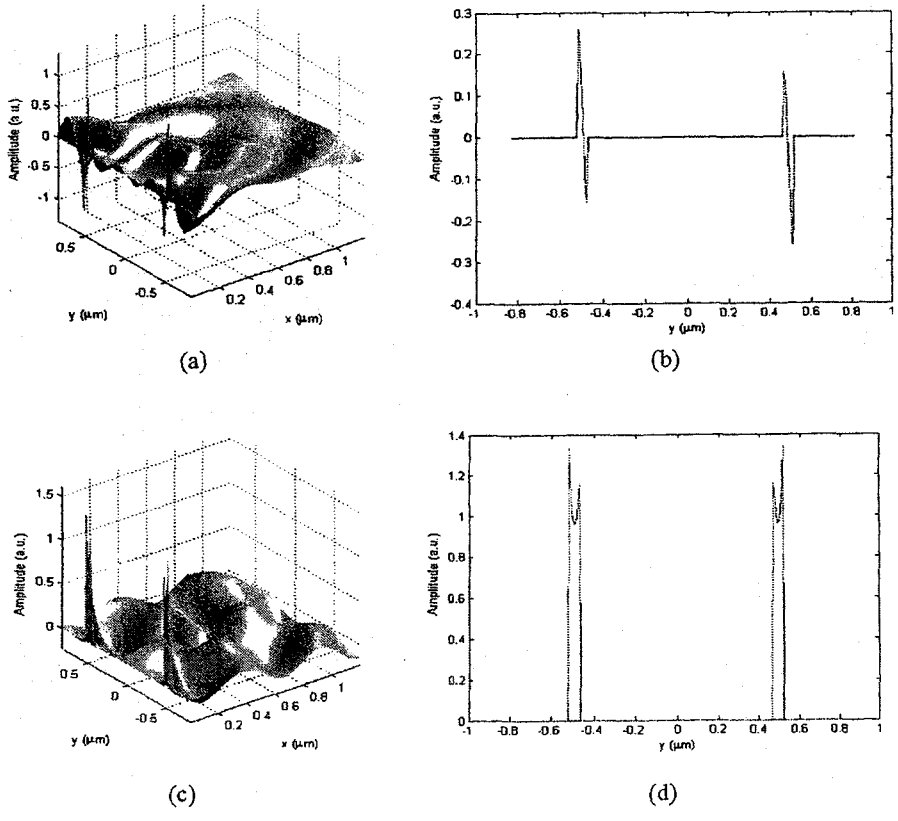

Fig. 4. Electric field distribution when $d = 1\mu m$ and $t = 200$ nm: (a) amplitude distribution of E_x (x component of electric field), (b) line profile of (a) at the metal/air interface, (c) E_y distribution, and (d) line profile of (c).

In the case of a nano-metallic single-slit, the intensity distribution decays exponentially in the lateral direction as well as the longitudinal direction as light propagates. In a nano-metallic double-slit, however, the intensity distribution in the region between the two slits appears as standing waves. It is also found that the interval of nodes is half of the wavelength λ. We suppose that the intensified standing wave in the region between the two slits is also obtained with the help of evanescent waves, whose intensity in the near-field region is much greater than that of propagating waves in the far-field region.

The interference pattern varies as the distance d between two slits increases. Figure 5 shows the results of simulation with various values of d. When $d < \lambda$, the interference fringe in the near- and far-field regions is not clear. As d grows to be greater than λ, clear interference patterns emerge. Considering that two point sources cannot be easily identified as two separate light sources when the distance between them is smaller than a wavelength, this phenomenon may be easily explained. Since the two slits act as a single light source at the far-field region, no interference pattern is constructed in that region. Similarly, it is hard to

#4212 - $15.00 US
Received 20 April 2004; revised 11 June 2004; accepted 13 June 2004

observe clear fringes in the near-field region because two or more distinct sources are required to shape clear fringes. It would be better to explain the phenomenon with diffraction when $d < \lambda$ as follows.

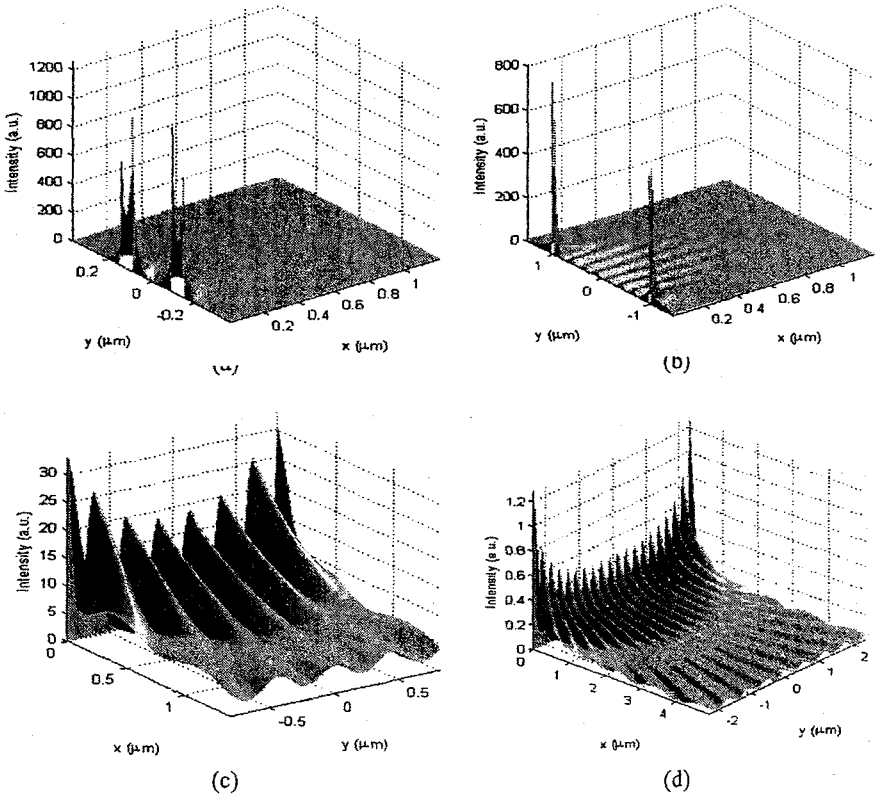

Fig. 5. Intensity distribution with various distances between two slits: (a) d = 250 nm, (b) d = 2 μm, (c) magnified display of the region between two slits when d = 2 μm, and (d) magnified display of the region between two slits when d = 5 μm.

Because near-field interference patterns have phase differences of π from far-field interference patterns, there should be a boundary that separates the interference patterns of the near-field region from that of the far-field region. In Figs. 5(c) and (d), we can easily discern the boundary circle that separates the two interference patterns. We can also see that the radius of the circle increases linearly as the distance between two slits increase. Specifically, the distance from the center of the double slit to the boundary circle equals to a half of the distance d between the two slits. Because light decays as it propagates along the metal/air interface in real metal, the assumption of perfect metal is necessary for these ideal results. However, we expect that the difference between interference patterns in both regions will affect the field distribution in the case of real metals.

We can shift the near-field interference pattern as well as the far-field interference pattern by filling the slits with different dielectric materials. For example, a constructive interference pattern will be obtained at the center of the double-slit when the slit thickness is half of the wavelength and one of the slits is filled with Si_3N_4 whose refractive index is 2. Figures 6(a)

#4212 - $15.00 US
Received 20 April 2004; revised 11 June 2004; accepted 13 June 2004

and (b) show examples of constructive interference. Figures 6(c) and (d) illustrate other results corresponding to interference of three slits and interference between slits of different widths, respectively. With the simulation where three slits are employed, we can see that each of the two pairs of slits show independent and identical interference patterns, which is equivalent to that of the double-slit. The intensity difference of the peaks originates from the employment of a Gaussian beam for the illumination. From Fig. 6(d), we can verify that the destructive interference occurs at the center of the double-slit in spite of the different widths.

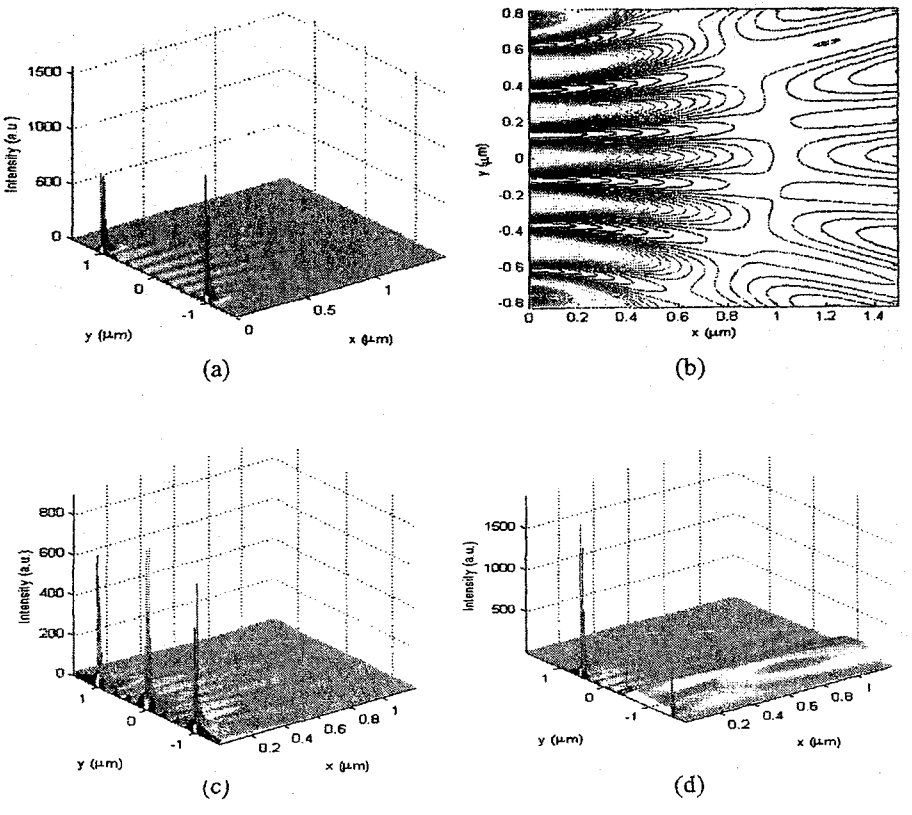

Fig. 6. Interference patterns with various conditions are presented. (a) and (b) correspond to the results when one of the slits is filled with silicon nitride (n = 2) to introduce phase difference resulting in a phase shift of π. (c) Interference pattern with three slits. (d) Interference between slits of different widths.

4. Evanescent wave enhancement by dielectric cladding

If a dielectric cladding is added to the double slit, more evanescent waves will be guided along the cladding/metal interface. Figure 7 shows interference patterns generated by the nano-metallic double-slit with a dielectric cladding of refractive index 1.5. Comparing Figs. 5(c) and 7(b), we can easily verify the enhancement of evanescent waves. In addition, evanescent waves decay more rapidly along the x-axis direction. In other words, evanescent waves are confined more effectively to the cladding/air interface.

#4212 - $15.00 US
Received 20 April 2004; revised 11 June 2004; accepted 13 June 2004

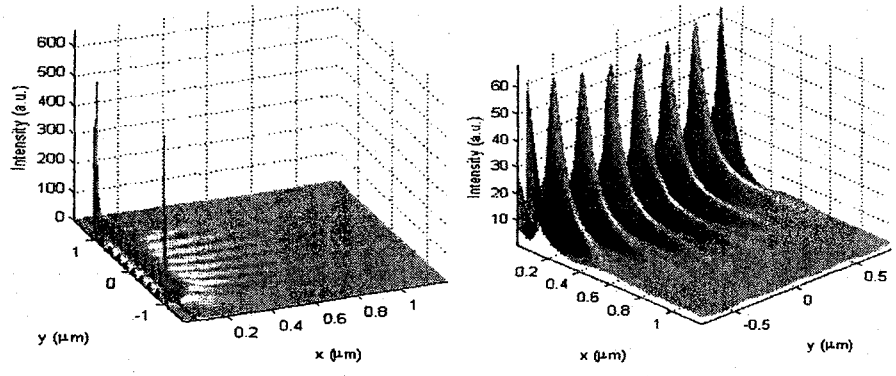

(a) (b)

Fig. 7. Intensity distribution with various slit intervals for a cladding thickness of 50 nm: (a) $d = 2$ μm, (b) magnified display of the region between the two slits.

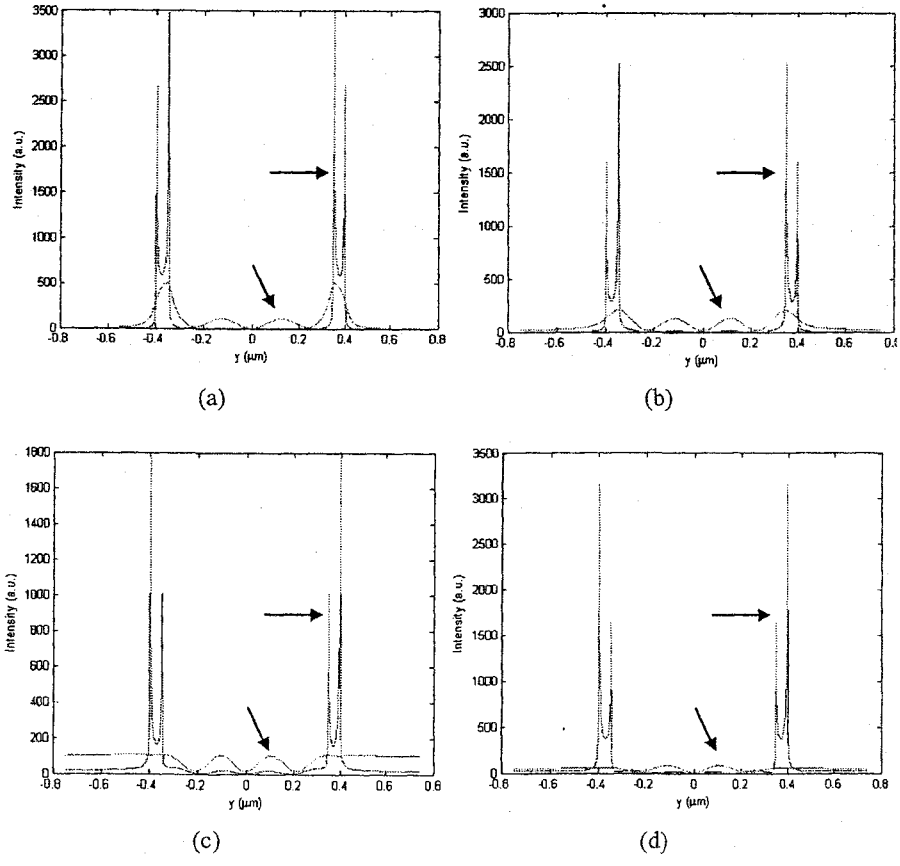

Fig. 8. Line profiles of the intensity distribution along the y direction when (a) $l = 20$ nm, (b) $l = 50$ nm, (c) $l = 100$ nm, and (d) $l = 200$ nm.

#4212 - $15.00 US
Received 20 April 2004; revised 11 June 2004; accepted 13 June 2004

Figure 8 shows the intensity distributions with various cladding thicknesses l when the distance d between the two slits is 750 nm. The line profiles are obtained at the planes a few nano-meters apart from the cladding/air interface because the height of line profile reaches its peak at that position. In comparison with the case with no cladding, the interval between the nodes of the standing wave decreases due to the increase of the refractive index. We can also see that the intensity distribution at the cladding/air interface varies as the cladding thickness is changed. When the cladding is too thin, little enhancement occurs. However, as the cladding thickness l increases, evanescent waves in the region between two slits grow stronger while those outside this region decay exponentially identical to the case of no cladding. The enhancement of the evanescent waves in this region continues until l is approximately 50 nm. As l grows to be greater than 50 nm, the intensity distribution in the outer regions between the slits becomes stronger. When l is 100 nm, the height of the intensity distribution in the outside regions equals to that in the region between the two slits, as shown in Fig. 5(c). The intensity distribution reduces as the slit thickness grows to be greater than 100 nm. With the results of the simulations, we found that the intensity distribution in the region between the two slits is maximally enhanced when l is approximately 50 nm, and approximately 100 nm for the case of the outside region.

It can also be noticed that the interval between the nodes of the standing wave decreases slightly as the thickness increases. Since the cladding can be considered as a waveguide, we suppose that the change of the dominant spatial mode leads to the variation of the interval between nodes. In other words, we suppose that waves propagate along the direction which is more inclined to the x-axis as the cladding grows thicker.

5. Conclusion

The characteristics of nano-metallic double-slits, assuming a perfect metal, in both near and far-field regions were analyzed. With the finite-difference time-domain (FDTD) simulation of a nano-metallic double-slit, we can see that the interference patterns in the near-field region have many characteristics different from those in the far-field region. Specifically, the interference patterns in both regions have a phase difference of π with respect to each other. In addition, a boundary separating the near-field interference from the far-field interference appears as a half circle, whose radius is half of the distance between the two slits. We think that this difference originates from the fact that the near-field interference is determined by evanescent waves whereas in the far-field propagating waves are dominant. We also show that filling the slits with different dielectric materials can shift fringes in the near-field region as well as the far-field region. In addition, simulations for three slits and double slits of different widths are also performed.

It is also found that when a dielectric cladding is added to the double-slit, evanescent waves are enhanced and confined more effectively to the cladding/air interface. As the cladding grows thicker, the intensity distribution varies as in the following orders. 1) Intensity in the region between two slits increases. 2) Light easily propagates laterally through the cladding and the light intensity propagating to the outer region of the two slits becomes equal to that of the region between the two slits. 3) Light propagation to the outside region becomes weaker. We think that a resonator of evanescent waves can be constructed by placing a pair of reflectors using the fact that light easily propagates laterally along the metal/cladding interface.

Acknowledgments

This research was supported by the Ministry of Science and Technology through the National Research Laboratory Program (Contact No. M1-0203-00-0082).

#4212 - $15.00 US
Received 20 April 2004; revised 11 June 2004; accepted 13 June 2004

Numerical analysis of an annular-aperture solid immersion lens

Cheng Liu and Seung-Han Park

National Research Laboratory of Nonlinear Optics, Yonsei University, Seoul 120-749, South Korea

Received March 1, 2004

A physical model of an annular-aperture solid immersion lens (SIL) is proposed, and its attractive features are presented numerically with the finite-difference time-domain method. Placing an appropriate annular aperture in front of the SIL shows that the focal depth can evidently be improved, combining the virtues of the annular-aperture technique and the SIL technique. With this proposed method the rigorous distance control condition in related devices can be relaxed, preventing scratches or collisions between the optical head and the recording medium. Potentially, this technique could have great prospects for applications in optical data recording, lithography, and other applications that depend on immersion media to meet the resolution criteria across the image field. © 2004 Optical Society of America

OCIS codes: 220.2560, 210.4770, 000.4430, 120.3180, 050.1940.

The demand for higher-data-capacity storage grows continuously, and in the case of optical data storage this demand is met by a reduction of the optical beam spot size. As an approach to minimizing the spot size, an aplanatic sphere known as a solid immersion lens (SIL), used in photon-tunneling microscopy[1] and optical data storage,[2] was developed to increase the resolution and areal density by means of increasing the numerical aperture (N.A.) above the theoretical upper limit of 1 obtained in air. In comparison with the near-field microscopic recording technique,[3] this method provides not only a satisfactory resolution but also a high optical efficiency and data rate. However, the reduced focal spot of a SIL exists only in close proximity to the SIL–air interface. Thus, to achieve high-density data storage with a SIL, the recording medium must be placed much less than 100 nm from the base of the SIL interface. However, it is difficult to maintain the distance between the SIL and the recording medium when they are so close since both the optical head and the recording medium can be easily damaged by scratches or collisions. This is the main reason that application of a SIL in data storage devices lacks practicality.

It is well known that the intensity distribution of the focal spot of a lens can be optimized by an annular aperture in the pupil plane.[4,5] However, a SIL is essentially an aplanatic immersion element rather than a conventional lens, having its focal spot in the near-field region of the SIL–air interface, where both the propagating wave and the evanescent wave contribute to the focused light. This makes an annular aperture SIL much more complicated than a conventional annular-aperture lens, and almost all the existing theories are not valid for its analysis. Only a few analyses of the effect of an annular aperture on a SIL have been reported so far to our knowledge. Tien *et al.*[6] discussed how the readout-signal contrast decreases while the distance between the SIL and the surface of the medium increases, when the incident rays below the critical total internal reflection angle are all blocked by a circular screen. Milster *et al.*[7] showed that the readout-signal contrast can be improved by placing a pupil filter in front of the SIL. Contrary to these previous works, in this Letter we show that the focal depth of a SIL can be improved by optimizing the interference between the propagating waves and the evanescent waves with an appropriate annular aperture in front of the SIL. With this method, in particular, we show that the distribution of the focused light is almost unchanged along a certain distance range in air, relaxing the need for rigorous distance control to make the SIL technique much more favorable for practical applications.

In our physical model an annular-aperture mask is placed in front of an objective lens as shown in Fig. 1(a). The beam spot profile in the near-field region of the SIL–air interface is numerically studied by combining the vector diffraction method and the three-dimensional (3D) finite-difference time-domain (FDTD) method.[8] It is assumed that the linearly polarized light with a wavelength of 650 nm is focused by an objective lens onto a SIL, where the electric field is polarized in the x direction. The SIL is hemispherical in shape, and its plane surface is placed at $z = 0$, as displayed in Fig. 1(a). The plane surface of the SIL is coated with a perfectly conducting metal film, and an aperture with a diameter of D is located in the center of the metal film. It is also assumed that the N.A. of the objective lens is 0.65 and the diffraction index of the SIL is 2.0. For the 3D FDTD

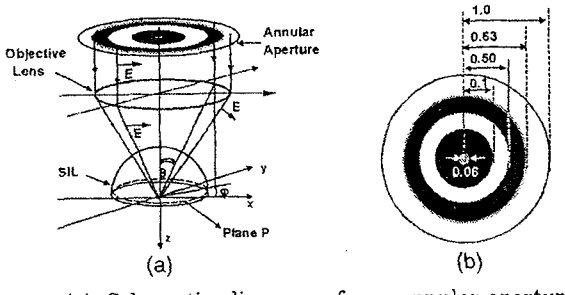

Fig. 1. (a) Schematic diagram of an annular-aperture SIL. (b) Structure of the annular aperture.

0146-9592/04/151742-03$15.00/0

simulation the calculation of the intensity distribution of the focal spot in air is divided into two steps. In the first step we calculate the amplitude distribution of the incident light in a plane just above the SIL–air interface by computing the 3D vector diffraction integral. Then the obtained amplitude distribution is used as the incident wave for calculation of the intensity distribution in the near-field region of the SIL–air interface with the 3D FDTD method.

Because of the high N.A. (= 0.65) of the optical head, the scalar diffraction theory is not valid, and hence a 3D electromagnetic calculation is required. The incident aberration-free focused electric field **E** can be expressed as[9]

$$E = C\int_0^{\theta_t}\int_0^{2\pi}(\xi,\eta,\zeta)f_0(\theta,\phi)(\cos\theta)^{1/2} \times \exp[jk_1(s^x x + s^y y + s^z z)]\sin\theta\,\mathrm{d}\theta\,\mathrm{d}\phi, \quad (1)$$

where C is a constant, θ_t is the maximum incident angle, $f_0(\theta,\phi)$ is the pupil function of the annular-aperture mask,

$$s^x = \sin\theta\cos\phi, \qquad s^y = \sin\theta\sin\phi, \qquad s^z = \cos\phi, \quad (2)$$

and (ξ,η,ζ) are the vector components of the electric field as follows[10]:

$$\xi = [\cos\theta + \sin^2\phi(1-\cos\theta)],$$
$$\eta = (\cos\theta - 1)\sin\phi\cos\phi,$$
$$\zeta = -\sin\phi\cos\phi. \quad (3)$$

The structure of the annular-aperture mask is shown in Fig. 1(b), in which the two black rings are the opaque regions of the annular aperture, and the central region introduces a phase retardation of $-\pi$. The calculated amplitude distribution in plane P (300 nm above the plane surface) is used as the incident wave to calculate the intensity distribution in the near-field region of the SIL–air interface with the 3D FDTD method. The FDTD simulation space is divided into 120 × 120 × 150 cells. Each cell has a volume of Δx, Δy, and Δz, where Δx, Δy, and Δz are each 30 nm. In dealing with the sharp change in the electromagnetic parameters at the interface, an average value must be taken for the materials at both sides of the interface.

Figure 2 shows the steady-state field distribution of both the conventional SIL and an annular-aperture SIL in the xz section. Figure 2(a) is the field distribution of the annular-aperture SIL. In comparison with Fig. 2(b), in which the intensity distribution of the common SIL is shown, the field distribution in Fig. 2(a) shows a tiny peak that could be employed as a virtual probe for data storage. Note that the focal depth of the annular aperture is considerably longer than that of the conventional SIL, and there is almost no increase in the transverse width.

Figure 3(a) shows the normalized intensity distributions of the central peak of Fig. 2(a) at different distances from the SIL–air interface. For comparison, the intensity distribution of the central peak of a common SIL at a plane 50 nm from the interface is also shown in Fig. 3(a) as a solid curve. Figure 3(b) displays the FWHMs of the central peak of the common SIL and the annular-aperture SIL as a dashed curve and solid curve, respectively. It is found that the FWHM of our annular-aperture SIL remains almost constant at ~300 nm in the range 0–1000 nm from the interface. On the other hand, the FWHM of the central peak of a common SIL increases rapidly with the distance from the interface.

Figure 4(a) shows the intensity distributions of the central peaks of a common SIL and our annular-aperture SIL versus distance from the interface along the z axis with a dotted curve and a dashed curve, respectively. It is found that the intensity of an annular-aperture SIL is still much stronger than that of a common SIL in the range from 150 to 1000 nm, even though some of the light is blocked by the annular aperture (see Fig. 1). Therefore the annular-aperture technique not only enhances the focal depth of the SIL but also strengthens the intensity of the focal spot.

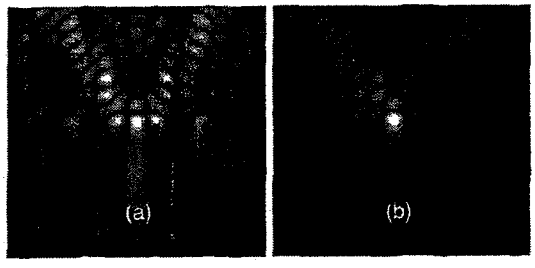

Fig. 2. Intensity distributions in the xz plane of (a) an annular-aperture SIL and (b) a conventional SIL.

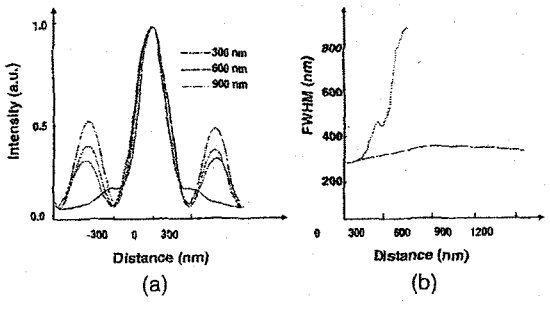

Fig. 3. (a) Intensity distributions at different distances from the SIL–air interface. (b) FWHM of the central peak versus distance from the SIL–air interface.

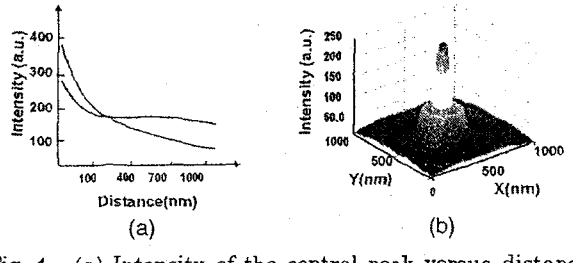

Fig. 4. (a) Intensity of the central peak versus distance from the SIL–air interface. (b) Intensity distribution at a plane 700 nm from the SIL–air interface.

For practical optical data devices this can provide a relaxed distance control condition and an improved optical efficiency and data rate. The intensity distribution of the central peak of the annular-aperture SIL in the xy plane at a distance of 700 nm from the interface is shown in Fig. 4(b). The FWHM of the central peak is approximately 0.48λ, and the intensity of the sidelobes is much smaller than that of the central peak. This indicates that the distribution of the focal spot can also be suitable for practical data storage at this distance.

In our numerical calculations the incident field in plane P of Fig. 1(a) does not include the error, since Eq. (1) is a rigorous equation without any approximations. In the second step of the FDTD simulation the error is considered to be dependent on the size of each cell in the simulation space and the time interval. In our calculation the size of the cell is only approximately 1/22 of a wavelength, and the time interval is approximately $T/110$ (T is the time period of the light). According to related FDTD theory,[11] the error in our calculation is estimated to be much less than 2%.

Generally speaking, Eq. (1) is not valid for a practical SIL because of the diffraction of the incident light on its imperfect surface. But if the deviation of a practical SIL surface from its ideal surface is much smaller than the wavelength, Eq. (1) is still valid under the Kirchhoff approximation. In this case the $f_0(\theta, \phi)$ in Eq. (1) must be replaced by

$$f(\theta, \phi) = f_0(\theta, \phi) f'(\theta, \phi), \tag{4}$$

where $f'(\theta, \phi) = \exp\{i2\pi[d(\theta, \phi)/\lambda]\}$ and $d(\theta, \phi)$ is the deviation of the practical radius of the SIL from the theoretical radius. Then Eq. (1) can be rewritten as

$$E' = C \int_0^{\theta_t} \int_0^{2\pi} (\xi, \eta, \zeta) f_0(\theta, \phi) (\cos\theta)^{1/2} f'(\theta, \phi) \times \exp[jk_1(s^x x + s^y y + s^z z)] \sin\theta \mathrm{d}\theta \mathrm{d}\phi. \tag{5}$$

This can be transformed as

$$E' = C \int_0^{\theta_t} \int_0^{2\pi} (\xi, \eta, \zeta) f_0(\theta, \phi) \cos(\theta)^{1/2} \times \exp[jk_1(s^x x + s^y y + s^z z)] \sin\theta \mathrm{d}\theta \mathrm{d}\phi \otimes \int_0^{\theta_t} \int_0^{2\pi} f'(\theta, \phi) \exp[jk_1(s^x x + s^y y + s^z z)] \times \sin\theta \mathrm{d}\theta \mathrm{d}\phi = E \otimes E^{\mathrm{error}}, \tag{6}$$

where $\otimes$ is the convolution operator. In Eq. (6) field $\mathbf{E}'$ (of the imperfect SIL) is the convolution between field $\mathbf{E}$ (of the ideal SIL) and error field $\mathbf{E}^{\mathrm{error}}$. However, it has been demonstrated above that the conventional ideal SIL and the annular-aperture ideal SIL have almost the same transverse distribution widths (see Figs. 2 and 3). Hence, according to convolution theory, it can be concluded from Eq. (6) that the annular aperture does not increase the sensitivity of the focused spot diameter when defects exist on the SIL surface.

In summary, a physical model of an annular-aperture SIL has been proposed to increase the focal depth of a SIL in air. In this technique the resolution is enhanced by the high-index SIL, and the depth of focus is enhanced by the annular aperture. With this method the FWHM of the central peak of the focal spot remains constant regardless of distance from the interface within a certain range. The prolonged focal spot also has a stronger intensity distribution than that of a common SIL. Thus the annular-aperture SIL can relax the rigorous distance control condition as well as improve its optical efficiency and data rate for related optical devices. The results amply demonstrate that this technique can be applied for fields in optical storage, nanolithography, and optical manipulation.

This research was supported by the Ministry of Science and Technology through the National Research Laboratory Program (contract M1-0203-00-0082). L. Cheng's e-mail address is liucheng@phya.yonsei.ac.kr.

References

1. S. M. Mansfied and G. S. Kino, Appl. Phys. Lett. **57,** 2615 (1990).
2. B. D. Terris, H. J. Mamin, D. Rugar, W. R. Studenmund, and G. S. Kino, Appl. Phys. Lett. **65,** 388 (1994).
3. E. Betzig, J. K. Trauman, R. Wolfe, E. M. Gyorgy, and O. L. Finn, Appl. Phys. Lett. **61,** 142 (1992).
4. W. T. Welford, J. Opt. Soc. Am. **50,** 749 (1960).
5. H. Wang and F. Gan, Appl. Opt. **41,** 5263 (2002).
6. C. H. Tien, Y. C. Lai, and H. P. D. Shieh, Opt. Eng. **40,** 2285 (2001).
7. T. D. Milster, K. Shimura, J. S. Jo, and K. Hitora, Opt. Lett. **24,** 605 (1999).
8. K. S. Yee, IEEE Trans. Antennas Propag. **AP-14,** 302 (1966).
9. S. Y. Hasegawa, N. Aoyama, A. Futamata, and T. Uchiyama, Appl. Opt. **38,** 2297 (1999).
10. B. Richards and E. Wolf, Proc. R. Soc. London Ser. A **253,** 358 (1959).
11. P. Monk and E. Suli, IEEE Trans. Magn. **30,** 3200 (1994).

Journal of the Korean Physical Society, Vol. 45, No. 2, August 2004, pp. 455~459

Symmetric and Asymmetric Resonance Characteristics of a Tuning Fork for Shear-Force Detection

Jae-Hoon LEE, Jang-Hoon YOO, Sang-Youp YIM and Seung-Han PARK*
National Research Laboratory of Nonlinear Optics, Yonsei University, Seoul 120-749

(Received 29 April 2004)

The frequency response of a tuning fork intended for shear-force detection on a near-field scanning optical microscopy (NSOM) system has been investigated. In particular, a simplified model based on a coupled harmonic oscillator is presented to qualitatively describe the experimentally observed symmetric and asymmetric resonance behaviors of the tuning fork. We find that the elastic terms of the frequency response can produce a pinning down effect on one side of the main peak, resulting in a suppression of the background noise with a high Q-factor.

PACS numbers: 07.79.Fc, 68.37.Uv
Keywords: Tuning fork, Resonance characteristics, Q-factor, Near-field scanning optical microscopy

I. INTRODUCTION

Near-field scanning optical microscopy (NSOM) is widely utilized for scanning the optical characteristics of sub-micron structures with resolutions better than the classical diffraction limit [1–3]. The basic concept of NSOM is to observe evanescent waves generated at a miniscule aperture, where the spatial resolution of NSOM is limited by the aperture size of the probe and its distance from the sample [2]. Specifically, evanescent waves can be achieved by placing an aperture with dimensions smaller than the wavelength at distances of from the surface of the sample. A number of methods, such as electron tunneling [1], frustrated total internal reflection [4], atomic force probing [5,6], and shear-force distance control [7–10], have been reported for accurate regulation of the surface-to-sample distance in order to scan an uneven surface. Vibrating a tapered optical fiber probe using a mechanical dither and detecting the shear-force feedback signal between the probe tip and the sample through a quartz tuning fork is one of the most commonly used methods up to date [9]. When a shear-force is experienced between the tip and the sample surface, the resonance peak of the tuning fork shifts to higher frequency, resulting in a decrease in the signal amplitude [11–13]. Using this method, we can take advantage of the ability to simultaneously obtain both the shear force topological image and the near-field optical image for a given sample.

In general, the shear-force detection system of NSOM consists of a tapered fiber-tip probe with a 50 $\sim$ 200 nm aperture, a commercial quartz tuning fork with a resonance frequency of 32,768 Hz, and a dithering PZT with its resonance frequency near 40 kHz. The fiber probe is glued along one of the prongs of the tuning fork, and the opposite side is mounted onto the dithering PZT. Under such circumstances, the tuning fork and the fiber probe system is likely to have more than one vibration mode. By obtaining the frequency response of the shear-force detection system, not only around the region of resonance ($\sim$32,768 Hz) but also along a larger inclusive span (10,000 $\sim$ 50,000 Hz), we can find many more subsidiary peaks [14]. In order to get certain resonance characteristics desired for high resolution, we should consider many subtle details, such as the mounting conditions and the mounting positions of the tuning fork on the dithering PZT, as well as the shape of the dithering PZT. Under different conditions, it is common to observe many different kinds of resonance curves with different noise amplitudes, quality factors, and curve shapes. Since a resonance peak with a high quality factor, Q, and a high signal-to-noise ratio is essential for good resolution during the scanning process, it is quite important to understand the origin of these diverse frequency responses of the shear-force detection system. In this paper, we present a simplified model based on a coupled harmonic oscillator. This model can qualitatively describe the experimentally observed symmetric and asymmetric resonance behaviors of the tuning fork.

II. EXPERIMENTS

Figure 1(a) shows nearly symmetric frequency resonance curves of the tuning fork and the fiber probe sys-

*E-mail: shpark@phya.yonsei.ac.kr;
Tel: +82-2-2123-2617; Fax: +82-2-392-3374

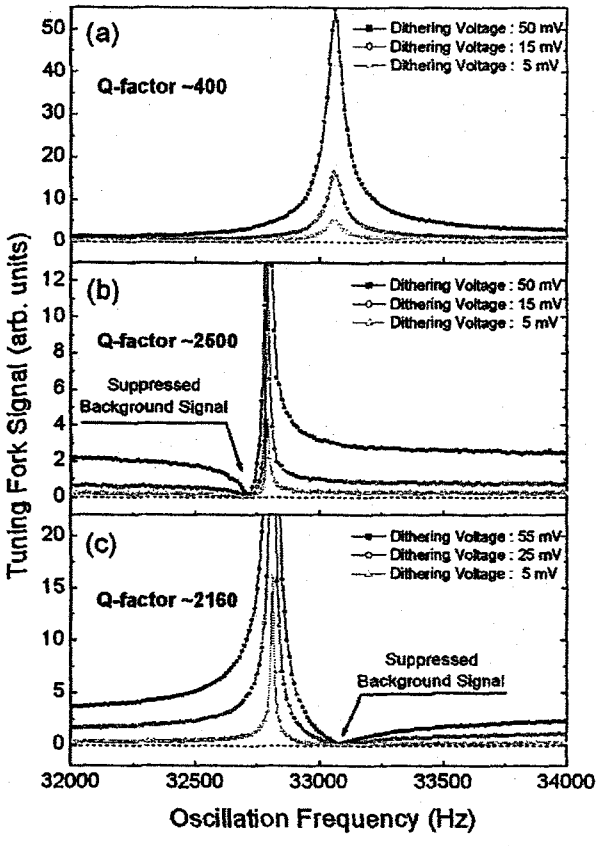

Fig. 1. Measured frequency response curves of a tuning fork for three different dithering voltages: (a) symmetric and (b) & (c) asymmetric responses. For the asymmetric responses, the background noise signal drops to nearly zero either on the low-frequency side (b) or on the high-frequency side (c) around the peak maximum.

tem. Those curves were measured at three different dithering voltages. In some cases, however, asymmetric resonance peaks having relatively steeper slopes with noise amplitudes suppressed nearly to zero at the base of one side of the peak are found. Figures 1(b) and 1(c) display the measured asymmetric frequency responses and show that the background noise signals drop to nearly zero on the low-frequency and the high-frequency sides of the peak, respectively. Note that the asymmetric frequency response curves shows higher Q-factors than the symmetric response curve.

Through these experiments, we found that two peaks were relatively larger than the other peaks, suggesting that a simplified approximation to the shear-force detection system might be a two-degree-of-freedom coupled oscillator with harmonic excitations. If the system is considered to be a two-degree-of-freedom coupled oscillator, the coupled equation of motion in matrix form can be written as

$$M\boldsymbol{x}(t) + C\boldsymbol{x}(t) + d\boldsymbol{x}(t) = \boldsymbol{F}(t) \tag{1}$$

Assuming the excitation force to be harmonic, we may express the force, the steady-state response, the effective-mass, the damping-constant, and the stiffness matrices as

$$\boldsymbol{F}(t) = \boldsymbol{F}_0 e^{i\omega t}, \quad \boldsymbol{x} = \boldsymbol{X}(i\omega)e^{i\omega t},$$
$$M = \begin{pmatrix} m_1 & 0 \\ 0 & m_2 \end{pmatrix}, \quad C = \begin{pmatrix} m_1\Gamma_1 & 0 \\ 0 & m_2\Gamma_2 \end{pmatrix},$$
$$K = \begin{pmatrix} k_1 + K & -K \\ -K & k_2 + K \end{pmatrix},$$

where $\boldsymbol{F}_0$ is a constant-amplitude vector and $\boldsymbol{X}(i\omega)$ is a complex vector that depends on the driving frequency ω. The solution of Eq. (1) can be expressed by using two resonance terms [15] :

$$X_1(i\omega) = \frac{(-\omega^2 m_2 + i\omega m_2\Gamma_2 + k_2 + K)F_1 + KF_2}{(-\omega^2 m_1 + i\omega m_1\Gamma_1 + k_1 + K)(-\omega^2 m_2 + i\omega m_2\Gamma_2 + k_2 + K) - K^2}$$
$$X_2(i\omega) = \frac{KF_1 + (-\omega^2 m_1 + i\omega m_1\Gamma_1 + k_1 + K)F_2}{(-\omega^2 m_1 + i\omega m_1\Gamma_1 + k_1 + K)(-\omega^2 m_2 + i\omega m_2\Gamma_2 + k_2 + K) - K^2} \tag{2}$$

For the observed resonance signal, we may define the superposed frequency response function as $X(iw) \equiv X_1(iw) + X_2(iw)$ and the magnitude of the frequency response as

$$|X(iw)| = [X(iw)\bar{X}(iw)]^{\frac{1}{2}}$$
$$= \{[ReX(iw)]^2 + [ImX(iw)]^2\}^{\frac{1}{2}} \tag{3}$$

Assuming the tuning fork and the fiber-probe system to vibrate in two independent directions, such as the x and y directions [16], or using any other means to produce two coupled vibration modes, we may substitute different resonance conditions, such as damping coefficients, stiffness constants, and mass values for our simplified equation. By applying suitable values, we can obtain two comparatively large peaks corresponding to the experimental results. If we substitute different values of the damping constants Γ_1 and Γ_2, while choosing an adequate coupling constant K, one of the peaks will be substantially suppressed compared to the other, which

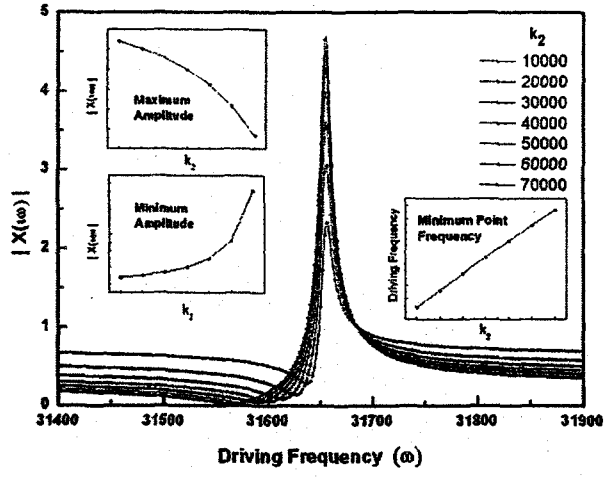

Fig. 2. Simulated results of $|X(iw)|$ *vs.* driving frequency for various values of k_2.

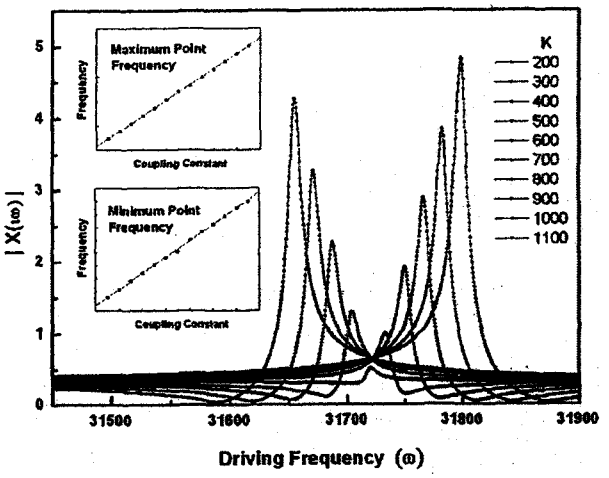

Fig. 3. Simulated results of $|X(iw)|$ *vs.* driving frequency for various values of the coupling constant K.

is the common case observed in our experiments. Thus, by selecting suitable relative positions, oscillating forces, and coupling constants of the two terms corresponding to the suppressed resonance peak and the main peak, we are able to produce special types of asymmetric resonance peaks identical to those observed.

Figure 2 shows the resonance curves for different values of k_2. Here all other variables, including k_1, are fixed to values permitting an asymmetric frequency response. As k_2 approaches k_1 = 100,000, the minimum point frequency, *i.e.*, the frequency of the point pinned down by the elastic term, moves closer to the peak maximum which is independent of k_2. The peak maximum amplitude and the minimum point amplitude also converge closer to each other while they decrease and increase, respectively. At a certain value of k_2, when k_2 is still smaller than k_1, the minimum point transfers to a higher-frequency region relative to the peak maximum, which dramatically changes the asymmetric shape of the frequency response.

Figure 3 depicts the asymmetric resonance curves for various coupling constants. The resonance curves show symmetric behaviors centered on a node at 31,721.5 Hz, which corresponds to a coupling constant, K, near 630. As K is set farther from 630, the maximum amplitude increases while the minimum decreases to nearly zero. Thus, for an asymmetric frequency response, the coupling constant should be situated in a region near the node. However if it is too close to the node the peak itself will be excessively suppressed. The region where the resonance is pinned down is also sensitive to changes in K near the node.

Figure 4 shows the resonance curves for different driving forces. F_2 was varied while F_1 was fixed at 4, and the value of was set smaller than 630. When F_2/F_1 is smaller than ~85, the minimum point is at a lower frequency relative to the peak maximum and rapidly approaches the peak maximum as F_2/F_1 approaches ~85. At this

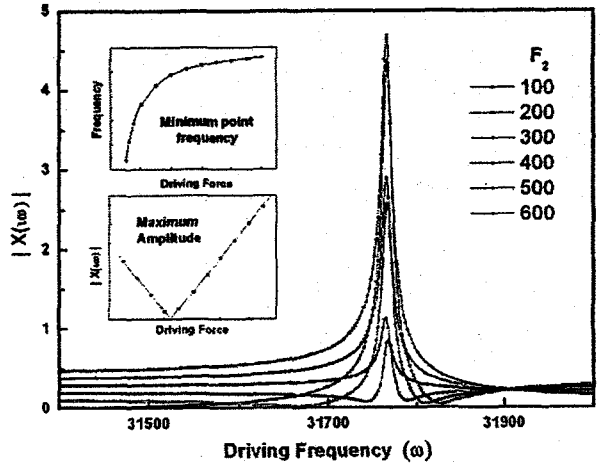

Fig. 4. Simulated results of $|X(iw)|$ *vs.* driving frequency for various values of F_2.

time, the maximum amplitude linearly decreases while the minimum amplitude slightly increases, presenting a small signal-to-background ratio when F_2/F_1 is near 85. For values of F_2/F_1 larger than 85, the minimum point transfers to a higher frequency relative to the peak maximum while the frequency of the minimum point increases very slowly, seeming to converge to about 31,800 Hz, a higher frequency relative to the peak maximum.

Figures 5(a), 5(b), and 5(c) are frequency response curves obtained from simulations using the principles discussed above. These figures mimick the experimental data of Figures 1(a), 1(b), and 1(c), respectively. Since the mounting conditions concerning the adhesive are very subtle, making it almost impossible to attempt to calculate each variable for each case, the actual values substituted in Figure 5 were chosen circumstantially in order to replicate Figure 1. A roughly symmetric response maay be acquired for the larger main peak, as in Figure

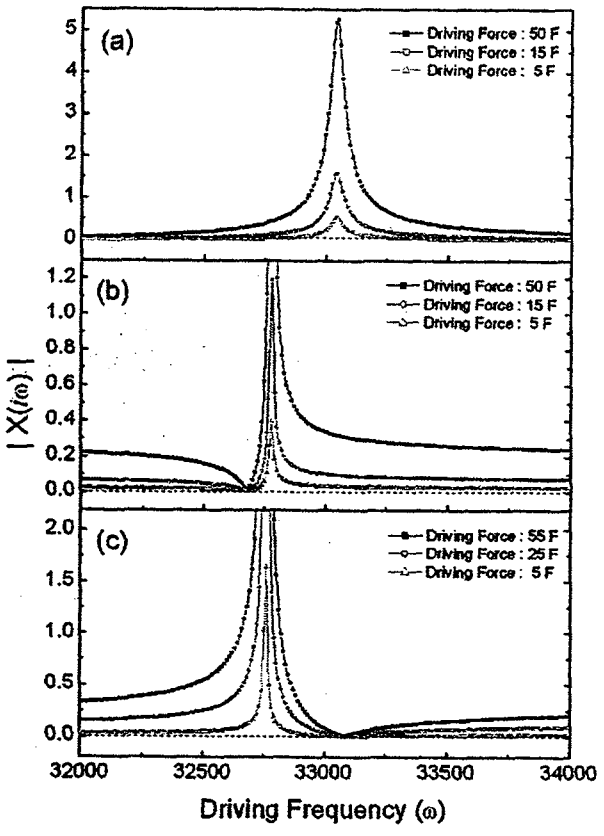

Fig. 5. (a) ~ (c) Simulated results obtained by calculating $|X(iw)|$ with Eq. (3), qualitatively matching those of Figures 1(a) ~ (c), respectively.

5(a), if the term corresponding to the smaller peak is driven by an oscillating force not large enough to have a noticeable effect on the main peak. However, if the oscillating force is substantial so as to have a noticeable influence on the main peak, we can observe a rapid drop in the resonance signal on one side of the main peak for an adequate coupling constant K. The frequency where the signal is suppressed nearly to zero is independent of the applied dithering oscillation amplitude, yielding steeper slopes for higher dithering voltages. This behavior of the amplitude is due to the elastic term of the suppressed peak, *i.e.*, Re $X_1(iw)$, supposing that $X_1(iw)$ is the suppressed term [17]. When Re $X_1(iw)$ has an ample effect on $X_2(iw)$, the main peak shows a asymmetric shape, strongly indicating that the proposed coupled two-degree-of-freedom spring-mass system serves as a good approximation to explain the different frequency response curves observed experimentally.

However, the two-dimensional model can only accurately simulate the resonance curve on a local scale. In order to simulate the frequency response for a global frequency range, we need to add many more terms. This idea is supported by the fact that as we increase the voltage applied to the dithering PZT, we are able to see many more peaks which are hidden by the background signal when higher voltages are applied, indicating the existence of additional terms. These terms come from different vibration modes of the tuning fork. One possibility is the existence of a vibration mode along the perpendicular direction of the typical vibration mode. The dithering PZT is vibrating not only along the direction normal to its surface but also along the orthogonal direction. The fact that the tuning fork is a beam, instead of a simple spring-mass system, may also be a cause since beam vibrations have many harmonic modes and nonlinearities. Any such vibration modes with large damping terms and F/m factors may contribute to a drop on one side of the main peak.

Practically, our interest is focused on the case where the asymmetric resonance peak has a better Q-factor in the lower frequency region with the noise amplitudes being greatly suppressed at its base. With such resonance curves, we have found that it is easier to obtain higher vertical and lateral resolution, which comes naturally with high Q-factors. We have tried to create and amplify such additional resonance terms by using a specially shaped, such as a trapezoid, dithering PZT to induce altered modes of the excitation force and by controlling the amount of adhesive pasted onto the tuning fork. The shape of the resonance curve also dependents on how far in the tuning fork is placed on the dithering PZT, how much adhesive is used, and what kinds of methods are used to mount the tuning fork onto the dithering PZT, which may contribute to determining the coupling constant K.

The influence of the shear-force on the dynamic behavior of the asymmetric frequency response has not been discussed in this paper. Nevertheless, because the asymmetric characteristics of the main peak, *i.e.*, a suppressed noise signal and a steep slope with a high Q-factor, are nearly independent of the perturbed peak positions in our simulations, a drastic deformation of the asymmetric shape due to the shear force is not expected. On the other hand, the properties of the phase signal may be more complex when a shear-force exists. The dynamic behavior of a tuning-fork shear-force feedback system for an asymmetric frequency response is under examination.

III. CONCLUSION

In summary, we presented a simple two-degree-of-freedom coupled harmonic oscillator model to explain both the symmetric and the asymmetric frequency resonance behaviors of a tuning fork for shear-force detection. In particular, we demonstrated that our two-dimensional model can accurately reproduce the experimentally observed resonance curves on a local scale. In addition, we showed that the elastic terms of additional peaks had the effect of pinning down one side of the main peak so as to suppress the background noise and yield high Q-factors. An artificial perturbation, such as em-

ploying a deformed dithering PZT, was also suggested as a way to induce an acute slope for the lower-frequency region relative to the main peak for purposes of achieving high-resolution NSOM images.

ACKNOWLEDGMENTS

This research was supported by the Ministry of Science and Technology of Korea through the National Research Laboratory Program (Contact No. Ml-0203-00-0082).

REFERENCES

[1] D. W. Pohl, W. Denk and M. Lanz, Appl. Phys. Lett. **44**, 651 (1984).
[2] E. Betzig, M. Isaacson and A. Lewis, Appl. Phys. Lett. **51**, 2088 (1987).
[3] E. Betzig, J. K. Trautman, T. D. Harris, J. S. Weiner and R. L. Kostelak, Science **251**, 1468 (1991).
[4] R. C. Reddick, R. J. Warmack and T. L. Ferrill, Phys. Rev. B **39**, 767 (1989).
[5] N. F. van Hulst, M. H. P. Moers, O. F. J. Noordman, R. G. Tack, F. B. Segerink and B. Bolger, Appl. Phys. Lett. **62**, 461 (1993).
[6] A. Sakai, N. Sasaki and T. Ninomiya, J. Korean Phys. Soc. **42**, S1076 (2003).
[7] E. Betzig, P. L. Finn and J. S. Weiner, Appl. Phys. Lett. **60**, 2484 (1992).
[8] R. D. Grober, T. D. Harris, J. K. Trautman and E. Betzig, Rev. Sci. Instrum. **65**, 626 (1994).
[9] K. Karrai and R. D. Grober, Appl. Phys. Lett. **66**, 1842 (1995).
[10] S. Hong, J. Kim and K. Lee, J. Korean Phys. Soc. **40**, 861 (2002).
[11] A. G. T. Ruiter, J. A. Veerman, K. O. van der Werf and N. F. van Hulst, Appl. Phys. Lett. **71**, 28 (1997).
[12] T. Okajima and S. Hirotsu, Appl. Phys. Lett. **71**, 545 (1997).
[13] J. H. Park, M. R. Kim and W. Jhe, Opt. Lett. **25**, 628 (2000).
[14] R. Brunner, A. Bietsch, O. Hollricher and O. Marti, Rev. Sci. Instrum. **68**, 1769 (1997).
[15] L. Meirovitch, *Fundamentals of Vibrations* (McGraw-Hill, New York, 2001).
[16] A. V. Zvyagin, J. D. White, M. Kourogi, M. Kozuma and M. Ohtsu, Appl. Phys. Lett. **71**, 2541 (1997).
[17] H. Jeff Kimble, *Waves, Quantum Physics and Statistical Mechanics* (McGraw Hill, University of California, Berkeley, 1968).

Relative strength of the screened Coulomb interaction and phase-space filling on exciton bleaching in multiple quantum well structures

Moongoo Choi, Koo-Chul Je, Sang-Youp Yim, and Seung-Han Park*
National Research Laboratory of Nonlinear Optics, Yonsei University, Seoul 120-749, Korea
(Received 5 April 2004; published 20 August 2004)

We investigate the effect of resonantly excited excitons on the bleaching of $n=1$ and $n=2$ heavy-hole (hh) exciton resonances in *GaAs* multiple-quantum-well structures by using a pump-probe spectroscopic technique at low temperature under quasi-stationary excitation conditions. In particular, we present direct observation of long-range Coulomb screening by two-dimensional exciton-exciton interactions along with the unambiguous discrimination of screened Coulomb interaction and phase-space filling on the $n=1$ hh exciton bleaching. In addition, we find that the strength of long-range Coulomb screening on the $n=1$ hh exciton bleaching is only two to three times weaker than that of the phase-space filling at 10 K.

DOI: 10.1103/PhysRevB.70.085309 PACS number(s): 78.67.De, 71.35.Cc

Quantum confinement effects in semiconductor multiple quantum wells (MQW's) enhance excitonic features, including strong and well-resolved excitonic peaks in linear absorption even at room temperature.[1,2] With increasing densities of photo-generated free electrons and holes, the excitonic absorption spectra are observed to be shifted, broadened, and saturated due to the Pauli exclusion principle, the screening of Coulomb interaction, band-gap renormalization, etc.[3–5] The exclusion principle, consisting of phase-space filling (PSF) and exchange effects, is very short ranged compared to the screened Coulomb interaction. Hereafter, we will denote the PSF and exchange effects as PSF.

During the past decades, relative contribution of Coulomb screening (CS) and PSF to the density-dependent exciton bleaching in bulk and MQW structures have been intensively investigated under various excitation conditions.[6–13] Fehrenbach *et al.*[6] observed that the screening of excitons by surrounding excitons is much weaker than that by free carriers in bulk *GaAs*. In GaAs MQW's, Knox *et al.*[7] found that resonantly generated excitons produce more absorption bleaching than free-carrier pairs of equal densities at room temperature. Recently, Becker *et al.*[8] showed that the bleaching effect of "cold" neutral excitons is stronger than that of the same density of "cool" uncorrelated charged electron-hole pairs in *CdZnTe/ZnTe* MQW's. However, to our knowledge, no experimental data on the long-range CS of excitons by excitons in quasi-two-dimensional (quasi-2D) MQW's have been available.

In this Letter, we report the first direct observation of long-range CS by two-dimensional exciton-exciton interactions as well as unambiguous discrimination of CS and PSF effects on the $n=1$ heavy-hole (hh) exciton bleaching at low temperature ($T=10$ K). In particular, we measured the changes of optical absorption for $n=1$ hh and $n=2$ hh exciton resonances simultaneously in a *GaAs/AlGaAs* MQW by using a pump-probe spectroscopic technique under quasi-stationary $n=1$ hh excitation conditions with a narrow-band nano-second laser. We observed the absorption bleaching of $n=1$ hh exciton resonance due to PSF and long-range CS, as expected. Surprisingly, however, we were also able to observe that neutral excitons generated at $n=1$ hh induce the bleaching of excitons at $n=2$ hh, strongly indicating the presence of long-range CS in the quasi-two-dimensional system. We subtracted the variation of $n=2$ hh from that of $n=1$ hh in order to deduce the PSF effect on the $n=1$ hh bleaching since the $n=1$ hh absorption bleaching is caused by both PSF and long-range CS. From the data we find that the relative strength of the absorption bleaching effect by PSF is only two to three times stronger than that of long-range CS. It agrees well with estimates from our theoretical calculation based on the multi-band-semiconductor Bloch equations.[5,14]

Figure 1 shows the spectral shapes of the pump pulse, the broadband probe pulse, and the absorbance, $\alpha L=-\ln(I_t/I_0)$, of a *GaAs/AlGaAs* MQW at 10 K. Here, I_0 and I_t are incident and transmitted intensities, respectively. The sample used in this study consists of 65 periods of 75 Å GaAs wells and 100 Å $Al_{0.34}Ga_{0.66}As$ barriers grown by molecular beam epitaxy. The substrate was removed by selective etching over part of the sample in order to allow transmission measurements. The resulting sample had sufficiently good optical quality in the vicinity of the excitonic peaks. The well-defined $n=1$ hh and $n=2$ hh exciton peaks were observed at 1.5684 eV and 1.6994 eV with line widths of ~2.7 meV and

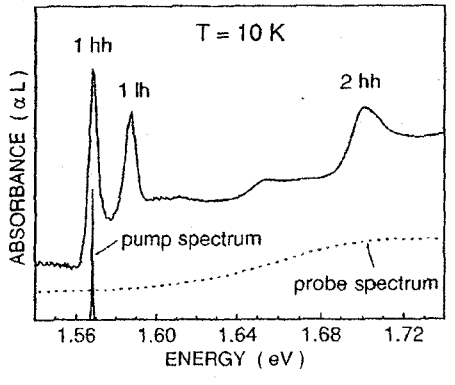

FIG. 1. Linear absorption spectrum of *GaAs/AlGaAs* MQW structure at 10 K, including the spectral shapes of the pump and probe pulses.

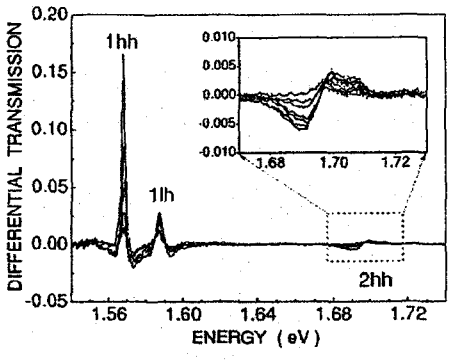

FIG. 2. Low temperature differential transmission spectra measured at both $n=1$ hh and $n=2$ hh excitons. The inset shows the enlarged view of differential transmission spectra near the $n=2$ hh excitons.

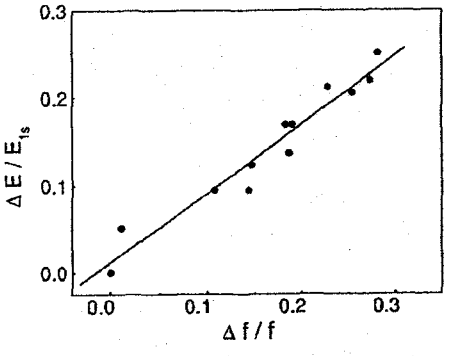

FIG. 3. The fractional change of exciton binding energy as a function of relative decrease of exciton oscillator strength.

~7.8 meV, respectively. The peak around 1.587 eV corresponds to the $n=1$ light-hole (lh) exciton.

The experiments were performed using a quasi-stationary pump and probe measurement technique. A Nd:YAG laser pumped dye-laser system operating at $n=1$ hh exciton resonance with a repetition rate of 10 Hz was employed for the pump beam. The probe pulses with very low intensity spectrally cover both $n=1$ hh and $n=2$ hh exciton resonances, as shown in Fig. 1. The pump pulses were ~5 ns in duration and the probe focus was kept much smaller than the size of the pump beam. A shutter synchronized with the laser pulse was used to get a high signal-to-noise ratio and remove the scattered laser beams. The transmission spectra with and without the pump beam were monitored using an optical multi-channel analyzer (OMA) with image sensing photodiode arrays.

Figure 2 shows the low temperature differential transmission spectra (DTS) which are taken near both $n=1$ hh and $n=2$ hh exciton resonances. The DTS is defined as $DTS=(T-T_0)/T$, where T is the probe transmission with the pump present and T_0 is the probe transmission without the pump. The spectra show induced transmission variations, i.e., bleaching of various excitonic transitions. The peaks are caused by variations of oscillator strengths of the excitons, where the absolute value of the induced transmission becomes larger as the pump beam intensity increases. The DTS around the $n=1$ hh excitonic resonance is positive, however, the high energy side of $n=1$ hh is negative, which originates from spectral overlapping of $n=1$ hh and $n=11$ h resonances.

In addition, we also observe absorption bleaching near the $n=2$ hh excitons, as is depicted in the inset of Fig. 2. It is worth noting that the wavelength of the pump beam is tuned at the $n=1$ hh exciton resonance, the excited excitons are created by the pump pulse with $\Delta E_{\text{Laser}}<1.0$ meV (much smaller than the $n=1$ hh exciton linewidth, $\Delta E_{1\,hh}$ ~2.7 meV) at 10 K, where the thermal-LO-phonon density is ignorable, and the decay time of excitons is the order of nanoseconds even at room temperature.[15–17] In order to minimize the effect of spectral hole burning due to the inhomogeneous broadening, in addition, the DTS were measured by controlling the intensity of the pump beam to create the carrier densities of up to 1.4×10^{11} cm^{-2}. Since only the ground-state excitons in the first subband are generated, the $n=2$ hh excitons in the second sub-band are affected solely by the long-range CS. In contrast to the $n=1$ hh exciton, however, negative and positive DTS are obtained in the low and high energy sides of the $n=2$ hh exciton, respectively. This means that the $n=2$ hh excitonic absorption spectra are red-shifted for increased exciton density. Therefore, the experimental observation clearly indicates the existence of long-range CS effects in the quasi-2D systems.

There are mainly two many-body effects acting in opposite directions of the peak shifts; an attractive inter-particle interaction influenced by long-range CS and a repulsive interaction by PSF, which contribute to red and blue shifts, respectively.[3,5,12] As mentioned above, the $n=2$ hh excitons are only affected by an attractive long range CS, exhibited by a red-shift of the $n=2$ hh exciton resonance. On the contrary, the blue-shifted $n=1$ hh exciton resonance is affected by both a repulsive PSF and an attractive long-range CS. These two opposite effects lead to the net change of the $n=1$ hh exciton resonance. The observed blue shift of the $n=1$ hh excitions indicates that PSF is stronger than long-range CS in a quasi-2D system. Note that both attractive and repulsive interactions also produce a reduction of excitonic oscillator strength. In summary, the long-range CS affects excitons of all sub-bands, whereas the PSF effects are restricted to the $n=1$ hh excitons of the occupied sub-band.

Figure 3 displays the relation between the peak shift and bleaching of the $n=1$ hh excitons due to PSF, which is given by $(\Delta E/E_{1s})=C(\Delta f_0/f_0)$,[3,11,18] where E_{1s} is a binding energy of bare $n=1$ hh excitons and f_0 is its oscillator strength. The magnitudes of Δf_0 and ΔE are determined by Gaussian fitting of nonlinear absorbance obtained by adding the DTS to the linear absorbance in Fig. 1. In particular, for an accurate comparison, we subtract the reduction ratio of oscillator strength in the $n=2$ hh excitons due to long-range CS from that of the $n=1$ hh excitons in order to eliminate the long range CS effect in the DTS. In addition, the net blue-shift of the $n=1$ hh excitons due to only PSF is extracted by compensating the red-shift of the $n=2$ hh excitons due to long-range CS with the observed blue-shift of the $n=1$ hh excitons. As can be seen in Fig. 3, we find a good linear

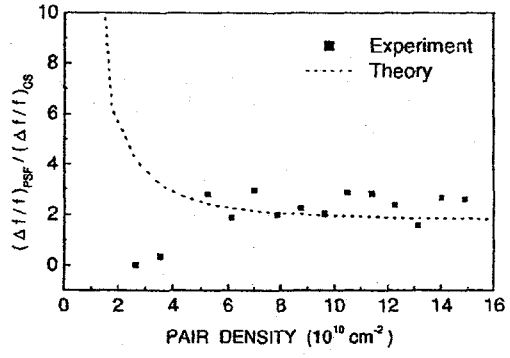

FIG. 4. Relative strength of PSF and CS on the $n=1$ hh exciton bleaching for various excitation densities. The dashed line corresponds to the theoretical calculation.

correlation between the net fractional change of exciton binding energy and $\Delta f_0/f_0$ for PSF. The coefficient C is obtained to be 0.8, which is 1.6 times larger than the predicted value. Nevertheless, it is comparable to previously reported experimental values of $0.3\sim1.0$.[11,18] The coefficient C is known to be close to zero for 3D systems, while for 2D systems they have nonzero values dependent upon their well size.[3,6,11,18]

The experimental data points in Fig. 4 show the ratio of the contribution of PSF and CS on the $n=1$ hh exciton bleaching for various excitation densities. It is found that the bleaching rate is almost constant between 2 and 3 with increasing carrier densities from 3×10^{10} cm^{-2} to 1.4×10^{11} cm^{-2}. In other words, bleaching due to PSF is nearly unvaried with values at around 2–3 times larger than that due to CS. In order to understand this behavior, we investigated the relative strength of bleaching effects due to CS and PSF theoretically by using the multi-band semiconductor Bloch equations onto the lowest 1 s exciton state. The nonlinear optical response of a semiconductor up to the third-order can be described by[5]

$$\left(-i\frac{\partial}{\partial t}-\Omega_0\right)P(t)=-\mu\cdot E(t)+b\mu\cdot E(t)|P(t)|^2+vP(t)|P(t)|^2.$$

Here, Ω_0 is the frequency of the exciton resonance, μ its transition dipole moment, $E(t)$ the external laser field, and μP the interband polarization. Moreover, $b=2\Sigma_{\vec{k}}\,\phi(\vec{k})^3$ represents a nonlinearity induced by Pauli blocking and $v=2\Sigma_{\vec{k}}\,V_s(\vec{k}-\vec{k}')[\phi(\vec{k})^3\phi(\vec{k}')-\phi(\vec{k})^2\phi(\vec{k}')^2]$ is a nonlinearity originating from the Coulomb interaction. $\phi(\vec{k})$ is assumed to be a real wavefunction of the 1s exciton and $\vec{k}$ denotes the momentum associated with the relative motion of electrons and holes. The two terms, which determine v, are originated from the field renormalization and the band-gap renormalization in the full semiconductor Bloch equation. The screened two-dimensional Coulomb potential is assumed to be

$$V_s(\vec{k}-\vec{k}')=\frac{2\pi e^2}{\varepsilon_0 L^2}\frac{1}{(\vec{k}-\vec{k}')+\kappa}, \quad (1)$$

treated statically using the plasmon-pole approximation.[19,20] The inverse of the screening length, κ, is calculated self-consistently according to $\kappa^2=(2\pi e^2/\varepsilon_0 V)\Sigma_n\,[df_n(k)/d\varepsilon]$, where $f_n(k)$ is the distribution function of the band index n, and ε_0 is the background dielectric constant. Within these approximations the explicit form of the third-order response is characterized by the ratio v/b, which determines the relative strength of the two sources of optical nonlinearity. We have ignored the light-hole states in our theoretical consideration. The calculated bleaching rate is shown in Fig. 4 as a dotted line. As can be seen in the figure, the bleaching due to PSF is estimated to be constant around 2 times larger than that due to CS within the carrier concentration 2.0×10^{11} cm^{-2}.[14] We find that the theoretical calculations agree well with experimental results. However, the calculated bleaching rate shows a rapid increase for very low densities. This result is presumed to come from very small excitonic bleaching of the $n=2$ hh peak due to CS in the very low densities, in which our calculations are limited.

In conclusion, we have found that the $n=2$ hh exciton resonance is consistently red-shifted by two-dimensional exciton-exciton interactions in *GaAs/AlGaAs* MQW's under quasi-stationary $n=1$ hh excitation conditions at low temperatures. This confirms that the effect of the excited excitons at $n=1$ hh on excitons at $n=2$ hh is primarily due to long-range CS, which is not negligible in the quasi-2D system. On the other hand, the $n=1$ hh exciton resonance is blue-shifted by the competition of both repulsive PSF and attractive long-range CS, which should be compensated. After discriminating PSF and long-range CS effects in the $n=1$ hh exciton bleaching, we find that the relative strength of absorption bleaching due to long-range CS is only 2 to 3 times weaker than that of PSF. The theoretically calculated value based on the multi-band semiconductor Bloch equations is in good agreement with our experimental results.

This research was supported by the Ministry of Science and Technology of Korea through the National Research Laboratory Program (Contract No. M1-0203-00-0082).

*Electronic address: shpark@phya.yonsei.ac.kr

[1] D. S. Chemla, D. A. B. Miller, P. W. Smith, A. C. Gossard, and W. Wiegmann, IEEE J. Quantum Electron. 20, 265 (1984).

[2] C. Weisbuch and B. Vinter, *Quantum Semiconductor Structures* (Academic, San Diego, 1991).

[3] S. Schmitt-Rink, D. S. Chemla, and D. A. B. Miller, Phys. Rev. B 32, 6601 (1985).

[4] H. Haug and S. Schmitt-Rink, J. Opt. Soc. Am. B 2, 1135 (1985).

[5] H. Haug and S. W. Koch, *Quantum Theory of the Optical and Electronic Properties of Semiconductors* (World Scientific, Sin-

gapore, 1994).
[6]G. W. Fehrenbach, W. Schafer, J. Treusch, and R. G. Ulbrich, Phys. Rev. Lett. **49**, 1281 (1982).
[7]W. H. Knox, R. L. Fork, M. C. Downer, D. A. B. Miller, D. S. Chemla, and C. V. Shank, A. C. Gossard, and W. Wiegmann, Phys. Rev. Lett. **54**, 1306 (1985).
[8]P. C. Becker, D. Lee, A. M. Johnson, A. G. Prosser, R. D. Feldman, R. F. Austin, and R. E. Behringer, Phys. Rev. Lett. **68**, 1876 (1992).
[9]D. R. Wake, H. W. Yoon, J. P. Wolfe, and H. Morkoc, Phys. Rev. B **46**, 13 452 (1992).
[10]E. Lach, M. Walther, G. Traenkle, A. Forchel, and G. Weimann, Phys. Status Solidi B **150**, 679 (1988).
[11]K.-H. Schlaad, Ch. Weber, J. Cunningham, C. V. Hoof, G. Borghs, G. Weimann, W. Schlapp, H. Nickel, and C. Klingshirn, Phys. Rev. B **43**, 4268 (1991).
[12]S. Hunsche, K. Leo, H. Kurz, and K. Kohler, Phys. Rev. B **49**, 16 565 (1994).
[13]W. H. Knox, C. Hirlimann, D. A. B. Miller, J. Shah, D. S. Chemla, and C. V. Shank, Phys. Rev. Lett. **56**, 1191 (1986).
[14]K-C. Je, M. Choi, S.-Y. Yim, J.-S. Ahn and S.-H. Park, Phys. Rev. B **66**, 155312 (2002).
[15]M. Colocci, M. Gurioli, and A. Vinattieri, J. Appl. Phys. **68**, 2809 (1990).
[16]J. E. Fouquet and A. E. Siegman, Appl. Phys. Lett. **46**, 280 (1985).
[17]W. Pickin and J. P. R. David, Appl. Phys. Lett. **56**, 268 (1990).
[18]D. Hulin, A. Mysyrowicz, A. Antonetti, A. Migus, W. T. Masselink, H. Morkoc, H. M. Gibbs, and N. Peyghambarian, Phys. Rev. B **33**, 4389 (1986).
[19]H. Haug and C. Ell, Phys. Rev. B **46**, 2126 (1992).
[20]K-C. Je, K-C. Seo and Y. Kim, J. Appl. Phys. **86**, 6196 (1999).

Enhancement of shear-force sensitivity using asymmetric response of tuning forks for near-field scanning optical microscopy

Jang-Hoon Yoo, Jae-Hoon Lee, Sang-Youp Yim, and Seung-Han Park

Department of Physics, Yonsei University, Seoul 120-749, Korea
shpark@phya.yonsei.ac.kr

Myong-Do Ro, Joo-Ho Kim, and In-Sik Park

Media Solution Team, Digital Media R&D Center, Samsung Electronics Co., Ltd., 416 Maetan-3Dong, Yeongtong-Gu, Suwon, Kyungki-Do 443-742, Korea

Kyuman Cho

Department of Physics, Sogang University, Seoul 121-742, Korea

Abstract: Resonance characteristics of a tuning fork are investigated to enhance the shear-force detection sensitivity for near-field scanning optical microscopy. In particular, we show that the asymmetric frequency response of a tuning fork can be utilized to increase quality factors and suppress the background feedback signal. The pinning down effect on one side of the main peak can readily elevate vertical sensitivity and stability. A simplified model based on a coupled harmonic oscillator is presented to describe the asymmetric resonance behavior of the tuning fork. We also show improved topographic images of a blue-ray disc and optical images of a chromium pattern on the quartz using the asymmetric resonance.

OCIS codes: (120.6660) Surface measurement, roughness, (180.5810) Scanning microscope

References and links

1. D. W. Pohl, W. Denk, and M. Lanz, "Optical stethoscopy: image recording with resolution λ /20,"Appl. Phys. Lett. **44**, 651 (1984).
2. E. Betzig, J. K. Trautman, T. D. Harris, J. S. Weiner, and R. L. Kostelak, "Breaking the diffraction barrier: optical microscopy on a nanometric scale," Science **251**, 1468 (1991).
3. R. Toledo-Crow, P. Yang, Y. Chen, and M. Vaez-Iravani, "Near-field differential scanning optical microscope with atomic force regulation," Appl. Phys. Lett. **60**, 2957 (1992).
4. E. Betzig, P. L. Finn, and J. S. Weiner, "Combined shear force and near-field scanning optical microscopy," Appl. Phys. Lett. **60**, 2484 (1992).
5. K. Karrai and R. D. Grober, "Piezoelectric tip-sample distance control for near-field optical microscopes,"Appl. Phys. Lett. **66**, 1842 (1995).
6. A. G. T. Ruiter, J. A. Veerman, K. O. van der Werf, and N. F. van Hulst, "Dynamic behavior of tuning fork shear-force feedback," Appl. Phys. Lett. **71**, 28 (1997).
7. T. Okajima and S. Hirotsu, "Study of shear force between glass microscope and mica surface under controled humidity," Appl. Phys. Lett. **71**, 545 (1997).
8. W. A. Atia and C. C. Davis, "A phase-locked shear-force microscope for distance regulation in near-field optical microscopy," Appl. Phys. Lett. **70**, 405 (1997).
9. M. J. Gregor, P. G. Blome, J. Schöfer, and R. G. Ulbrich, "Probe-surface interaction in near-field optical microscopy: The nonlinear bending force mechanism," Appl. Phys. Lett. **68**, 307 (1996).
10. Y. Martin, C. C. Williams, and H. K. Wickramashinghe, "Atomic force microscope-force mapping and profiling on a sub 100 Å scale," J. Appl. Phys. **61**, 4723 (1987).
11. R. D. Grober, J. Acimovic, J. Schuck, D. Hessman, P. J. Kindlemann, J. Hespanha, A. S. Morse, K. Karrai, I. Tiemann, and S. Manus, "Fundamental limits to force detection using quatz tuning froks," Rev. Sci. Instrum. **71**, 2776 (2000).
12. R. S. Decca, H. D. Drew, and K. L. Empson, "Mecahnical oscillator tip-to-sample separation control for near-field optical microscopy," Rev. Sci. Instrum. **68**, 1291 (1997).

#4890 - $15.00 US
Received 29 July 2004; revised 7 September 2004; accepted 9 September 2004

13. J. Salvi, P. Chevassus, A. Mouflard, S. Davy, M. Spajer, and D. Courjon, "Piezoelectric shear force detection: a geometry avoiding critical tip/tuning fork gluing," Rev. Sci. Instrum. 69, 1744 (1998).
14. A. V. Zvyagin, J. D. White, M. Kourogi, M. Kozuma, and M. Ohtsu, "Solution to the bistability problem in shear force distance regulation encountered in scanning force and near-field optical microscopes," Appl. Phys. Lett. 71, 2541 (1997).
15. D.P. Tsai and Y. Y. Lu, "Tapping-mode tuning fork force sensing for near-field scanning optical microscopy," Appl. Phys. Lett. 73 2724 (1998)
16. L. Meirovitch, *Fundamentals of Vibrations* (McGraw-Hill, New York, 2001).
17. M. Ro, K. Lee, D. Yoon, I. Hwang, C. Park, Y. Kim, I. Park, and D. Shin, "Experimental results of 3-piece 0.4mm molded substrate," Jpn. J. Appl. Phys. 40, 1666 (2001).

1. Introduction

Near-field scanning optical microscopes (NSOM) have been developed to get images of much better resolution than that of the conventional diffraction-limited optical microscopes [1,2]. The NSOM often employs a tapered optical fiber as a probe to obtain near-field optical signals as well as topographic images. The highest possible resolution of the NSOM is achieved when the probe-to-surface separation is kept constant in the near-field regime over the entire scanning process. Therefore, various distance regulation schemes have been proposed, including electron tunneling[1], frustrate total internal reflection, atomic force probing, and shear-force distance control[3,4]. To date, the shear-force detection technique is widely adopted for the probe-to-surface distance control because of its simplicity, in which a probe is vibrated parallel to a sample surface and its oscillating amplitude is measured [5-8].

A method to produce the probe oscillation and measure its amplitude is to utilize a tuning fork with one prong attached to the tapered optical fiber and the other mounted on a dithering piezoelectric transducer (PZT) plate. At resonance, the tuning fork generates an oscillating piezoelectric signal proportional to the probe oscillation amplitude [5]. As the probe approaches normally onto the sample surface, the oscillating piezoelectric signal decreases since the resonance frequency is shifted to a higher frequency [6,7,9]. The shifting effects indicate that the low frequency slope of the main resonance peak should be used as the shear-force control signal. The resonance characteristics of the tuning fork play an important role to determine the shear-force detection sensitivity for the probe-surface distance regulation. High shear-force detection sensitivity requires a large quality factor Q of the tuning fork since the derivative of the smallest detectable force is proportional to $1/\sqrt{Q}$ [8,10]. For a standard proportional-integral closed loop configuration, electrical reduction of resonance background noise without *minimizing* Q should also be provided to get better stability as well as fast response [11]. However, since the feedback signal does not go to zero when the tip is in contact with the surface, a calibration for the approach curve is not accurate and the distance regulation signal becomes unstable. This problem always occurs such the techniques based on quartz mode tuning forks including the tapping mode, because the resonance frequency is shifted as the tip approaches the sample. Up to now, there are only few approaches to avoid such problems [12,13]. In order to obtain certain resonance characteristics desired for high resolution, we should consider many subtle details, such as the mounting conditions and the mounting positions of the tuning fork on the dithering PZT, along with the shape of the dithering PZT.

In this letter, we investigate symmetric and asymmetric responses of the tuning fork to enhance the shear-force detection sensitivity of the probe-sample distance-control for the NSOM system. Particularly, we present substantial improvement of the shear-force detection sensitivity utilizing the asymmetric resonance of a tuning fork. We show that the asymmetric frequency response with a large quality factor Q of ≥ 2500 and a suppressed background feedback signal can be generated by controlling the conditions on an edge-clipped dithering PZT plate. The asymmetric system applied to the NSOM allows us to acquire nano-scale surface images with a shear-force vertical stability of less than 2nm. A simplified model based

#4890 - $15.00 US Received 29 July 2004; revised 7 September 2004; accepted 9 September 2004

on a coupled harmonic oscillator system is also presented to describe the asymmetric behavior of the tuning fork.

2. Experiments

A schematic diagram of our NSOM is shown in Fig. 1. A commercially available metal-coated tapered fiber-probe with an opening aperture of $100nm$ is glued along the side of one prong of a tuning fork with a resonance frequency of $32{,}768\ Hz$. The piezoelectric signal from the tuning fork is detected by a $1\ M\Omega$ load resistor with a high-impedance pre-amplifier (AD524) of $100\times$ gain. This signal is fed into a lock-in amplifier (EG&G 7265) and a "fast X" output from the lock-in amplifier is employed as an error signal for the feedback loop to take advantage of its rapid phase-signal response. The distance control using the amplified signal is achieved by a proportion and integration (PI) feedback controller. The bandwidth of our system was about 30Hz, which was measured by an actuator (Jena TRITOR 100) oscillating the sample intentionally. The distance between the tip and sample was positioned by a piezoelectric tube which was calibrated using a Michelson interferometer.

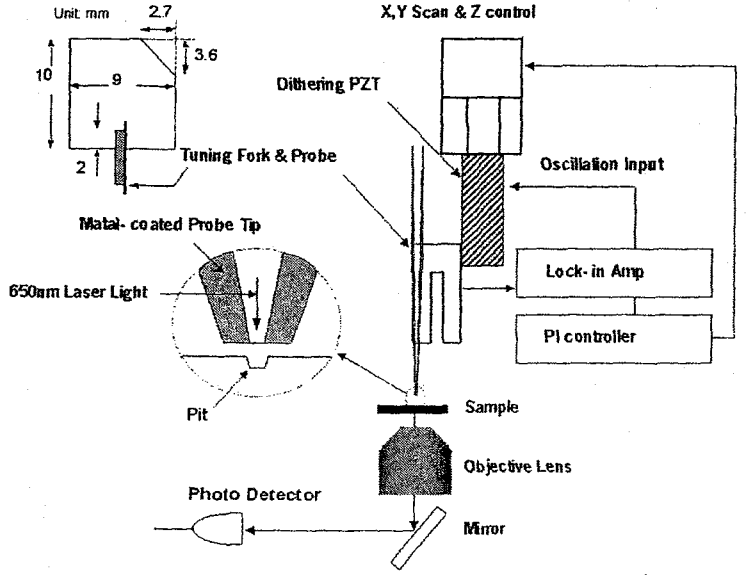

Fig. 1. Schematic diagram of the near field scanning optical microscope.

Figure 2(a) displays a typical symmetric response of the piezoelectric signal amplitude, with a Q factor of ~1600 in our system. Raising the dithering voltage increases the off-resonance feedback signal, which limits the shear-force vertical sensitivity. In order to enhance the Q factor and locally suppress the feedback signal, as shown in Fig. 2(b), an asymmetric frequency resonance is proposed by attaching a fiber-probe along to one (upper) prong of the tuning fork and the other (lower) arm to the edge-clipped PZT plate. We found that the symmetric Lorentzian response curve can be readily broken by artificial perturbation, such as chipping off a piece of the corner of the PZT plate, and altering mounting conditions of the tuning fork on the dithering plate and the fiber probe on the prong. Practically, our interest is focused on the case where the asymmetric resonance peak has a better Q-factor in

#4890 - $15.00 US
Received 29 July 2004; revised 7 September 2004; accepted 9 September 2004

the lower frequency region with off-resonance amplitudes greatly suppressed. With such resonance curves, we have found that it is easier to obtain higher vertical and lateral resolutions, yielding naturally higher Q-factors. We have tried to create and amplify such additional resonances by using a specially shaped, such as a trapezoid, dithering PZT to induce altered modes with the excitation force, and also by controlling the amount of adhesive pasted onto the tuning fork. The shape of the resonance curve is also dependent on where the tuning fork is placed on the dithering PZT, how much adhesive is used, and what kinds of methods are used to mount the tuning fork onto the dithering PZT.

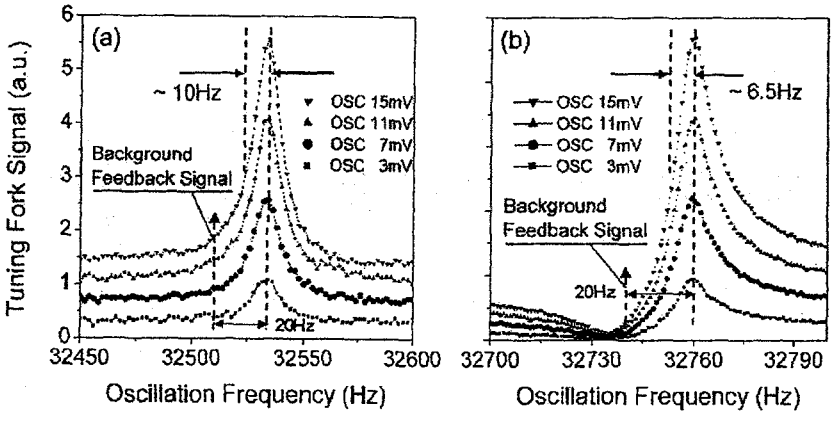

Fig. 2. The amplitude of the PZT signal measured as a function of driving frequency. (a) and (b) show symmetric and asymmetric responses with damping, respectively. The driving voltage is varied from 3mV to 15mV. A relatively high Q-factor (≥ 2500) is achieved in the case of (b) compared to (a), where the Q-factor is ~1600 and the background feedback signal is increased for higher dithering voltages.

The breaking of the symmetric shape of the main resonance peak creates two or more resonance peaks of the tuning fork [14]. In fact, as shown in Fig. 3, many more supplemental peaks are observed when the voltage applied onto the dithering PZT plate is increased. The largest peak is located at 32,760 *Hz* near the original resonance frequency, whereas the other peaks are located at higher or lower frequencies. It is observed that a supplementary peak, largely damped, is located around 4.2 *kHz* away from the main peak, as shown in Fig. 3. Through a variety of experiments, such as breaking one of the prongs off, we find that the upper prong of tuning fork had a dominant effect on the main peak. As is expected, however, resonance characteristics are also strongly dependent upon the mounting position of the tuning fork on the dithering PZT plate. A large Q (≥ 2500) of the tuning fork and tip assembly with an almost completely suppressed off-resonance feedback signal can be obtained by gluing approximately two millimeters of the lower prong of the tuning fork to the edge-clipped dithering PZT plate. Here, Q is estimated to be two times of the half width at half maximum of the tuning fork resonance peak in the low frequency side of the peak since the slope of low frequency side is used for the tip-to-sample distance control. Note that the feedback signal at

#4890 - $15.00 US
Received 29 July 2004; revised 7 September 2004; accepted 9 September 2004

the low frequency side, specifically at around $32{,}735\,Hz$, remains below 2.5% of the amplitude of the resonance peak, even though the dithering voltage is increased. This strongly indicates that the asymmetric frequency dependence of the output signal can enhance the Q-factor and the detection sensitivity for the distance control process of shear-force modes. The asymmetric frequency dependence with a pinning down effect at the higher frequency side can also be used for the tapping mode NSOM system because for this case the resonance peak is slightly shifted to the lower side when the probe approaches to the sample surface [15].

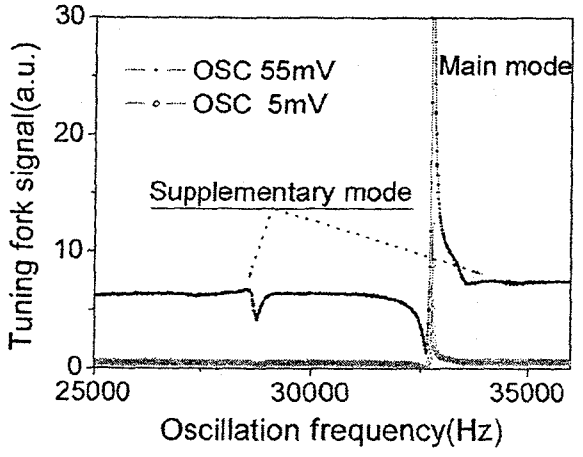

Fig. 3. Resonance response profiles measured as a function of driving frequency. The driving voltage is varied from 5mV to 55mV. The main resonance peak is detected around $32{,}760\,Hz$ while a second peak is also detected near $28{,}540\,Hz$, respectively. Additional supplementary modes are also apparent at higher frequencies than the main resonance frequency.

According to the experiments, the special shape of the PZT plate provides many more subsidiary modes of vibration. We can observe many peaks not only around the region of resonance ($\sim 32768\,Hz$) but also along a larger inclusive span ($10000 \sim 50000\,Hz$). In particular, through repeated experiments, we have found that two peaks were observed to be relatively larger than other peaks, suggesting a simplified approximation of the shear force detection system as a 2 degree-of-freedom coupled oscillator with harmonic excitations.

3. Theoretical modeling

In order to understand the asymmetric resonance behavior of the tuning fork, therefore, we introduce a coupled two-degree-of-freedom harmonic oscillator system, *i.e.*,

$$M\ddot{\mathbf{x}}(t) + C\dot{\mathbf{x}}(t) + K\mathbf{x}(t) = \mathbf{F}(t) \tag{1}$$

Here, the effective mass, the damping coefficients, and the stiffness matrices with a coupling constant K can be written as $M = \begin{pmatrix} m_1 & 0 \\ 0 & m_2 \end{pmatrix}$, $C = \begin{pmatrix} m_1\Gamma_1 & 0 \\ 0 & m_2\Gamma_2 \end{pmatrix}$, $K = \begin{pmatrix} k_1 + \mathrm{K} & -\mathrm{K} \\ -\mathrm{K} & k_2 + \mathrm{K} \end{pmatrix}$.

Assuming a harmonic driving force, $\mathbf{F}(t)$ and $\mathrm{x}(t)$ can be written as $\mathbf{F}(t) = \mathbf{F}_0 \exp(i\omega t)$ and $\mathrm{x}(t) = \mathbf{X}(i\omega)\exp(i\omega t)$, respectively, where $\mathbf{F}_0$ is a constant

#4890 - $15.00 US

Received 29 July 2004; revised 7 September 2004; accepted 9 September 2004
20 September 2004 / Vol. 12, No. 19 / OPTICS EXPRESS 4471

vector and $\mathbf{X}(i\omega)$ is a complex vector depending on the driving frequency ω. Then, the solution of Eq. (1) is given by [16]

$$X_1(i\omega) = \frac{(-\omega^2 m_2 + i\omega m_2\Gamma_2 + k_2 + \mathrm{K})F_1 + \mathrm{K}F_2}{(-\omega^2 m_1 + i\omega m_1\Gamma_1 + k_1 + \mathrm{K})(-\omega^2 m_2 + i\omega m_2\Gamma_2 + k_2 + \mathrm{K}) - \mathrm{K}^2}$$
$$X_2(i\omega) = \frac{\mathrm{K}F_1 + (-\omega^2 m_1 + i\omega m_1\Gamma_1 + k_1 + \mathrm{K})F_2}{(-\omega^2 m_1 + i\omega m_1\Gamma_1 + k_1 + \mathrm{K})(-\omega^2 m_2 + i\omega m_2\Gamma_2 + k_2 + \mathrm{K}) - \mathrm{K}^2} \quad (2)$$

with a superposed response function defined as $X_S(i\omega) \equiv X_1(i\omega) + X_2(i\omega)$. The magnitude of the frequency response, which is actually the superposed electrical signal from the quartz tuning fork, can be written by

$$|X_S(i\omega)| = [X_S(i\omega)\bar{X}_S(i\omega)]^{1/2} = \{[\mathrm{Re}\,X_S(i\omega)]^2 + [\mathrm{Im}\,X_S(i\omega)]^2\}^{1/2} \quad (3)$$

Two resonance peaks are obtained when taking similar but slightly different mass and stiffness values for the two terms X_1 and X_2. If one of the peaks is substantially suppressed by damping, a rapid drop of amplitude is observed in either higher or lower frequency regions of the larger main peak, depending on the different values of the coupling constant K, and peak positions mostly depending on k_1/m_1 and k_2/m_2 as shown in Fig. 4(a), (b). Figure 4(b) shows simulations of resonance curves based on our model, with the parameters of $m_1 = 1.000\times10^{-4}$, $m_2 = 1.015\times10^{-4}$, $\Gamma_1 = 5$, $\Gamma_2 = 10$, $k_1 = 107200$, $k_2 = 106300$, and $K = 100$. The external forces are varied from $3F$ to $15F$, where the force is given by $F = \begin{pmatrix} 1 \\ 10 \end{pmatrix} \exp(i\omega t)$.

The overall shape as well as the suppressed signal in the low frequency side of the experimentally observed asymmetric resonance profiles is well reproduced in the simulation. The resonance curve with a pinning down frequency response at the higher frequency side is also simulated for the tapping mode systems as shown in Fig. 4(a), where the parameters are the same as for the shear-force system except for the coupling constant set at $K = 400$. For the simulations, only two peaks are utilized in order to obtain the asymmetric resonance features with a suppressed off-resonance signal. As mentioned above, however, it should be emphasized that the actual system is much more complicated having many different resonance peaks [14]. These peaks come from different vibration modes of the tuning fork. One possibility is the existence of a vibration mode along the perpendicular direction of the typical vibration mode, owing to the fact that the dithering PZT is vibrating not only along the direction normal to its surface but also along the orthogonal direction. Since the tuning fork is a beam instead of a simple spring mass system and its beam vibrations have many harmonic modes and nonlinearities, in addition, multiple modes can be produced. Any such vibration mode which has a large damping term and a high F/m factor may contribute to a drop on one side of the main peak. According to our model, it is found that the asymmetric resonance curve with a drop at the lower frequency side is mainly due to a coupled vibration of the shear-force mode tuning fork. The coupling constant K may be determined by the mounting methods of the tuning fork.

#4890 - $15.00 US
Received 29 July 2004; revised 7 September 2004; accepted 9 September 2004

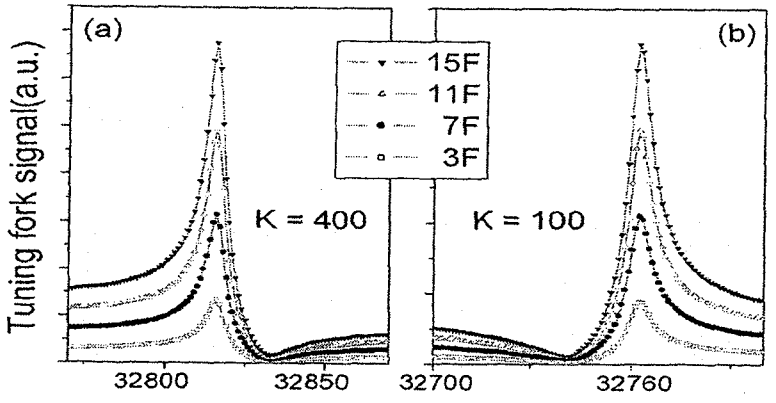

Fig. 4. Asymmetric resonance response curves simulated by a coupled two-degree-of-freedom harmonic oscillator system. Simulations of a suppressed signal in the high frequency side with K=400 for tapping mode systems(a) and in the low frequency side with K=100 for shear-force mode systems(b).

4. Results and conclusions

Figure 5(a) shows the topographic image of the blue-ray optical disc obtained by using the asymmetric response of the tuning fork while Fig. 5(b) and (c) show the cross-section points measured along the black lines. The cross section lines are low-pass filtered to remove high frequency noise. As shown in the inset of Fig. 5(b), it is also found that the shear-force vertical stability is less than 2 nm while scanning the surface along the black line.

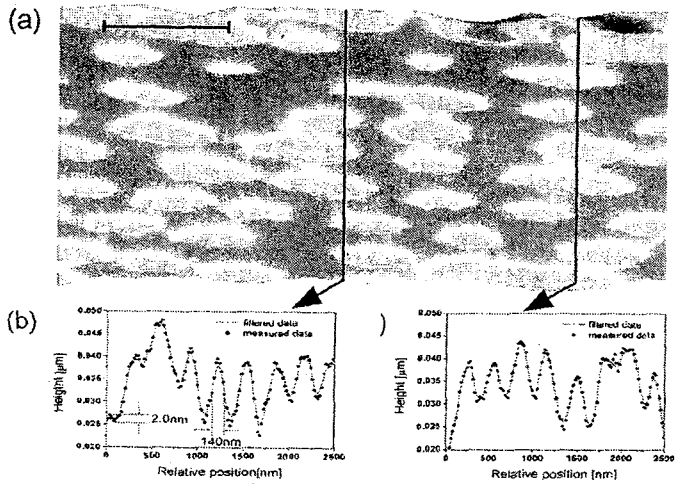

Fig. 5. (a) Topographic NSOM images of a blue-ray optical disc obtained by utilizing an asymmetric response and (b),(c) show the cross-section view having a vertical stability of less than 2 nm .

The low frequency slope of the main resonance peak is used as the shear-force control signal since the resonance frequency is shifted to a higher frequency as the tip approaches normally onto the sample surface. The asymmetric response with a drop in the low frequency

#4890 - $15.00 US
Received 29 July 2004; revised 7 September 2004; accepted 9 September 2004

region is more sensitive than that of the high frequency region. Applying this asymmetric system to our NSOM, high resolution images are obtained for a blue-ray optical disc having a sequence of nano-scale pits. The commercialized AFM images of the poly-carbonate high-density optical disc reveal that the track pitch, the pit width, and the depth of the pit are measured to be $\sim 320nm$, $\sim 100nm$, and $\sim 70nm$, respectively[17].

Figure 6(a) shows the topographic images of the blue-ray optical disc and its cross-section view was obtained as shown in Fig. 6(b) using a symmetric frequency response of the tuning fork. The measured vertical stability of the symmetric case was about 10nm which was inferior to the asymmetric case(~2nm).

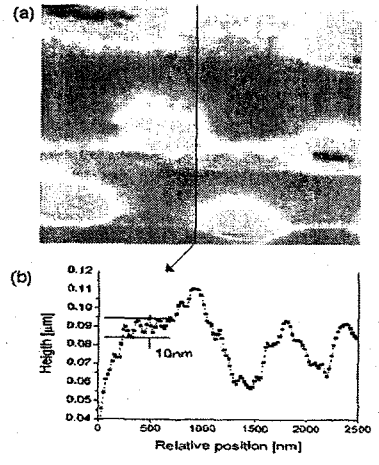

Fig. 6. (a) Topographic NSOM images of blue-ray optical disc obtained by utilizing a symmetric response and (b) the cross-sectional view having a vertical stability of about 10nm.

The fiber probe has an outer diameter larger than $500\ nm$, which is much larger than the pit size, not having have a super tip which is verified by tunneling electron microscope(TEM) images. Therefore, the probe should not be able to trace the sample surface to the bottom of the pits, indicating that the measured data(~20nm) do not display the actual topographical depth of the pits but in fact show a variation of the distance regulation signal due to the inconstant density distribution of the surface. The regions of the pits have a relatively lower density than its surroundings, giving a non-uniform density distribution

On the other hand, patterns of larger scale compared to the blue-ray disc sample were traced from peak to valley as shown in Fig. 7(a), where the probe was able to follow the actual topographical surface of the patterns. Because the width of pattern was large enough for the probe to trace the bottom of a valley, it was observed that the depth of the mask pattern was about $100\ nm$ while that of a blue-ray disc was below 20nm as shown in Fig. 5. The optical image of the chromium pattern on a quartz glass plate was also obtained by the asymmetric response of a tuning fork as shown in Fig. 7(b) simultaneously. The scanning area was $5 \times 5\ \mu m^2$. The optical probe was able to emit a laser light of 650nm and diffracting lights from the mask sample was gathered by the objective lens. The optical signal consistent with the topogrpahic image was obtained using a photo-detector (see Fig. 1). Therefore, this method has the potential of sensing the density fluctuations of the samples with almost no height variations and obtaining an optical image through the opening aperture of the probe simultaneously.

#4890 - $15.00 US

Received 29 July 2004; revised 7 September 2004; accepted 9 September 2004

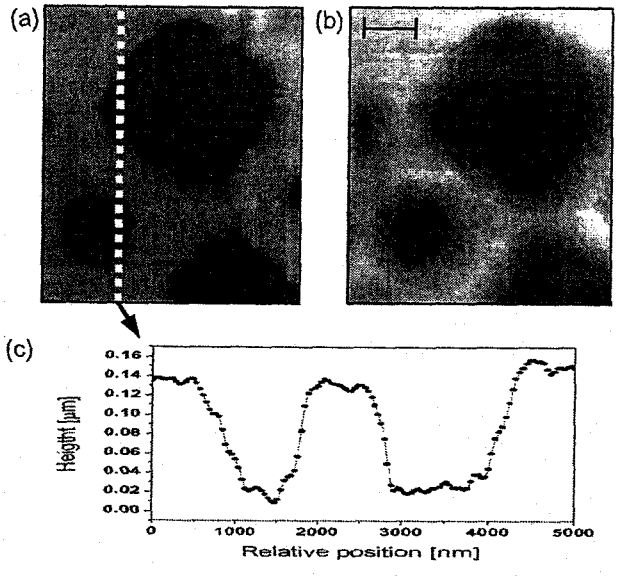

Fig. 7. Topographic image(a) and optical image(b) of chromium mask pattern respectively and the cross-section view(c) along white dotted line.

In conclusion, we have investigated symmetric and asymmetric responses of the tuning fork to enhance the shear-force detection sensitivity of the probe-sample distance-control for our NSOM system. Particularly, we have demonstrated that the asymmetric frequency response of $Q \geq 2500$, with the suppressed background feedback signal, can be reproduced by controlling the mounting conditions on an edge-clipped dithering PZT plate. The asymmetric system applied to the NSOM allows us to acquire nano-scale surface images with a shear-force vertical stability of less than 2nm which was enhanced 5 times as much as for the conventional case. A simplified model based on a coupled harmonic oscillator system is also presented to theoretically describe the asymmetric behavior of the tuning fork. We believe that it will be particularly useful in imaging biological samples having density fluctuations and/or refractive index variations of comparably high lateral and vertical resolution.

Acknowledgments

This research was supported by the Ministry of Science and Technology through the National Research Laboratory Program (Contact No. M1-0203-00-0082).

#4890 - $15.00 US

Received 29 July 2004; revised 7 September 2004; accepted 9 September 2004

Journal of the Korean Physical Society, Vol. 45, No. 4, October 2004, pp. 1060~1064

Fabrication of a Novel Nano-Probe Slide for Near-Field Optical Microscopy

Sang-Youp YIM, Eunhee JEANG, Jae-Hoon LEE and Seung-Han PARK*
National Research Laboratory of Nonlinear Optics, Yonsei University, Seoul 120-749

Kyuman CHO
Department of Physics, Sogang University, Seoul 121-741

(Received 26 April 2004)

A novel probe structure, which can act as a planar nano-*probe slide* for near-field microscopy, was proposed and fabricated. Sub-wavelength apertures on a Si substrate are successfully produced by means of standard photolithography techniques with properly selected masks. In particular, the anisotropic etching characteristics of Si substrate and the hardness of the Si_3N_4 film are utilized. Probe-to-probe scanning of the fabricated near-field nano-*probe slide* shows sub-wavelength confinement of light and comparable throughput to the conventional optical fiber probe. We also show that the nano-*probe slide* can serve as a supporting base and a sub-wavelength aperture to obtain the near-field photoluminescence spectra of a limited number of CdSe nanocrystals.

PACS numbers: 07.79.Fc, 78.67.Bf
Keywords: Nano-probe, Sub-wavelength aperture, Throughput, Near-field scanning optical microscopy

I. INTRODUCTION

The nano-optical probe is one of the key elements for constructing the near-field scanning optical microscope (NSOM). The most commonly used probe for NSOM imaging is a metal-coated tapered optical fiber tip, fabricated either by a pulling [1] or an etching process [2]. However, various types of probes, such as the micromachined cantilever type probe [3], the 'apertureless' metal probe [4], the solid immersion lens [5], the surface-plasmon-enhanced metal aperture [6], *etc.*, have also been developed and adopted. Each probe, including the tapered optical fiber tip, has unique advantages, which may enhance the capabilities of the NSOM.

In general, a complex distance regulating system [7, 8] in the NSOM makes most of the probes difficult to use for nanostructure investigations and device applications. For NSOM devices, in addition, batch production of the probe, as well as simple operation for near-field distance detection, are required. Recently, therefore, different approaches without using a distance regulating system have been reported in order to overcome the aforementioned difficulties, including apertures in metal films directly deposited on GaAs quantum dots (QD) [9], a stationary near-field nano-slit scanner with moving samples [10], and zero-mode waveguides [11]. E-beam lithography techniques with fine controllability were employed to fabricate such probes, resulting in the lack of direct application to industry.

In this paper, we propose a new type of near-field optical nano-probe integrated with a nano-slide, which can be produced by using a standard photolithographic technique. In contrast to previous works, our proposed probe has a few tens of nanometer thick silicon-nitride (Si_3N_4) film on a nano-aperture, which acts as a 'slide (glass)' for the samples, as shown in Fig. 1. Hereafter, we call this system a 'nano-*probe slide*'. As displayed in Fig. 1(a), a sample placed on the top of the nano-*probe slide* experiences near-fields because the distance between the aperture and the sample is determined by the sub-wavelength thickness of the Si_3N_4 film. If the sample is brought inside the nano-*probe slide*, as is depicted in Fig. 1(b), it will be immersed in a completely undiffracted near-field. Compared with the metal coated tapered optical fiber tip, our proposed nano-*probe slide* has superior properties, such as mechanical strength, high throughput, and batch production [12]. Moreover, easy access to both sides of the nano-*probe slide* opens new possibilities for

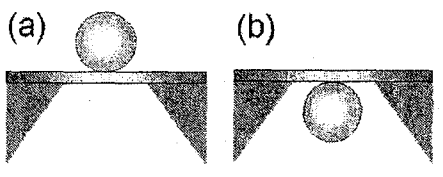

Fig. 1. Schematic diagram of the proposed nano-*probe slide*. Nano-materials can be located on top of the nano-probe, either (a) outside, or (b) inside.

*E-mail: shpark@phya.yonsei.ac.kr;
Tel: +82-2-2123-2617; Fax: +82-2-392-3374

the NSOM and for near-field optical-device applications.

II. FABRICATION OF A NANO-PROBE SLIDE

Figure 2 is a flow chart of the fabrication process for a nano-slide integrated with a nano-probe. The fabrication process is based on the anisotropic etching characteristics of Si substrates and the robustness of Si_3N_4 films. If a Si substrate is dipped into an anisotropic etchant, *e.g.*, a potassium hydroxide (KOH) aqueous solution, due to the different etch rates along the crystal directions, the {111} planes of the Si structure serve as etch stops, so the width of an etched {100} plane decreases along the depth, forming an inverted pyramid [13]. Therefore, sub-wavelength apertures can be produced routinely by means of standard photolithography techniques with properly selected masks [12].

We used a silicon-on-insulator (SOI) wafer, which consisted of a nominal 15-μm-thick (100)-direction Si top layer and a 1-μm-thick SiO_2 layer on a bulk 500-μm Si substrate (Fig. 2(a)), as the starting material. The bottom side of the bulk substrate was coated with a 1-μm oxide layer. The SOI wafer provided sufficient homogeneity of the Si layer and a high enough accuracy for the Si layer thickness. The measured thickness variation was within 500 nm over the entire 4-inch-diameter wafer. Note that such a small thickness variation cannot be obtained if the bulk Si wafer is employed. Therefore, the SOI wafer reduces unnecessary lithographic errors originating from variations in the Si layer thickness.

Before the sub-wavelength aperture was opened, a window region was fabricated by using photolithography with dry etching on the bottom side of the SOI wafer (Fig. 2(b), (c)). The buried oxide layer served as an etch stop. The prepared window was $\sim 0.6 \times 0.6$ mm^2. Subsequently, the oxide layers were removed by using buffered oxide etchant (BOE) because the oxide layers usually cause a strain that bulges out the silicon layer.

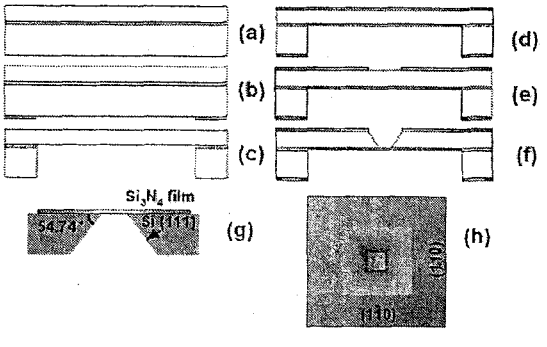

Fig. 2. (a) ~ (f) Fabrication procedure for the nano-*probe slide*. Details are in the text. (g) Side view, and (h) front view of the proposed nano-*probe slide*.

On both sides of the remaining Si layer, a robust Si_3N_4 film was grown by using a low pressure chemical vapor deposition (LPCVD) method. Silicon nitride was chosen because of its optical transparency up to the UV region and fairly strong hardness. Moreover, Si_3N_4 films can be deposited routinely during the Si fabrication process. The upper Si_3N_4 layer was used as a mask film (Fig. 2(d)), and the lower one, typically 30-nm-thick, was preserved to be the nano-*probe slide*.

On the Si_3N_4 mask film, an aperture pattern was formed by using photolithography with a reactive ion etching process, as in the window formation process (Fig. 2(e)). Finally, the Si layer was dipped into a KOH aqueous solution (10 weight percent, 65 °C), which is one of the most widely used anisotropic etchants of silicon (Fig. 2(f)). As mentioned above, the final aperture size was determined by the basal width, the etched silicon layer thickness, and the angle between the base and the side wall (54.75°). To reduce the etchant density gradient, we stirred the solution with a magnetic spin bar. The estimated etch rate, measured by using an α-step stylus, was about 40 μm/hour.

III. RESULTS AND DISCUSSION

Figure 3(a) and (b) show scanning electron micrograph (SEM) images of a 10 × 10 array of probes and one single probe, respectively. As Fig. 3(a) shows an array structure is well fabricated over the entire area. Moreover, most of apertures of the array exhibit nearly the same size for the same mask width, even though the size deviation is not perfectly controllable in this simple method. The aperture size is found to increase/decrease along one direction, suggesting a thickness variation in the Si substrate. The measured aperture size variation is within 100 nm.

A highly magnified SEM image (Fig. 3(b)) shows that an inverted pyramid is etched down to the bottom, successfully forming a sub-wavelength aperture. The dark center area of less than 130 × 170 nm is the exposed silicon nitride layer, *i.e.*, the nano-slide. The slightly elongated aspect ratio might be due to a thickness difference

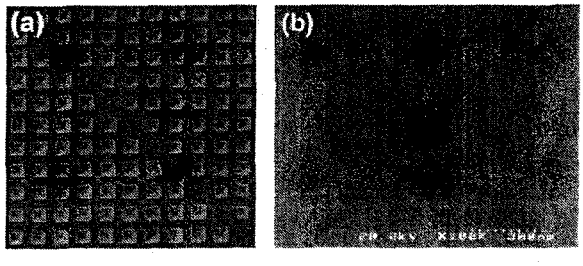

Fig. 3. SEM image of (a) an array of nano-*probe slides* (total area ~ 450 × 450 μm), and (b) a single nano-*probe slide*.

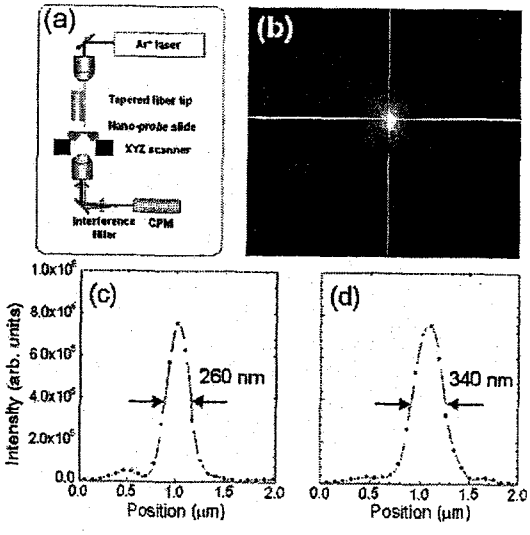

Fig. 4. (a) Near-field measurement setup and (b) spatial distribution of the near-field intensity of a nano-*probe slide*. The total scan area is 2 × 2 μm. The line profile of the near-field intensity along (c) the x & (d) the y directions.

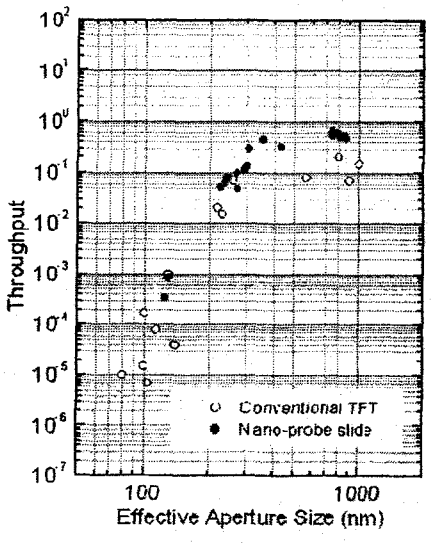

Fig. 5. Throughput as a function of the effective aperture size. The throughput data of a conventional tapered fiber tip is replotted from Ref. 17.

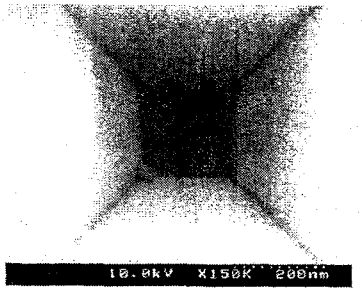

Fig. 6. CdSe nanocrystals located on a nano-*probe slide*.

in the Si layer. Unless particles exist on the nano-slide, all the apertures appear to be dark due to the relatively low brightness inside the inverted pyramid hole.

At the present state, metal is not coated on the sides of the inverted pyramid hole of our nano-probe. An uncoated probe usually exhibits a leaky aperture, which degrades the spatial resolution of the near-field image [14]. However, the huge absorption by silicon at UV-visible wavelengths can suppress the far-field components and reduce the effective aperture of the uncoated nano-*probe slide*. The absorption coefficient of Si is reported to be as high as $\sim 1.9 \times 10^4$ cm^{-1} at 2.54 eV (488 nm) and to increase to nearly 10^6 cm^{-1} at 3.81 eV (325 nm) [15]. Therefore, if a UV laser is used, the light confinement effect is expected to be the same order of magnitude as that for a metal-coated probe. In addition, the near-field interaction between a material and an aperture contributes strongly to the signal in NSOM spectroscopy [16].

To confirm the sub-wavelength confinement of light and to measure the throughput of the nano-*probe slide*, we measured the transmitted power through the nano-*probe slide* by using the probe-to-probe scanning method [17]. A metal-coated tapered optical fiber tip with a 100-nm aperture (Nanonics) was brought onto the nano-*probe slide* by using tuning-fork-based shear-force detection [18] and scanned over the aperture region in the constant gap mode (Fig. 4(a)). A 488-nm-wavelength Ar laser beam was coupled into the tapered fiber tip, and the light transmitted through the nano-*probe slide* was measured through a 488-nm interference filter by using a channeled photomultiplier tube (CPM).

The measured spatial distribution of the near-field intensity, as expected, shows a larger effective aperture size than the geometrical one. Note that the near-field intensity map was obtained from the aperture shown in Fig. 3(b). Interestingly, the near-field distribution along the x axis is slightly shorter ($\sim$ 80 nm) than that along the y axis, as shown in Figs. 4(c) and 4(d). In fact, as Fig. 3(b) shows, the aperture is elongated by $\sim$ 40 nm along the y axis. The full widths at half maximum (FWHM) of the line profile are estimated to be 260 nm ($\sim \lambda/1.9$) and 340 nm ($\sim \lambda/1.5$).

Figure 5 shows the throughput, defined by the ratio of the input power to the output power through the nano-*probe slide*, for various effective sizes. Because of the finite size of the tapered optical fiber tip (100 nm), a deconvolution technique was employed to estimate the effective size of the nano-*probe slide*. As can be seen in Fig. 5, the throughput of our nano-*probe slide* is quite comparable to that of a conventional probe [19]. As mentioned above, however, it should be emphasized that the probe presented here is purely dielectric and that the confinement of light originates only from band-to-band absorption and the waveguide geometry. In contrast to

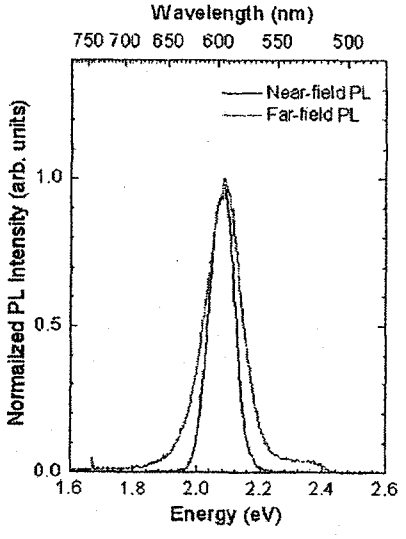

Fig. 7. Comparison of far-field PL and near-field PL from CdSe nanocrystals on a nano-*probe slide*. The linewidths of the far-field and the near-field PL are 140 meV and 92 meV, respectively.

the metal-coated fiber tip, therefore, our nano-*probe slide* has much more endurance for high input powers and much better mechanical durability.

Finally, as Fig. 6 shows, a 200-nm-wide nano-*probe slide* and CdSe nanocrystals placed on top of the nano-*probe slide* were imaged by using scanning electron microscopy (SEM). The CdSe nanocrystals were prepared, by using a chemical method, as a colloid in Hexane. A 10-μl drop was spin cast at 5000 rpm for 60 seconds. It is clearly shown that the nano-slide can serve as a supporting base for CdSe nanocrystals. Figure 7 shows the near-field photoluminescence (PL) spectra of CdSe nanocrystals on one of the nano-*probe slide* apertures, compar with the far-field PL spectrum. The linewidth of the PL spectrum, emitted from the CdSe nanocrystals narrows down to 65 % compared with the far-field PL at room temperature. This result confirms that the nano-*probe slide* can illuminate locally, only a limited number of nanocrystals is exposed to the excitation light, and a direct near-field characterization of nano-materials is possible without a complex sample-probe distance regulating system.

IV. CONCLUSIONS

In summary, a novel near-field planar nano-probe structure, accessible by standard photolithographic techniques, was proposed. The proposed nano-*probe slides* with various sizes were fabricated successfully by using a photolithography technique with properly selected masks, anisotropic etching characteristics of the Si substrate and the robustness of the Si_3N_4 film. The scanning electron micrograph (SEM) images clearly showed that a 10 × 10 array of probes and one single probe could be realized. In addition, with the help of the probe-to-probe scanning technique, a sub-wavelength confinement and a high throughput comparable to those of a conventional tapered optical fiber probe were confirmed. CdSe nanocrystals were successfully located on top of the nano-*probe slide* by using a spin coating method. The linewidth of the PL spectrum in the near-field region is narrower than that in the far-field region, indicating the possibility of direct near-field characterization of nano-materials without complex sample-probe distance regulating systems. We hope that our proposed nano-slide integrated with a nano-probe can be quite useful for investigating organic and inorganic samples which require the high input intensities.

ACKNOWLEDGMENTS

This research was supported by the Ministry of Science and Technology through the National Research Laboratory Program (Contact No. M1-0203-00-0082).

REFERENCES

[1] E. Betzig, J. K. Trautman, T. D. Harris, J. S. Weiner and R. L. Kostelak, Science **251**, 1468 (1991).
[2] T. Pangaribun, K. Yamada, S. Jiang, H. Ohsawa and M. Ohtsu, Jpn. J. Appl. Phys. **31**, L1302 (1992).
[3] N. F. van Hulst, M. H. P. Moers, O. F. J. Noordman, R. G. Tack, F. B. Segerink and B. Bölger, Appl. Phys. Lett. **62**, 461 (1993).
[4] F. Zenhausern, Y. Martin and H. K. Wickramasinghe, Science **269**, 1083 (1995).
[5] S. M. Mansfield and G. S. Kino, Appl. Phys. Lett. **57**, 2615 (1990).
[6] T. W. Ebbesen, H. J. Lezec, H. F. Ghaemi, T. Thio and P. A. Wolff, Nature **391**, 667 (1998).
[7] Jae-Hoon Lee, Jang-Hoon Too, Sang-Youp Yim and Seung-Han Park, J. Korean Phys. Soc **45**, 455 (2004).
[8] Jinan Xia, Beom Hoan O, Seung Gol Lee and El-Hang Lee, J. Korean Phys. Soc **42**, 226 (2003).
[9] N. H. Bonadeo, G. Chen, D. Gammon, D. S. Katzer, D. Park and D. G. Steel, Phys. Rev. Lett. **81**, 2759 (1998).
[10] J. O. Tegenfeldt, O. Bakajin, C.-F. Chou, S. S. Chan, R. Austin, W. Fann, L. Liou, E. Chan, T. Duke and E. C. Cox, Phys. Rev. Lett. **86**, 1378 (2001).
[11] M. J. Levene, J. Korlach, S. W. Turner, M. Foquet, H. G. Craighead and W. W. Webb, Science **299**, 682 (2003).
[12] M. B. Lee, M. Kourogi, T. Yatsui, K. Tsutsui, N. Atoda and M. Ohtsu, Appl. Opt. **38**, 3566 (1999).
[13] M. Elwenspoek and H. V. Jansen, *Silicon Micromachining* (Cambridge University Press, New York, 1998).
[14] V. Sandoghdar, S. Wegscheider, G. Krausch and J. Mlynek, J. Appl. Phys. **81**, 2499 (1997).

[15] S. M. Sze, *Physics of Semiconductor Devices* (Wiley, New York, 1981).
[16] K. B. Song, J. E. Bae, K. Cho, S. Y. Yim and S. H. Park, Appl. Phys. Lett. **73**, 2260 (1998).
[17] T. Yatsui, M. Kourogi and M. Ohtsu, Appl. Phys. Lett. **71**, 1756 (1997).
[18] K. Karrai and R. D. Grober, Appl. Phys. Lett. **66**, 1842 (1995).
[19] T. Yatsui, M. Kourogi and M. Ohtsu, Appl. Phys. Lett. **73**, 2090 (1998).